# Strong Dipolar Effects in a Chromium Bose-Einstein Condensate

Diplomarbeit
vorgelegt von
**Bernd Fröhlich**

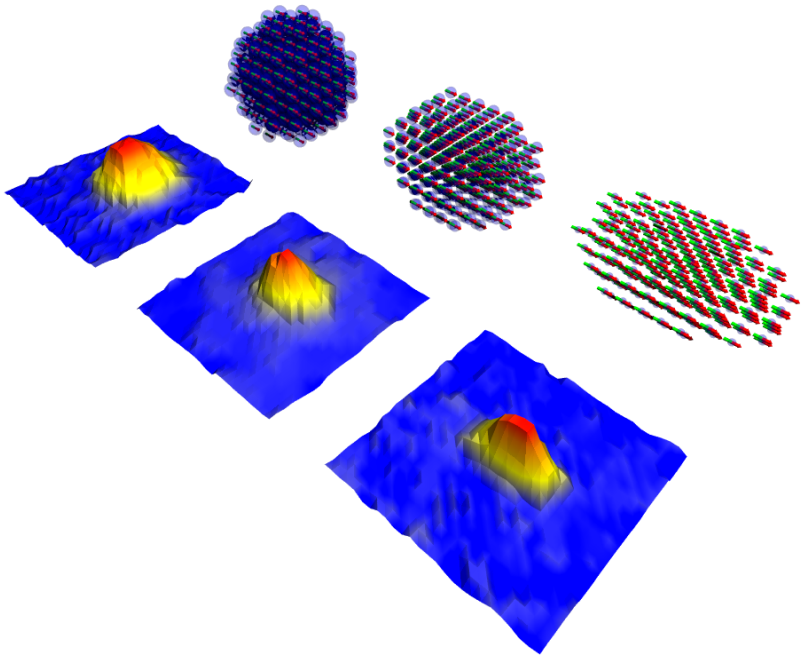

Hauptberichter: Prof. Dr. Tilman Pfau
Mitberichter: Prof. Dr. J. Wrachtrup

5. Physikalisches Institut
Universität Stuttgart

13. Juli 2007

# Contents

# Zusammenfassung

Im Rahmen dieser Arbeit wurde erstmals eine Supraflüssigkeit realisiert, die eine starke Dipol-Dipol-Wechselwirkung zwischen ihren mikroskopischen Bestandteilen aufweist [1]. Diese Supraflüssigkeit kann in Analogie zu klassischen Ferroflüssigkeiten eine Quanten-Ferroflüssigkeit genannt werden. Die Dipol-Dipol-Wechselwirkung unterscheidet sich durch ihren anisotropen — also symmetriebrechenden — und langreichweitigen Charakter fundamental von der Kontakt-Wechselwirkung, welche bisher in allen Experimenten mit ultra-kalten atomaren Gasen dominierend war. Die Realisierung einer Quanten-Ferroflüssigkeit ist daher der erste Schritt zur Untersuchung einer Fülle neuer physikalischer Phänomene in ultra-kalten Gasen [2].

Eine Supraflüssigkeit weist einige außerordentliche Eigenschaften auf, z.B. fliesst sie ohne Reibung und hat eine unendliche thermische Leitfähigkeit. Diese Eigenschaften sind eine direkte Folge der bosonischen Natur ihrer Bestandteile. Das erste System in dem suprafluide Eigenschaften beobachtet wurden war flüssiges Helium 1937 [3, 4]. Hierbei wurde das bosonische Isotop $^4$He verwendet. Aber auch in flüssigem Helium bestehend aus dem fermionischen Isotop $^3$He wurde 35 Jahre später Suprafluidität nachgewiesen [5]. Dies ist durch eine Paarbildung der $^3$He Atomen zu Bosonen möglich. Ein weiterer Meilenstein in der Untersuchung von Supraflüssigkeiten war die Realisierung eines Bose-Einstein Kondensats in verdünnten atomaren Gasen 1995 [6, 7]. Diese Systeme erlauben einer hervorragende Kontrolle der experimentellen Parameter und haben eine Vielzahl grundlegender Untersuchungen suprafluider Phänomene erlaubt. Aber auch in fermionischen atomaren Gasen wurde zehn Jahre später Suprafluidität nachgewiesen [8], die wiederum nur durch eine Paarbildung der Atome möglich ist. In diesen Experimenten mit ultra-kalten bosonischen oder fermionische Gasen war bisher die Kontakt-Wechselwirkung dominierend, deren Stärke durch einen einzigen Parameter, die Streulänge $a$, beschrieben werden kann.

Trotz des vergleichsweise großen Dipolmoments von 6 $\mu_{\mathrm{B}}$ von $^{52}$Cr Atomen ist die Kontakt-Wechselwirkung auch in einem Chrom Bose-Einstein Kondensat dominierend. Die Dipol-Dipol-Wechselwirkung kann als Störung in der Beschreibung des Kondensats berücksichtigt werden. Das erste Chrom Bose-Einstein Kondensat wurde 2004 von Griesmaier und Mitarbeitern realisiert [9]. Ein Jahr später konnte der Effekt der Dipol-Dipol-Wechselwirkung erstmalig anhand einer Modifizierung der Form des Kondensates nachgewiesen werden [10].

Eine Methode, die die Stärke der Dipol-Dipol-Wechselwirkung relativ zur Kontakt-Wechselwirkung erhöht, ist die Verwendung einer Feshbach Resonanz um die Streulänge und somit die Stärke der Kontakt-Wechselwirkung zu verringern. Feshbach Resonanzen wurden 1998 erstmals in einem ultra-kalten atomaren Gas nachgewiesen [11]. Sie erlauben es durch Anlegen eines Magnetfelds die Streulänge über einen weiten Bereich von positiven bis hin zu negativen Werten zu varriieren. Auch in einem ultra-kalten Gas aus $^{52}$Cr Atomen wurden im Jahr 2004 Feshbach Resonanzen nachgewiesen [12].

Im Rahmen dieser Arbeit wird die breiteste dieser Resonanzen verwendet, um die Streulänge von Chrom auf ein Fünftel des ursprünglichen Wertes zu verringern. Diese Verringerung

führt gleichzeitig zu einer Erhöhung der relativen Stärke der Dipol-Dipol-Wechselwirkung um einen Faktor fünf. Somit wird erstmals eine Supraflüssigkeit erzeugt, die stark durch den dipolaren Charakter ihrer Bestandteile beeinflusst ist. In einer Serie von Experimenten wird die Anwendbarkeit der Methode demonstriert, um diese Quanten-Ferroflüssigkeit zu untersuchen. Diese Arbeit enthält neben einer ausführlichen Beschreibung der durchgeführten Experimente eine Einführung in die theoretische Beschreibung von Feshbach Resonanzen und dipolaren Kondensaten, sowie eine Beschreibung der Modifikationen des Experiments, die nötig waren, um die Ergebnisse zu ermöglichen. Ein ausführlicher Anhang berichtet über den ebenfalls im Rahmen dieser Arbeit realisierten akusto-optischen Modulator (AOM) Treiber, welcher durch Verwenden von zwei verschiedenen Radiofrequenzsignalen die Stabilität der Dipolfallen-Laserstrahlen signifikant erhöht [13].

# 1. Introduction

A superfluid is a *quantum fluid*. The quantum character of any microscopic particle, which is usually not visible in macroscopic bodies, gives rise to their exceptional properties, like zero viscosity or infinite thermal conductivity. The quantum character is visible, because the phase relation between the quantum particles of which it is composed of is fixed, whereas it is random in classical bodies, leading on average to the classical properties. The collective behaviour of the quantum particles arises from the Bose statistics describing their many-body state [14]. The first system to show superfluid character was liquid helium in 1937 [3, 4]. Not only the bosonic $^4$He undergoes the phase transition to a superfluid, also $^3$He condenses to a superfluid via a pairing mechanism of the fermionic atoms [5], analogous to the *Cooper pairing* responsible for superconductivity. The symmetry-breaking interaction in $^3$He, caused by the p-wave pairing, substantially enriches the physical properties of the $^3$He superfluid compared to the $^4$He system [15].

A new system that allows to study superfluidity are quantum-degenerate bosonic or fermionic gases. The narrow path to cool down an atomic sample to a state which reveals the quantum nature — without solidifying the sample — has prevented the realization of such systems until 1995. First the group of Wieman and Cornell [6] and shortly afterwards the group of Ketterle [7] produced quantum-degenerate bosonic gases of $^{87}$Rb and $^{23}$Na atoms. These *Bose-Einstein condensates* (BECs) of dilute gases, later also realized with $^7$Li [16], spin-polarized hydrogen [17], $^{85}$Rb [18], metastable Helium [19], $^{41}$K [20], $^{133}$Cs [21], $^{174}$Yb [22], $^{52}$Cr [9] and recently with $^{39}$K [23], led to many experiments on superfluid properties, for example on collective oscillations [24] or vortices [25]. The dominant interaction underlying these experiments is the isotropic and short-range *contact interaction*, which for ultra-cold atoms is described by a single parameter, the scattering length $a$ [26]. The tunability of this parameter via *Feshbach resonances* [11] is an important tool to study a wide range of physical regimes.

A quantum-degenerate gas of fermions, first realized in 1999 with potassium atoms [27], shows superfluidity via a pairing of the atoms like in $^3$He [8]. Two atoms in different spin states form a weakly bound Cooper pair, which is a boson and can undergo condensation. The theory describing the paring was developed in 1957 mainly by Bardeen, Cooper and Schrieffer [28]. The condensed state of Cooper pairs is therefore called *BCS state*. The pairing mechanism depends strongly on the interaction between the atoms. Like for bosons the dominant interaction is the contact interaction. Hence, it is tunable via Feshbach resonances [29, 30, 31], which allowed to study the crossover of the BCS state to a condensate of diatomic molecules [32, 33, 34]. A quantum gas of fermions is an ideal model system to explore the formation of a superfluid made of paired fermions. Besides the interaction strength, also the ratio of the atoms in different spin states can be controlled precisely. Thus, the formation is studied over a wide parameter range (see for example [35]).

Another interaction, which promises the realization of a new type of superfluid, is the *dipole-dipole interaction*. It attracts a large attention of theoreticians currently, apparent

through about 60 publications on this topic over the last 5 years. Dipole-dipole interaction has long-range character and is anisotropic. This distinguishes it significantly from contact interaction. The symmetry-break corresponding to the anisotropy is predicted to give rise to a variety of new physical phenomena [2], similar to the enrichment of the physical properties of $^3$He compared to $^4$He. Among these new phenomena are e.g. novel quantum phases in optical lattices, such as checkerboard or supersolid phases [36], or structured density profiles [37], including biconcave density distributions in pancake-shaped traps [38]. Dipolar effects should also enrich the field of spinor physics [39, 40, 41]. Another interesting prediction for these systems is a roton-like excitation spectrum [42].

A superfluid with strong dipolar interaction can be called a *quantum ferrofluid*, in analogy to classical ferrofluids. Polar molecules in their vibrational ground state are a possibility to realize them with *electric* dipoles. Although progress has been made recently in slowing and trapping of polar molecules (see for example [43]), the densities and temperatures reached are still far from quantum-degeneracy. Polar molecules created from two ultra-cold atomic species via Feshbach resonances [44] are an actively explored alternative [45]. However, until now it is not possible to bring these molecules to their vibrational ground state [46]. Electric dipoles induced by dc electric fields [47] or by light [48] might be an alternative.

The first quantum ferrofluid was realized with *magnetic* dipoles [1] and is presented in this thesis. Our experimental approach makes use of the large magnetic dipole moment of $6\mu_\mathrm{B}$ of Chromium atoms to realize such a quantum system. Important steps that paved the way towards this development were the observation of Feshbach resonances in 2004 [12] and the condensation of Chromium in 2004 [9]. Besides, experiments on the expansion dynamics of Chromium showed in 2005 [10] for the first time dipolar effects in a BEC. However, the relative strength of the dipole-dipole interaction to the contact interaction in these measurements corresponded only to a small perturbation, although the dipole-dipole interaction is 36 times larger than in standard alkali quantum gases. This is changed with the experiments that are a part of this thesis. By using a Feshbach resonance to tune the scattering length $a$, the relative strength of the dipole-dipole interaction is increased by a factor of 5. This modifies the condensate properties way beyond the perturbative regime and constitutes the first realization of a quantum ferrofluid.

**This thesis is organized as follows:**
In chapter 2 the theory of Feshbach resonances is introduced. To provide a theoretical basis to understand the physics of Feshbach resonances, the first section reports on scattering theory with a focus on the scattering properties of ultra-cold atomic gases. The second section discusses the phenomenological properties of Feshbach resonances, which supports the theoretical description in section 3. The theoretical approach presented follows closely [44] and [49]. The last section describes the Feshbach resonances of Chromium, which have been observed in a series of measurements in 2004 [12].

Chapter 3 gives an introduction to the theoretical description of Bose-Einstein condensates with dipole-dipole interaction. To introduce the theoretical methods used to describe BECs, and to allow a comparison of condensates with and without dipole-dipole interaction, the first two sections take only contact interaction into account. The first section discusses important properties of the steady-state of BECs. The mean-field description with a macroscopic wave function and the Thomas-Fermi approximation are introduced. The second section reports

on the hydrodynamic description of the condensate dynamics. In the third section this hydrodynamic theory is expanded to include dipole-dipole interaction. The main results of this theory, which are used in the data analysis of the experiments on strong dipolar effects, are presented.

The apparatus that is used for the experiments is described in chapter 4. The first section gives a coarse overview of the experiment, more details can be found for example in [50]. The important steps to produce a quantum-degenerate gas of Chromium atoms are described. The second section reports on the measurements of the trapping frequencies of the optical dipole trap, which are performed with a new method, that has not been used in our setup before. Next, I discuss modifications of the apparatus, which are done to perform the experiments presented in this thesis. The third section reports on the production of a stable, homogenous magnetic field at $\sim 600$ G, which is needed to tune the scattering length $a$ via a Feshbach resonance. Also described is the calibration of the curvature compensation, which allows us to produce BECs at these high magnetic fields. The last section discusses the high-field imaging system, which is used to image the atoms at the high magnetic fields.

Finally, in chapter 5 the experimental results on strong dipolar effects in a quantum gas are presented. In the first section the broadest Feshbach resonance at 589.1 G is characterized. This resonance is used to tune the scattering length $a$. Both measurements on the lifetime and the variation of $a$ in the vicinity of the resonance are described. In the second section the observation of strong dipolar effects is discussed, which are apparent through a change of the condensate shape. In a time-of-flight series our control on the system is demonstrated.

An appendix provides additional information. In particular it reports on a two-frequency acousto-optic modulator driver realized as a part of this thesis [13], which is included in the setup to improve the stability of the optical dipole trap.

# 2. Scattering Theory and Feshbach Resonances

*In the experiments presented in this thesis a Feshbach resonance is used to tune the contact interaction strength. The theoretical description of Feshbach resonances is introduced in this chapter. For a basic understanding of these resonances, scattering theory is required. Hence, section 2.1 gives an overview on scattering theory, focusing on the collision dynamics of ultra-cold atoms. The presentation follows closely [26] and chapter 8 in [51]. The partial wave decomposition for spherically symmetric potentials is not discussed. I chose a more general approach to prepare the theoretical description of Feshbach resonances and for brevity. For information on the partial wave decomposition the reader is referred to the standard literature on scattering theory [51, 52, 53]. In section 2.2 the physical process underlying a Feshbach resonance is discussed and their properties are described phenomenologically. With this background, in section 2.3 the theory of Feshbach resonances is introduced. The main steps to obtain an expression for the scattering length as a function of the magnetic field $B$ are presented. The last section 2.4 reports on the Feshbach properties of $^{52}Cr$.*

## 2.1. Collisional Dynamics of Ultra-Cold Atomic Gases

A basic knowledge of collision physics is important to understand the properties of ultra-cold atomic gases. Elastic collisions for example ensure the thermalization of a gas, which is crucial for evaporative cooling. A second example is the expansion of a BEC which is governed by the mean-field interaction. For a dilute gas the interaction range $r_0$ between two atoms (typically on the order of a few nm) is much smaller than the mean distance between them (typically a few 100 nm). This allows to reduce the theoretical description of the collisions to the scattering problem of only two atoms [26]. They interact via their molecular potential, which consists of several contributions like the exchange interaction or the van der Waals interaction. For ultra-cold atomic samples a detailed knowledge of the molecular potential is not needed to describe the collision process: The thermal de Broglie wavelength

$$\lambda_{\mathrm{th}} = \sqrt{\frac{2\pi\hbar^2}{mk_{\mathrm{B}}T}}\,, \tag{2.1}$$

where $m$ is the atomic mass and $T$ is the temperature of the gas, is larger than $r_0$ and the details of the potential are not resolved. As we shall see, the scattering process is then isotropic and is described by a single parameter, the *scattering length* $a$. The complicated molecular potential is replaced by a simple contact interaction potential.

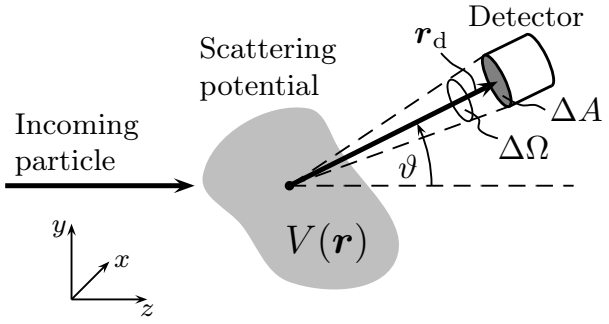


**Figure 2.1.:** *Sketch of a scattering process in the center-of-mass system. The incoming relative particle is scattered by the fixed potential $V(\boldsymbol{r})$ into the solid angle $\Delta\Omega(\vartheta, \varphi)$. The detector with the detecting area $\Delta A$ is placed at a distance $r_\mathrm{d}$ and thus $\Delta\Omega = \Delta A / r_\mathrm{d}^2$.*

### 2.1.1. Scattering Theory

The scattering problem of two distinguishable particles 1 and 2 with equal mass $m$ interacting via the potential $V(\boldsymbol{r}_1 - \boldsymbol{r}_2)$ is reduced to the scattering of one *relative particle* with the reduced mass $m_\mathrm{r} = m/2$ on a fixed target potential $V(\boldsymbol{r})$ by separating the center-of-mass motion and using relative coordinates

$$\boldsymbol{r} = \boldsymbol{r_1} - \boldsymbol{r_2}\,, \tag{2.2}$$

$$\boldsymbol{p} = (\boldsymbol{p_1} - \boldsymbol{p_2})/2\,. \tag{2.3}$$

Here $\boldsymbol{r}_1$ and $\boldsymbol{r}_2$ are the positions and $\boldsymbol{p}_1$ and $\boldsymbol{p}_2$ are the momenta of the particles. Figure 2.1 shows a sketch of a collision process. The incoming relative particle is scattered to an angle ($\vartheta$, $\varphi$) and detected with a detector that covers a solid angle $\Delta\Omega$. Let us now assume that we have an incoming flux of particles $j_0$, i.e. a certain amount of particles per time interval and unit area, interacting with $V(\boldsymbol{r})$. The probability that a particle is scattered into the direction of the detector is related to the differential cross section $\mathrm{d}\sigma(\vartheta, \varphi)$, which is defined as the number of scattered particles going through the area $\Delta A = r_\mathrm{d}^2 \Delta\Omega$ divided by the incoming flux $j_0$. With the scattered flux $j_\mathrm{s}(r, \vartheta, \varphi)$ this becomes

$$\mathrm{d}\sigma(\vartheta, \varphi) = \frac{j_\mathrm{s}(r, \vartheta, \varphi) r_\mathrm{d}^2 d\Omega}{j_0}\,, \tag{2.4}$$

if we make $\Delta\Omega$ infinitesimally small[1]. $\mathrm{d}\sigma$ has the dimension of an area, i.e. it corresponds to a surface that scatters particles into the direction ($\vartheta$, $\varphi$).

A quantum-mechanical description of the scattering problem starts from the hamiltonian $H$, which is given by the sum of kinetic and potential energy

$$H = \frac{p^2}{2m_\mathrm{r}} + V(\boldsymbol{r}) \tag{2.5}$$

[1]Later in this section it is shown that the radial dependence cancels out in Eq. (2.4). Hence, $\mathrm{d}\sigma(\vartheta, \varphi)$ does not depend on $r$.

of the relative particle. With the time-independent Schrödinger equation

$$H\psi_{\boldsymbol{k}}(\boldsymbol{r}) = E_k\psi_{\boldsymbol{k}}(\boldsymbol{r}) \tag{2.6}$$

we can calculate the stationary scattering eigenstates of $H$. We are interested only in the asymptotic behavior of these states as the mean distance between the atoms is much larger than the interaction range $r_0$. To calculate the asymptotic behavior, Eq. (2.6) is written in the form

$$(\Delta + k^2)\psi_{\boldsymbol{k}}(\boldsymbol{r}) = U(\boldsymbol{r})\psi_{\boldsymbol{k}}(\boldsymbol{r})\,, \tag{2.7}$$

with the notations

$$k^2 = \frac{2m_{\mathrm{r}}E_k}{\hbar^2}\,, \quad U(\boldsymbol{r}) = \frac{2m_r}{\hbar^2}V(\boldsymbol{r})\,. \tag{2.8}$$

The concept of *Green's functions*, known e.g. from the theory of electrodynamics, is a powerful tool to tackle a differential equation of the form of Eq. (2.7). With the Green's function $G_{\boldsymbol{k}}(\boldsymbol{r})$, which is defined through the following equation

$$(\Delta + k^2)G_{\boldsymbol{k}}(\boldsymbol{r}) = \delta(\boldsymbol{r})\,, \tag{2.9}$$

where $\delta(\boldsymbol{r})$ is the Dirac delta function, a formal solution of Eq. (2.7) is

$$\psi_{\boldsymbol{k}}(\boldsymbol{r}) = \psi_0(\boldsymbol{r}) + \int \mathrm{d}^3r' G_{\boldsymbol{k}}(\boldsymbol{r}-\boldsymbol{r}')U(\boldsymbol{r}')\psi_{\boldsymbol{k}}(\boldsymbol{r}')\,. \tag{2.10}$$

The first term $\psi_0(\boldsymbol{r})$ on the right hand side is the solution of the homogeneous differential equation

$$(\Delta + k^2)\psi_0(\boldsymbol{r}) = 0\,. \tag{2.11}$$

It describes the incoming particle in the asymptotic limit. We choose the easiest non-trivial solution of Eq. (2.11), a plane wave traveling in $z$ direction $\psi_0(\boldsymbol{r}) = e^{ikz}$, not taking into account the normalization problem.

It can be shown (see for example [53]), that the Green's functions has two linear independent solutions

$$G^{\pm}_{\boldsymbol{k}}(\boldsymbol{r}) = -\frac{1}{4\pi}\frac{e^{\pm ikr}}{r} \tag{2.12}$$

corresponding to an outgoing, respectively incoming, spherical wave. Only the outgoing spherical wave $G^{+}_{\boldsymbol{k}}$ is a physically sensible solution, because the scattered wave cannot exist before the particle is interacting with the potential. Let us now evaluate the asymptotic form of Eq. (2.10). If we look at a spot $S$ far from the interaction range of $V(\boldsymbol{r})$ (see Fig. 2.2), the argument $|\boldsymbol{r}-\boldsymbol{r}'|$ of $G_{\boldsymbol{k}}$ in Eq. (2.10) is approximately given by

$$|\boldsymbol{r}-\boldsymbol{r}'| \approx r - \hat{\boldsymbol{r}}\cdot\boldsymbol{r}' \tag{2.13}$$

with $\hat{\boldsymbol{r}} = \boldsymbol{r}/r$. Hence it follows for large $r$

$$G^{+}_{\boldsymbol{k}}(\boldsymbol{r}-\boldsymbol{r}') = -\frac{1}{4\pi}\frac{e^{ik|\boldsymbol{r}-\boldsymbol{r}'|}}{|\boldsymbol{r}-\boldsymbol{r}'|} \approx -\frac{1}{4\pi}\frac{e^{ikr}}{r}e^{-ik\hat{\boldsymbol{r}}\cdot\boldsymbol{r}'}\,. \tag{2.14}$$

If we insert this result into Eq. (2.10) together with the homogeneous solution $\psi_0(\boldsymbol{r})$, we end

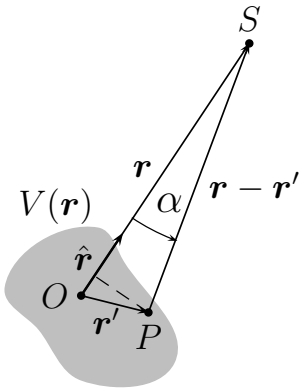


**Figure 2.2.:** *Illustration of the approximation* $|\boldsymbol{r}-\boldsymbol{r}'| \approx r - \hat{\boldsymbol{r}}\cdot\boldsymbol{r}'$. *If* $S$ *is far from the interaction region, the angle* $\alpha$ *between* $SO$ *and* $SP$ *is small, which means that the distance* $SP$ *is approximately equal to the projection of* $SP$ *on* $SO$.

up with

$$\psi_{\boldsymbol{k}}(\boldsymbol{r}) \overset{r\to\infty}{\sim} e^{ikz} - \frac{1}{4\pi}\frac{e^{ikr}}{r}\int \mathrm{d}^3r' e^{-ik\hat{\boldsymbol{r}}\cdot\boldsymbol{r}'}U(\boldsymbol{r}')\psi_{\boldsymbol{k}}(\boldsymbol{r}')\,. \tag{2.15}$$

The interpretation of expression (2.15) is more evident, if we write it in the following form

$$\psi_{\boldsymbol{k}}(\boldsymbol{r}) \overset{r\to\infty}{\sim} e^{ikz} + f_k(\vartheta,\varphi)\frac{e^{ikr}}{r}\,, \tag{2.16}$$

with the *scattering amplitude*

$$f_k(\vartheta,\varphi) = -\frac{m_\mathrm{r}}{2\pi\hbar^2}\int \mathrm{d}^3r' e^{-ik\hat{\boldsymbol{r}}\cdot\boldsymbol{r}'}V(\boldsymbol{r}')\psi_{\boldsymbol{k}}(\boldsymbol{r}')\,. \tag{2.17}$$

The asymptotic scattering state consists of the superposition of an incoming plane wave and an outgoing spherical wave with an angle-dependent pre-factor $f_k(\vartheta,\varphi)$. To connect the scattering amplitude with the differential cross section, the flux of the incoming plane wave and the scattered wave has to be calculated (see Eq. (2.4)). The stationary flux of a wave function is defined by [51]

$$\boldsymbol{j}(\boldsymbol{r}) := \frac{1}{m}\mathrm{Re}\left[\psi^*(\boldsymbol{r})\frac{\hbar}{\mathrm{i}}\boldsymbol{\nabla}\psi(\boldsymbol{r})\right]\,. \tag{2.18}$$

Hence, the incoming flux is

$$j_0 = \frac{\hbar k}{m_\mathrm{r}}\,. \tag{2.19}$$

The scattered flux is easiest calculated in spherical coordinates. At a distance $r$ large compared to the interaction region the flux in $\vartheta$ and $\varphi$ direction, $j_\vartheta$ and $j_\varphi$, are negligible compared to the radial component $j_r$, which is calculated to be [51]

$$j_r(r,\vartheta,\varphi) = \frac{\hbar k}{m_\mathrm{r}}\frac{1}{r^2}|f_k(\vartheta,\varphi)|^2\,. \tag{2.20}$$

Inserting $j_0$ and $j_s(r,\vartheta,\varphi) \approx j_r(r,\vartheta,\varphi)$ into Eq. (2.4) results in a simple relation between the differential cross section and the scattering amplitude

$$\frac{\mathrm{d}\sigma}{\mathrm{d}\Omega}(\vartheta,\varphi) = |f_k(\vartheta,\varphi)|^2 \,. \tag{2.21}$$

The scattering amplitude is thus directly connected to the experiment.

### 2.1.2. Low-Energy Limit

Let us now discuss the low-energy limit and show that the scattering is isotropic in this regime. In the low-energy limit the thermal de Broglie wavelength is large compared to the interaction range ($\lambda_{\mathrm{th}} \gg r_0$). In terms of the $k$-vector this is equivalent to $k \ll 1/r_0$. The main contributions to the integral of Eq. (2.17) are given for $|\boldsymbol{r}'| \lesssim r_0$, where the potential $V(\boldsymbol{r})$ has significant values. The factor $e^{-ik\hat{\boldsymbol{r}}\cdot\boldsymbol{r}'}$ in Eq. (2.17) is therefore approximately 1 as $k\hat{\boldsymbol{r}}\cdot\boldsymbol{r}' \lesssim kr_0 \ll 1$ and hence

$$f_k \approx -\frac{m_{\mathrm{r}}}{2\pi\hbar^2}\int \mathrm{d}^3r' V(\boldsymbol{r}')\psi_{\boldsymbol{k}}(\boldsymbol{r}') \,. \tag{2.22}$$

Consequently the interaction is isotropic, because the amplitude is independent of $\vartheta$ and $\varphi$. The integral equation (2.22) for $f_k$ is implicit, i.e. $f_k$ appears on both sides of Eq. (2.22)[2].

The scattering length[3] $a$ is defined as

$$a := -\lim_{k\to 0} f_k \,. \tag{2.23}$$

It can be shown that $a$ depends strongly on the details of $V(\boldsymbol{r})$ and that a small variation in $V(\boldsymbol{r})$ can lead to a divergence of $a$. This is the case e.g. for Feshbach resonances (see section 2.2 and 2.3). For potentials with a finite $a$, the total cross section $\sigma$, given by the integral of $\mathrm{d}\sigma/\mathrm{d}\Omega$ over the full $4\pi$ solid angle, is $4\pi a^2$. $\sigma$ is thus equal to the scattering area of a classical hard sphere with a radius given by twice the scattering length. This analogy helps to get a descriptive understanding of $a$. However, it is only valid if $a$ is positive, which is not necessarily the case.

The total cross section changes, if the colliding particles are indistinguishable. In this case it cannot be distinguished which particle is going in which direction after the collision (see Fig. 2.3). Therefore the wave function $\psi_{\boldsymbol{k}}(\boldsymbol{r})$ has to be symmetrized (anti-symmetrized) for bosons (fermions) against particle exchange. For the scattering amplitude the particle exchange is equivalent to a substitution of $(\vartheta,\varphi)$ by $(\pi-\vartheta,\varphi+\pi)$ [26]. Hence the differential cross section is

$$\frac{\mathrm{d}\sigma}{\mathrm{d}\Omega}(\vartheta,\varphi) = |f_k(\vartheta,\varphi) + \epsilon f_k(\pi-\vartheta,\varphi+\pi)|^2 \,, \tag{2.24}$$

with $\epsilon = +1$ for bosons and $\epsilon = -1$ for fermions. Consequently, at low energies collisions are strongly suppressed for fermions in the same quantum state and enhanced by a factor of 2

[2] This is changed with the Born approximation, where the scattered wave function $\psi_{\boldsymbol{k}}(\boldsymbol{r}')$ is replaced by the incoming plane wave $e^{ikz}$ (see for example [51] or [53]). The Born approximation is valid for weak interacting particles. It cannot be applied in case of contact interaction, but is used to describe dipole-dipole interaction (see section 3.3).

[3] Equal to the s-wave scattering length in the description by partial waves if only $l = 0$ contributes.

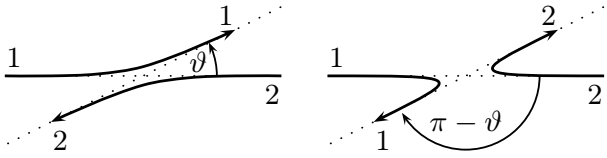


**Figure 2.3.:** *Scattering of identical particles. For identical particles the two processes shown in the figure are indistinguishable. The scattering amplitude $f_k(\vartheta, \varphi)$ describing the left process is equal to $f_k(\pi - \vartheta, \varphi + \pi)$, which describes the right process.*

for bosons, leading to a total cross section[4] of $8\pi a^2$ instead of $4\pi a^2$.

To obtain the macroscopic properties of an atomic gas from the microscopic theory of binary collisions, a mean field description is used. The mean field description makes use of a pseudo-potential, which replaces the complicated molecular potential between two atoms. This pseudo-potential must have the same scattering length $a$. A natural choice is a contact interaction potential [26]

$$V_{\text{contact}}(r) = g\delta(r)\,. \tag{2.25}$$

This potential has the same scattering length $a$ for[5]

$$g = \frac{2\pi\hbar^2 a}{m_{\text{r}}} = \frac{4\pi\hbar^2 a}{m}\,. \tag{2.26}$$

The form of the potential indicates the physical meaning of the sign of $a$, it determines whether the contact interaction is attractive ($a < 0$) or repulsive ($a > 0$).

## 2.2. Tuning the Scattering Length via Feshbach Resonances

The previous section has shown that the collisional properties in the low-energy limit are completely determined by a single parameter, the scattering length $a$. It has also been stated that a small variation of the scattering potential can have a strong effect on $a$. This is the case for Feshbach resonances, which allow to tune $a$ with a magnetic field $B$ over a wide range. To understand this phenomena, one needs to take a closer look at the atom-atom interaction. The molecular potential between two atoms depends on the internal atomic quantum states. For example, for two atoms with spin 1/2 the total spin can be either 0 or 1, leading to a singlet and a triplet potential with different strengths. To describe the physics behind a Feshbach resonance it is not enough to take into account only a single molecular potential between the atoms, Feshbach resonances occur due to a *coupling* between different potentials.

This is illustrated in Fig. 2.4. Two molecular potentials are indicated in the figure. The

[4] As the state specified by $(\vartheta, \varphi)$ is identical to $(\pi - \vartheta, \varphi + \pi)$, Eq. (2.24) has to be integrated only over half of the $4\pi$ solid angle to avoid double counting. Therefore the total cross section is enhanced only by a factor of 2 [54].

[5] To be more precise, the form (2.25) is applicable only for regular wave functions which do not have a $1/r$ divergence. For none-regular functions a regularizing operator has to be included (see for example [26] for details).

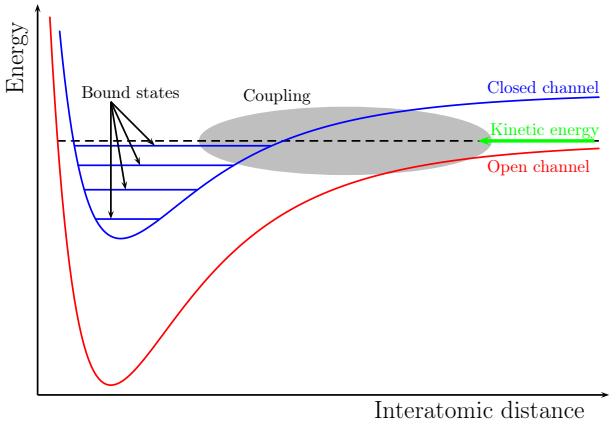


**Figure 2.4.:** *Coupling between molecular potentials that leads to a Feshbach resonance. The asymptotic value $E_\infty$ of the higher lying (blue) potential exceeds $E_{\mathrm{kin}}$ and can thus usually be neglected in the description of a scattering process. If a bound state of this potential comes close to $E_{\mathrm{kin}}$, the coupling changes the scattering properties and the potential has to be taken into account.*

lower lying (red) potential has an asymptotic energy $E_\infty = \lim_{r\to\infty} V(r)$ smaller than the relative kinetic energy $E_{\mathrm{kin}}$ of the atoms, for the other (blue) one $E_\infty > E_{\mathrm{kin}}$. Without coupling only the lower lying potential would contribute to the scattering amplitude. The internal quantum states corresponding to a potential with $E_\infty < E_{\mathrm{kin}}$ ($E_\infty > E_{\mathrm{kin}}$) define an open (closed) channel. The situation with only one open channel is realistic for cold atoms experiments, as the atoms are often prepared solely in one quantum state[6].

With coupling, for example due to exchange interaction or spin-spin interaction, the scattering properties are determined also by the closed channel. However, the scattering length $a$ is affected significantly only if a bound state of the closed channel is close to $E_{\mathrm{kin}}$. If this is not naturally the case, a difference in the magnetic moments of open and closed channel $\mu_{\mathrm{res}} = \mu_{\mathrm{closed}} - \mu_{\mathrm{open}}$ can be used to vary the relative energy between the channels with a magnetic field $B$ and to bring a bound state close to $E_{\mathrm{kin}}$. The atoms can then undergo a *virtual transition* to this bound state. The duration of the transition scales with the inverse of the energy difference between bound state energy $E_{\mathrm{b}}$ and $E_{\mathrm{kin}}$ [49]. If $E_{\mathrm{b}} - E_{\mathrm{kin}}$ is tuned with $B$ to small values, the virtual molecule lives long compared to the time the scattering process takes. This has a dramatic effect on the scattering properties. In the vicinity of a resonance the scattering length $a$ varies as

$$a(B) = a_{\mathrm{bg}}\left(1 - \frac{\Delta B}{B - B_{\mathrm{res}}}\right), \tag{2.27}$$

where $B_{\mathrm{res}}$ is the resonance position, $\Delta B$ is the resonance width and $a_{\mathrm{bg}}$ is the scattering length with no bound state close (see Fig. (2.5)). At $B_{\mathrm{res}}$ the scattering length diverges. It goes to $+\infty$ when approaching the resonance from below $B_{\mathrm{res}}$ ($E_{\mathrm{bound}} < E_{\mathrm{kin}}$) and to $-\infty$ when approaching from above ($E_{\mathrm{bound}} < E_{\mathrm{kin}}$).

Hence, a Feshbach resonance allows in principle to tune the scattering length to any positive or negative value. Nevertheless, the scattering cross section is limited and reaches a constant value proportional to $\lambda_{\mathrm{th}}^2$ and independent of $a$ for $|a| \gg \lambda_{\mathrm{th}}$. This limit is called the unitarity

[6] Provided that the atoms cannot undergo transitions to other states during the collision.

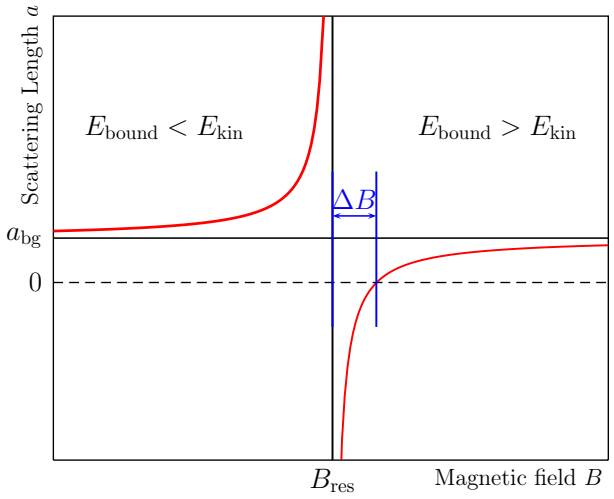


**Figure 2.5.:** *Variation of the scattering length in the vicinity of a Feshbach resonance. At the position of the resonance $B_{\text{res}}$ the scattering length diverges. The resonance width $\Delta B$, defined as the magnetic field difference between $B_{\text{res}}$ and the zero crossing of $a$, depends on the coupling strength between open and closed channel.*

limit (see for example [55]). The width of the resonance $\Delta B$ is defined as the magnetic field difference between $B_{\text{res}}$ and the zero crossing of $a$. It depends on the coupling strength, which means that a broad resonance corresponds to a strong coupling between open and closed channel. In fact, the resonance position $B_{\text{res}}$ does not coincide with the crossing of $E_{\text{b}}$ and $E_{\text{kin}}$, because the coupling leads to a shift. It induces a mixing of open and closed channel states resulting in a Landau-Zener type behavior of the energies of these mixed states. The details of this are discussed in the next section.

In the vicinity of a Feshbach resonance not only the probability for elastic collisions increases, also inelastic three-body collisions are more likely. In a three-body collision a molecule is formed with the participation of a third atom. Without the third atom, which carries away a part of the momentum, energy and momentum could not be conserved at the same time. The binding energy of the molecule is set free as kinetic energy in the process. As the binding energy is usually much larger than the trap depth, both molecule and atom are lost from the trap. If both background collisions and two-body losses are neglected, the relation

$$\dot{n} = -L_3 n^3 \tag{2.28}$$

holds for the decrease of the atomic density with time. The three-body loss coefficient scales universally like $L_3 \propto a^4$ for scattering lengths much larger than the characteristic interaction range of the atoms [56]. This relation predicts thus enhanced inelastic losses close to a Feshbach resonance, where $a$ diverges. But also on the side of a resonance where the scattering length decreases strongly enhanced losses are observed [57]. This enhancement has to be explained with a different theoretical treatment of the ultra-cold three-body collisions (see for example [58]). Due to the dependence of $\dot{n}$ on the third power of $n$, at the high atomic densities reached in a Bose-Einstein condensate (on the order of $10^{14}$ cm$^{-3}$) the losses can be so large that they prevent a crossing of a Feshbach resonance without destroying the quantum degeneracy.

## 2.3. Theory of Feshbach Resonances

To derive a theoretical description of Feshbach resonances, this section recapitulates scattering theory taking into account a coupling between different molecular potentials. Only one bound state is considered, which is the single resonance approach. The presentation follows mainly [49] and [59]. For more details the reader is referred also to [54, 60].

### 2.3.1. Formal Solution

As explained in the previous section, a coupling between open and closed channel is crucial for a Feshbach resonance. This coupling leads to a mixing of the open and the closed channel state $|\psi_{\mathrm{op}}\rangle$ and $|\psi_{\mathrm{cl}}\rangle$. The *scattering state* has thus the following general form

$$|\psi\rangle = \alpha\,|\psi_{\mathrm{op}}\rangle + \beta\,|\psi_{\mathrm{cl}}\rangle\ . \tag{2.29}$$

As was done in section 2.1, we calculate the stationary scattering eigenstate with the time-independent Schrödinger equation. Though, we now have two coupled differential equations due to the coupling [59]

$$H_{\mathrm{op}}\,|\psi_{\mathrm{op}}\rangle + W\,|\psi_{\mathrm{cl}}\rangle = E\,|\psi_{\mathrm{op}}\rangle\ , \tag{2.30}$$

$$H_{\mathrm{cl}}\,|\psi_{\mathrm{cl}}\rangle + W\,|\psi_{\mathrm{op}}\rangle = E\,|\psi_{\mathrm{cl}}\rangle\ , \tag{2.31}$$

and two scattering eigenstates[7] $|\psi^{\mathrm{op}}_{\boldsymbol{k}}\rangle$ and $|\psi^{\mathrm{cl}}_{\boldsymbol{k}}\rangle$. Here $H_{\mathrm{op}}$ (respectively $H_{\mathrm{cl}}$) is the Hamilton operator for the open (respectively closed) channel without coupling and $W$ denotes the coupling. $H_{\mathrm{op}}$ is thus equal to Eq. (2.5).

$H_{\mathrm{cl}}$ is of the same form as $H_{\mathrm{op}}$, but its potential energy is given by the closed channel potential $V_{\mathrm{cl}}(\boldsymbol{r})$. The eigenfunctions of interest of $H_{\mathrm{cl}}$ are all bound states, because the asymptotic energy of $V_{\mathrm{cl}}(\boldsymbol{r})$ is larger than the relative kinetic energy of the atoms. $H_{\mathrm{cl}}$ can therefore be written as

$$H_{\mathrm{cl}} = \sum_{\nu} E_\nu\,|\psi_\nu\rangle\,\langle\psi_\nu|\ , \tag{2.32}$$

with the bound states $|\psi_\nu\rangle$ and their energy $E_\nu$. This allows us to write Eq. (2.31) as

$$\sum_{\nu}(E - E_\nu)\,|\psi_\nu\rangle\,\langle\psi_\nu|\,\psi_{\mathrm{cl}}\rangle = W\,|\psi_{\mathrm{op}}\rangle\ . \tag{2.33}$$

We are interested in the behavior of $a$ when a bound state is close to the relative kinetic energy $E_{\mathrm{kin}}$ of the atoms. Therefore we can neglect all eigenstates of $H_{\mathrm{cl}}$ other than $|\psi_{\mathrm{b}}\rangle$, the bound state that is close to $E_{\mathrm{kin}}$. Consequently Eq. (2.33) can be rewritten as

$$(E - E_{\mathrm{b}})\,|\psi_{\mathrm{b}}\rangle\,\langle\psi_{\mathrm{b}}|\,\psi_{\mathrm{cl}}\rangle = W\,|\psi_{\mathrm{op}}\rangle\ . \tag{2.34}$$

This approach is called the single resonance approximation.

To get to a formal solution of the coupled Schrödinger equations (2.30) and (2.31), the concept of Green's functions — in this case Green's operators — is used like in the previous

[7] Also called dressed states.

section. With the Green's operators

$$G_{\mathrm{op}}(z) = \frac{1}{z - H_{\mathrm{op}}}, \tag{2.35}$$

$$G_{\mathrm{cl}}(z) = \frac{1}{z - H_{\mathrm{cl}}}, \tag{2.36}$$

where $z$ is a complex number with the dimension of an energy, the scattering states become [49]

$$|\psi_{\boldsymbol{k}}^{\mathrm{op}}\rangle = |\psi_{\boldsymbol{k}}\rangle + G_{\mathrm{op}}(E + i\epsilon) W \left|\psi_{\boldsymbol{k}}^{\mathrm{cl}}\right\rangle , \tag{2.37}$$

$$\left|\psi_{\boldsymbol{k}}^{\mathrm{cl}}\right\rangle = G_{\mathrm{cl}}(E) W |\psi_{\boldsymbol{k}}^{\mathrm{op}}\rangle . \tag{2.38}$$

Let us first discuss expression (2.37): $|\psi_{\boldsymbol{k}}\rangle$ is the solution of Eq. (2.30) without coupling $W$ and therefore in position-space given by Eq. (2.15). The argument $z = E + i\epsilon$ of the Green's operator ensures that the second term has the asymptotic behaviour of an *outgoing* spherical wave. Equation (2.38) has no scattered component[8] for $W = 0$, because for $H_{\mathrm{cl}}$ exist only bound states, as was stated above. In this equation we can include the single resonance approximation. The Green's operator $G_{\mathrm{cl}}(E)$ becomes then

$$G_{\mathrm{cl}}(E) = \frac{1}{(E - E_{\mathrm{b}}) |\psi_{\mathrm{b}}\rangle \langle\psi_{\mathrm{b}}|} = \frac{|\psi_{\mathrm{b}}\rangle \langle\psi_{\mathrm{b}}|}{(E - E_{\mathrm{b}})} . \tag{2.39}$$

Consequently $\left|\psi_{\boldsymbol{k}}^{\mathrm{cl}}\right\rangle$ is proportional to $|\psi_{\mathrm{b}}\rangle$

$$\left|\psi_{\boldsymbol{k}}^{\mathrm{cl}}\right\rangle = |\psi_{\mathrm{b}}\rangle \frac{\langle\psi_{\mathrm{b}}| W |\psi_{\boldsymbol{k}}^{\mathrm{op}}\rangle}{E - E_{\mathrm{b}}} . \tag{2.40}$$

If we now insert (2.40) into (2.37), after some algebra an expression for $|\psi_{\boldsymbol{k}}^{\mathrm{op}}\rangle$ is obtained, which depends only on the states $|\psi_{\boldsymbol{k}}\rangle$ and $|\psi_{\mathrm{b}}\rangle$

$$|\psi_{\boldsymbol{k}}^{\mathrm{op}}\rangle = |\psi_{\boldsymbol{k}}\rangle + G_{\mathrm{op}} \frac{W |\psi_{\mathrm{b}}\rangle \langle\psi_{\mathrm{b}}| W}{E - E_{\mathrm{b}} - \langle\psi_{\mathrm{b}}| W G_{\mathrm{op}} W |\psi_{\mathrm{b}}\rangle} |\psi_{\boldsymbol{k}}\rangle . \tag{2.41}$$

### 2.3.2. Derivation of the Scattering Properties

With Eq. (2.41) the scattering properties in the vicinity of a Feshbach resonance are deduced. Only *zero-energy resonances* are considered, which means $E_{\mathrm{kin}} = 0$. Here the zero of energy is set as the dissociation threshold of the open channel. As already discussed above, the first term on the right hand side of Eq. (2.41) describes the scattering in the open channel with no coupling $W$. The scattering length corresponding to this is called background scattering length $a_{\mathrm{bg}}$. The resonance behaviour of $a$ is caused by the second term of Eq. (2.41). The scattering amplitude, given by its asymptotic behaviour, diverges when the denominator vanishes, i.e. if

$$E = E_{\mathrm{b}} + \langle\psi_{\mathrm{b}}| W G_{\mathrm{op}} W |\psi_{\mathrm{b}}\rangle . \tag{2.42}$$

[8] Hence, z is chosen real.

For small $E$ the second term on the right hand side of Eq. (2.42) becomes [49]

$$\begin{aligned} \langle\psi_\mathrm{b}|\, WG_\mathrm{op}W\,|\psi_\mathrm{b}\rangle &= \langle\psi_\mathrm{b}|\, W\frac{1}{E-H_\mathrm{op}+i\epsilon}W\,|\psi_\mathrm{b}\rangle \\ &\overset{E\to 0}{\approx} \sum_{\boldsymbol{k}} \frac{|\,\langle\psi_\mathrm{b}|\, W\,|\psi_{\boldsymbol{k}}\rangle\,|^2}{-\frac{\hbar^2\boldsymbol{k}^2}{2m_\mathrm{r}}+i\epsilon} := \hbar\Delta_0\,. \end{aligned} \tag{2.43}$$

The approximate expression for $\langle\psi_\mathrm{b}|\, WG_\mathrm{op}W\,|\psi_\mathrm{b}\rangle$ has a form that is well-known from perturbation theory[9]. The expression describes the shift of the resonance position due to second order coupling induced by $W$ on $|\psi_\mathrm{b}\rangle$. Consequently the resonance does not occur when $E_\mathrm{b}$ is close to zero, but when

$$E_\mathrm{res} = E_\mathrm{b} + \hbar\Delta_0 = 0\,. \tag{2.44}$$

As was already stated in the previous section, the energy difference between open and closed channel is tunable with a magnetic field $B$, if the two states have a difference in magnetic moment $\mu_\mathrm{res} = \mu_\mathrm{closed} - \mu_\mathrm{open}$. Hence, $E_\mathrm{b} = E_\mathrm{b}(B) = \mu_\mathrm{res}(B - B_\mathrm{b})$, where $B_\mathrm{b}$ is the magnetic field value at which $E_\mathrm{b} = E_\mathrm{kin}$. Therefore the magnetic field value $B_\mathrm{res}$ that corresponds to the resonance position is defined by

$$B_\mathrm{res} = B_\mathrm{b} + \frac{\hbar\Delta_0}{\mu_\mathrm{res}}\,. \tag{2.45}$$

To get an expression for the total scattering amplitude $f_\mathrm{tot}$, we include Eq. (2.44) in Eq. (2.41) and multiply with $\langle\boldsymbol{r}|$ from the left, which gives the total scattered wave function

$$\psi^\mathrm{op}_{\boldsymbol{k}}(\boldsymbol{r}) = \langle\boldsymbol{r}|\,\psi^\mathrm{op}_{\boldsymbol{k}}\rangle = \psi_{\boldsymbol{k}}(\boldsymbol{r}) + \frac{\langle\boldsymbol{r}|\, G_\mathrm{op}W\,|\psi_\mathrm{b}\rangle\,\langle\psi_\mathrm{b}|\, W\,|\psi_{\boldsymbol{k}}\rangle}{E-E_\mathrm{res}}\,. \tag{2.46}$$

It takes some effort to calculate the asymptotic behaviour of this expression [49], hence I only state the result

$$\psi^\mathrm{op}_0(\boldsymbol{r}) \overset{r\to\infty}{\approx} \psi_0(\boldsymbol{r}) + \frac{1}{r}\frac{4\pi^2 m_\mathrm{r}}{\hbar^2}\frac{|\,\langle\psi_0|\, W\,|\psi_\mathrm{b}\rangle\,|^2}{E_\mathrm{res}}\,, \tag{2.47}$$

here $E$ and $k$ are set to zero. The factor behind $1/r$ is the contribution $f_\mathrm{res}$ to the total scattering amplitude, thus we finally get to Eq. (2.27) for the scattering length

$$a(B) = -\lim_{k\to 0} f_\mathrm{tot} = a_\mathrm{bg} - \frac{4\pi^2 m_\mathrm{r}}{\hbar^2}\frac{|\,\langle\psi_0|\, W\,|\psi_\mathrm{b}\rangle\,|^2}{E_\mathrm{res}} = a_\mathrm{bg}\left(1 - \frac{\Delta B}{B-B_\mathrm{res}}\right)\,, \tag{2.48}$$

with the width of the resonance

$$\Delta B = \frac{4\pi^2 m_\mathrm{r}}{\hbar^2}\frac{|\,\langle\psi_0|\, W\,|\psi_\mathrm{b}\rangle\,|^2}{a_\mathrm{bg}\mu_\mathrm{res}}\,. \tag{2.49}$$

It depends on the coupling strength $W$ between open and closed channel, as already discussed in the previous section.

[9] Strictly speaking $\Delta_0$ has also an imaginary part due to $i\epsilon$. It can be shown that in the low-energy limit we can neglect this part which would lead to a damping term, because the density of states of the continuum of $H_\mathrm{op}$ vanishes near $k = 0$ [49].

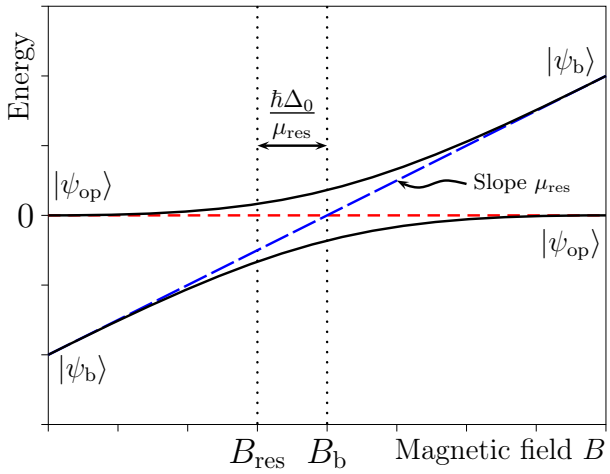


**Figure 2.6.:** *Avoided crossing of the bound state energy of the closed channel (blue dashed line) and the open channel energy (red dashed line). Due to the coupling the two states mix near the crossing to dressed states. The energies of these dressed states do not cross (black solid lines). This allows to produce weakly bound Feshbach molecules by ramping the magnetic field adiabatically from values above the resonance to values below (Landau-Zener transition). The coupling results also in a shift of the resonance position by $\hbar\Delta_0/\mu_{res}$.*

Figure 2.6 illustrates the results described above. It shows the energy dependence of the open (red dashed) and closed channel (blue dashed) energy and the dressed states energies (black solid lines). The open channel energy is set to zero, hence the closed channel energy increases with a slope given by $\mu_{res}$. The shift of the position of the singularity in $a$ is indicated for a negative $\hbar\Delta_0$. The Landau-Zener behaviour of the dressed states allows to produce molecules by sweeping the magnetic field over the resonance from above, similar to a radio-frequency sweep to transfer atoms between different magnetic states. The resulting Feshbach molecules are weakly bound with an binding energy depending on $B$ (see [59] for details on Feshbach molecules).

## 2.4. Feshbach Resonances of Chromium

Until now I did not talk about the details of the internal atomic structure that causes the coupling between various molecular potentials. This section summarizes experimental and theoretical work [12, 60, 61] on Chromium atoms ($^{52}$Cr), for which 14 resonances below 600 G have been found. The assignment of these resonances to internal quantum states allowed to determine the background scattering length $a_{bg}$ of Chromium atoms in the $^7S_3$ ground state with $M_S = -3$ to be $112(14)a_0$, where $a_0$ is the Bohr radius. $^{52}$Cr is a bosonic isotope with no nuclear spin $\boldsymbol{I}$ (see appendix B.1). This is a main difference to alkali atoms which are often used for experiments with ultra-cold atoms, as there is no hyperfine structure. It has an comparatively large magnetic dipole moment of 6 $\mu_B$, because the spins of the 6 outer electrons couples to a total spin $S = 3$.

The molecular interaction potential of $^{52}$Cr atoms consists of the following contributions

$$V_{\mathrm{mol}} = \sum_{k=1}^{2} V_{\mathrm{Z}}^{k} + V_{\mathrm{E}} + V_{\mathrm{vdW}} + V_{\mathrm{SS}} + V_{\mathrm{SO}} \,. \tag{2.50}$$

The various terms are:

**Zeeman interaction $V_{\mathrm{Z}}^{k}$:** The magnetic dipole moment of the atoms $k = 1, 2$ leads to a shift of their energy if a magnetic field $B$ is applied. It is given by the well-known formula

$$V_{\mathrm{Z}}^{k} = -\boldsymbol{\mu}_k \cdot \boldsymbol{B} = -\mu_{\mathrm{B}} g_J M_{J,k} B \,. \tag{2.51}$$

Here $M_{J,k}$ is the projection of the total angular momentum $\boldsymbol{J}_k$ of atom $k$ on the quantization axis defined by the magnetic field. The Landé-factor $g_J$ of the $^7\mathrm{S}_3$ ground state of Chromium is negative and close to the electron $g$ factor, namely $g_J = -2.00183$ [62]. The Zeeman interaction is crucial for Feshbach resonances, as it allows to shift molecular potentials with different projections of the dipole moment relative to each other.

**Exchange interaction $V_{\mathrm{E}}$:** The electronic exchange interaction has no classical analogy and has therefore to be described quantum mechanically [63]. It arises from the fact that the valence electrons cannot be allocated to a specific atom any more if the electron clouds overlap. It is a short range interaction because this overlap decays exponentially with the distance of the atoms. At small distances it is strongly repulsive because of the fermionic nature of electrons.

**Van der Waals interaction $V_{\mathrm{vdW}}$:** The atoms induce mutually an electric dipole moment if they are close. These dipole moments interact with each other, leading to an attractive potential falling of as $-C_6/r^6$. $C_6$ is the van der Waals coefficient determining the interaction strength. There exist also higher multipole contributions decaying as $-C_n/r^n$, with $n = 8$, 10, ....

**Spin-spin interaction $V_{\mathrm{SS}}$:** Also referred to as dipole-dipole interaction in this thesis. $V_{\mathrm{SS}}$ is the most important coupling interaction for $^{52}$Cr, as coupling due to exchange interaction does not lead to Feshbach resonances (see below). The potential energy is dependent on the relative alignment of the dipoles and falls of with $1/r^3$. For a polarized sample it is given by

$$V_{\mathrm{SS}} = \frac{\mu_0 \mu^2}{4\pi} \left( \frac{1 - 3\cos^2\theta}{r^3} \right) , \tag{2.52}$$

with the atomic dipole moment $\mu = g_J \mu_{\mathrm{B}} M_J$ and with $\theta$ being the angle between the magnetic field and the connection line between the atoms.

**Second order spin-orbit interaction $V_{\mathrm{SO}}$:** Besides the direct spin-spin interaction $V_{\mathrm{SS}}$, there is an indirect interaction between the spins, the second-order spin-orbit interaction $V_{\mathrm{SO}}$. It occurs when the atomic charge clouds overlap as a molecule is formed, and the interaction between the ground state spins are modified due to couplings mediated through

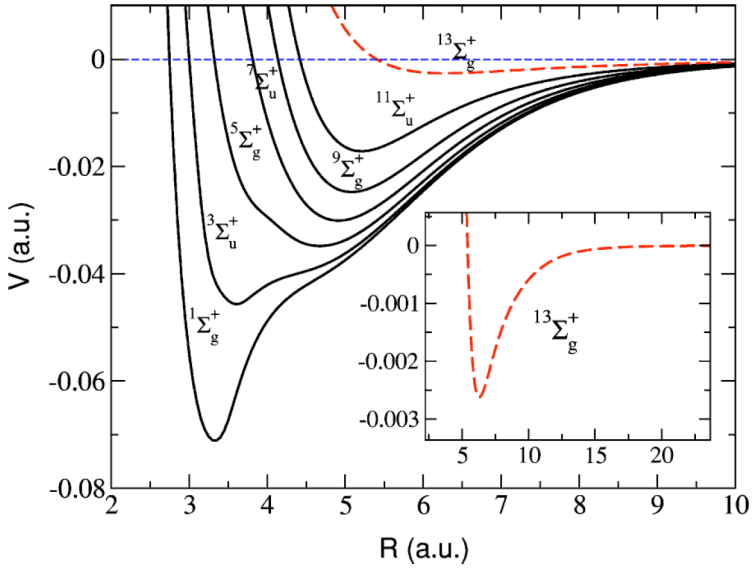


**Figure 2.7.:** *Molecular potentials of $^{52}$Cr resulting from theoretical ab-inito calculations for ground state atoms (see text for the notation of the molecular states). The total spin of the atoms can couple to values between 0 and 6 and therefore results in 7 potentials. The potential with molecular spin $S_M = 0$ has the strongest binding energy. The depth of the potentials decreases then for higher $S_M$ up to the comparatively shallow one with $S_M = 6$, which is shown in detail in the inset. Figure taken from [61].*

distant excited electronic states of the molecule [64]. For heavy species like Rb and Cs these indirect terms can be much larger than $V_{\mathrm{SS}}$ at short distances. However, for the discussion of the Feshbach resonances of Chromium it is not relevant and will not be discussed further.

Taking all these contributions into account leads to the potential curves shown in Fig. 2.7. These potentials are results of theoretical ab-inito calculations for $^{52}$Cr atoms in their ground state without an external magnetic field $B$ [61]. The interaction of two ground state $^{52}$Cr atoms is best described by Hund's case (a), i.e. a strong coupling of the motion of the electrons to the internuclear axis. This means, that the quantum numbers of the orbital angular momenta $\boldsymbol{L}_k$ and of the spins $\boldsymbol{S}_k$ of the atoms are no good quantum numbers any more. Instead, the quantum numbers of the projection of these quantities on the internuclear axis have to be used [65]. This leads to the notation $^{2S_M+1}\Lambda^{\sigma}_{\pi_e}$ for the different molecular states, where $\Lambda = |\sum_k M_{L,k}|$ and $S_M = |\sum_k M_{S,k}|$. $\Lambda$ is 0 (denoted with $\Sigma$) for two atoms in the $^7$S$_3$ ground state, whereas $S_M$ can take values between 0 and 6, resulting in seven different potentials. The parity of the wave functions corresponding to these potentials is denoted with $\pi_e = $ g, u (for gerade, ungerade) and their symmetry upon reflection at a plane through the internuclear axis with $\sigma = +, -$.

In our experiment we start with a spin polarized sample of atoms in the $^7$S$_3$ ground state with $M_S = -3$. When two colliding atoms are still far apart, the total orbital angular momentum $\boldsymbol{L}$ and the total spin $\boldsymbol{S}$ of the dimer are still good quantum numbers, with $M_L$ and $M_S$ being the projection on the magnetic field $\boldsymbol{B}$, which is required to keep the sample polarized. In the course of the collision, the total projection $M = M_L + M_S$ and the parity

| | $1^{\text{st}}$ order | $2^{\text{nd}}$ order |
|---|---|---|
| $\Delta L$ | 0, ±2 | 0, ±2, ±4 |
| $\Delta M_L$ | 0, ±1, ±2 | 0, ±1, ±2, ±3, ±4 |
| $\Delta S$ | 0, ±2 | 0, ±2, ±4 |

**Table 2.1.:** *Selection rules for a first and second order dipole-dipole transition.* $\Delta M_L = 0$ *is not allowed for* $L = 0 \rightarrow L' = 0$ *in first order.*

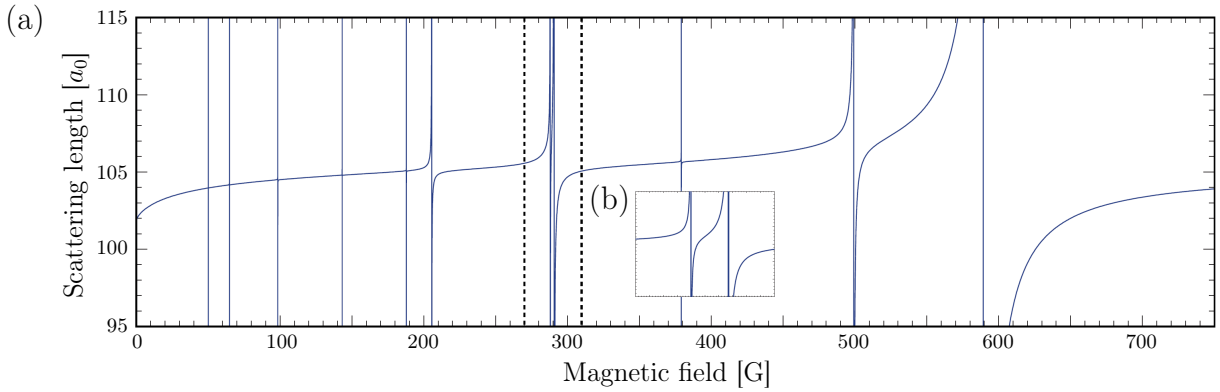


**Figure 2.8.:** *(a) Theoretical prediction of the variation of the scattering length a of* $^{52}Cr$ *with an applied magnetic field B. The scattering length shows singular behaviour at the position of the 14 Feshbach resonances below 600 G. Except the resonances at* 290.3*,* 499.9 *and* 589.1 *G, all resonances are due to second order coupling and therefore narrow. Around 290 G two resonances almost coincide. This double structure is resolved in the inset (b). Figure taken from [60].*

$(-1)^L$ are conserved [60]. The symmetrization needed because the nuclei of the atoms are identical leads to an exclusion of states with $(-1)^{S+L} \neq 1$. Only $V_{\text{E}}$, $V_{\text{SS}}$ and $V_{\text{SO}}$ lead to a coupling. The exchange interaction $V_{\text{E}}$ is the dominating coupling term for alkali atoms, but does not lead to Feshbach resonances for Chromium. $V_{\text{E}}$ conserves $M_S$ and therefore the Zeeman energy of open and closed channel are equal. Of the two remaining terms the spin-spin interaction $V_{\text{SS}}$ is much stronger and $V_{\text{SO}}$ can be neglected. Therefore the selection rules of $V_{\text{SS}}$, in addition to the rules described above, determine which states lead to a Feshbach resonance. Table 2.1 summarizes all possible first and second order transitions for $L$, $M_L$ and $S$. Taking this into account allowed to assign quantum numbers to 13 out of 14 Feshbach resonances that were found experimentally in 2004 [12]. Figure 2.8 shows the resulting scattering length $a(B)$. Most of the resonances are due to second order coupling and thus quite narrow. Only three first order resonances occur, of which the broadest is at 589.1 G. This resonance is used to tune the scattering length $a$ (see chapter 5). For more details on the Feshbach resonances of Chromium, for example on the assignment procedure, the reader is referred to [60].

# 3. Dipolar Bose-Einstein Condensates

*Chromium has an comparatively large magnetic dipole moment of 6 $\mu_B$. Hence, a theoretical description of a Chromium Bose-Einstein condensate has to include also dipole-dipole interaction. This chapter discusses an extension of the mean-field theory for condensates with only contact interaction to dipolar condensates. In the first two sections the theory including only contact interaction is described. Section 3.1 reports on the in-trap properties of such a condensate. The mean-field approximation and the Thomas-Fermi regime are introduced. The theoretical description of the condensate dynamics by hydrodynamic equations is discussed in section 3.2. Finally, section 3.3 includes dipole-dipole interaction in this theory. All important results that are used for the data evaluation are presented.*

## 3.1. Bose-Einstein Condensation

The new state of matter called Bose-Einstein condensate (BEC) that was first realized in 1995 in the group of Wieman and Cornell [6] and shortly afterwards in the group of Ketterle [7], had been predicted already 70 years before by Einstein [14]. Bose-Einstein condensation is based on the *indistinguishability* and *wave nature* of particles [66]. The phase transition from a thermal gas of trapped bosonic atoms to a condensate appears, when the thermal de Broglie wavelength $\lambda_{\mathrm{th}}$ (Eq. (2.1)) starts to be on the order of the mean atomic distance (given approximately by $n^{-1/3}$, where $n$ is the particle density). Therefore the wave functions of the atoms start to overlap and the indistinguishability becomes important: Bosons accumulate in the ground state which leads to a collective macroscopic behaviour of the atoms (see Fig. 3.1). The sample can then be described by one macroscopic wave function with a fixed phase throughout the whole sample. BECs are a macroscopic probe to study quantum phenomena, which explains the huge interest they have attracted over the last years.

### 3.1.1. Statistical Description

Before I introduce the mean-field description, I summarize important results of the statistical description of Bose-Einstein condensation. For a derivation of these results see for example [54, 55, 67] or standard textbooks on statistical physics [68, 69]. For a Bose gas without interactions in a box with periodic boundary conditions, the phase transition to a condensate appears when the phase space density, defined as $\rho := n\lambda_{\mathrm{th}}^3$, is equal to[1] $\zeta(3/2) \approx 2.612$. This corresponds to a critical temperature

$$T_{\mathrm{c}}^{\mathrm{box}} = \frac{2\pi\hbar^2}{m k_{\mathrm{B}}} \left( \frac{n}{\zeta(3/2)} \right)^{2/3} . \tag{3.1}$$

[1] Here $\zeta(x)$ is the Riemann Zeta function, defined as $\zeta(x) = \sum_{k=1}^{\infty} k^{-x}$.

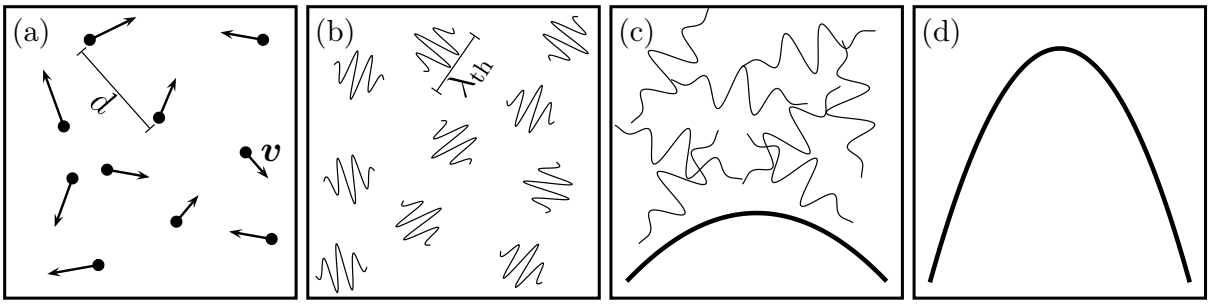


**Figure 3.1.:** *Illustration of Bose-Einstein condensation. (a) At high temperatures $T$ the atomic gas is treated in a particle picture. The atoms act like 'billiard balls' with a Maxwell-Boltzmann velocity distribution. The mean distance $d$ is approximately $n^{-1/3}$. (b) If the temperature is lowered, the wave nature of the atoms gets apparent. The thermal de Broglie length is still too small to lead to an overlap of the different wave packets. (c) At $T = T_{\mathrm{c}}$ the wave packets start to overlap and the atoms accumulate in the ground state. (d) At $T = 0$ the condensate is pure, all atoms are in the ground state. A 'giant matter wave' is formed. Figure similar to [66].*

At $T = T_{\mathrm{c}}^{\mathrm{box}}$ a macroscopic number of atoms start to occupy the motional ground state $|\phi_0\rangle$. The condensate fraction, i.e. the ratio of ground state atoms all atoms, is

$$\frac{N_0(T)}{N} = 1 - \left(\frac{T}{T_{\mathrm{c}}^{\mathrm{box}}}\right)^{3/2} . \tag{3.2}$$

These properties change when the realistic case of trapped atoms is considered. For the simple and often realized case of a harmonic trap the condensate fraction is given by

$$\frac{N_0(T)}{N} = 1 - \left(\frac{T}{T_{\mathrm{c}}}\right)^{3} , \tag{3.3}$$

with the critical temperature

$$T_{\mathrm{c}} = \frac{\hbar\omega_{\mathrm{ho}}}{k_{\mathrm{B}}} \left(\frac{N}{\zeta(3)}\right)^{1/3} . \tag{3.4}$$

The trap geometry enters the formula for the critical temperature through the geometric mean of the trapping frequencies in $x$, $y$ and $z$ direction

$$\omega_{\mathrm{ho}} = (\omega_x \omega_y \omega_z)^{1/3} . \tag{3.5}$$

For typical experimental parameters the critical temperature is on the order of a few 10 nK to 1 $\mu$K. Here it should be stressed that at $T_{\mathrm{c}}$ the level spacing in the trap, $\hbar\omega_{\mathrm{ho}}$, is still 10 to 100 times smaller than the thermal energy $k_{\mathrm{B}}T$. Bose-Einstein condensation is a *statistical* effect.

### 3.1.2. Mean-Field Approximation and Thomas-Fermi Limit

The results discussed above are not exactly valid anymore if the atoms interact with each other. I do not discuss the influence of the interaction on the critical temperature and the condensate fraction as this effect corresponds only to a few percent change (see for

example [54]). Nevertheless, the interaction is important for the structure of a BEC. The many-body hamiltonian of a cloud of interacting atoms includes the potential energy between each pair of atoms. Typical BECs contain $10^4$–$10^6$ atoms, it is clear that the many-body problem can thus not be solved exactly. Because BECs are dilute gases with $n|a|^3 \ll 1$ for sufficiently small interaction, we can neglect the correlations between the atoms and assume that they move in a *mean-field* potential created by the other atoms. The mean-field potential has to be defined in a self-consistent way. This mean-field approximation simplifies the theoretical description vastly.

In the fully condensed state ($T = 0$) all atoms occupy the same motional ground state $|\phi_0\rangle$. In the mean field approximation the whole condensate is then described by one wave function[2]. It is useful to define the wave function as

$$\psi(\boldsymbol{r}) := \sqrt{N}\phi_0(\boldsymbol{r})\,, \tag{3.6}$$

because then the particle density $n(\boldsymbol{r})$ is given by $|\psi(\boldsymbol{r})|^2$. A non-linear Schrödinger equation for this wave function, the (time-independent) *Gross-Pitaevskii equation* (GPE), is obtained by using variational methods [54]

$$\left(-\frac{\hbar^2}{2m}\boldsymbol{\nabla}^2 + V_{\text{ext}}(\boldsymbol{r}) + g|\psi(\boldsymbol{r})|^2\right)\psi(\boldsymbol{r}) = \mu\psi(\boldsymbol{r})\,. \tag{3.7}$$

Here $m$ is the atomic mass, $V_{ext}(\boldsymbol{r})$ is the confining potential and $\mu$ is the chemical potential of the system, i.e. the energy needed to add a particle to the system. The derivation of Eq. (3.7) makes use of the simple pseudo-potential introduced in section 2.1 to describe the atom-atom interaction. This leads to the mean-field interaction term $gn(\boldsymbol{r}) = g|\phi(\boldsymbol{r})|^2$. As already stated above, dipole-dipole interaction is first not taken into account. Equation (3.7) is the key tool in the mean field description of BECs.

The GPE simplifies a lot if the kinetic energy term is neglected. The kinetic energy is caused by the confinement of the atoms due to the Heisenberg principle. It can be shown (see for example [54]) that for large atom numbers and repulsive interaction the kinetic energy is negligible[3]. This regime is called *Thomas-Fermi limit*, it is valid if

$$\frac{Na}{a_{\text{ho}}} \gg 1\,, \tag{3.8}$$

where $a_{\text{ho}} = \sqrt{\hbar/(m\omega_{\text{ho}})}$ is the oscillator length of the trapping potential. In this case we directly obtain a solution of the GPE

$$n(\boldsymbol{r}) = |\psi(\boldsymbol{r})|^2 = \begin{cases} \dfrac{\mu - V_{\text{ext}}(\boldsymbol{r})}{g} & : \quad V_{\text{ext}}(\boldsymbol{r}) \leq \mu \\ 0 & : \quad \text{otherwise} \end{cases}\,. \tag{3.9}$$

The density profile of the BEC reflects the shape of the confining potential. For harmonic traps it is thus parabolic (see Fig. 3.2). With the Thomas-Fermi radii, which are defined by

[2] Please note that the wave function is the order parameter of the BEC phase transition.

[3] It is intuitively clear that for repulsive interaction the size $R$ of the BEC increases and hence the kinetic energy ($\sim \hbar^2/(mR^2)$) decreases.

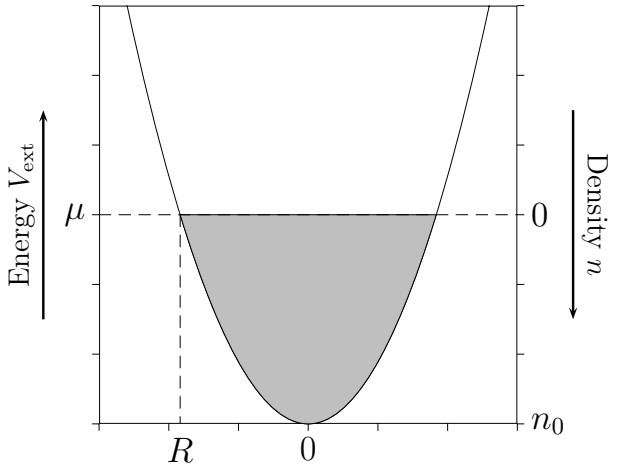


**Figure 3.2.:** *Potential energy $V_{\text{ext}}$ and density n in the Thomas-Fermi limit. The density profile has the inverted shape of the harmonic trapping potential. The trap is 'filled' up to the Thomas-Fermi radius R, where $V_{\text{ext}} = \mu$.*

$$R_i := \sqrt{\frac{2\mu}{m\omega_i^2}}\,, \quad i = x, y, z\,, \tag{3.10}$$

we can express Eq. (3.9) like

$$n(\boldsymbol{r}) = \max\left\{ n_0 \left( 1 - \sum_i \left( \frac{x_i}{R_i} \right)^2 \right), 0 \right\}, \tag{3.11}$$

with the peak density $n_0 = \mu/g$. The normalization of the wave function $\psi(\boldsymbol{r})$ allows us to express the chemical potential in terms of atom number $N$, trapping frequencies $\omega_i$ and scattering length $a$:

$$\mu = \frac{1}{2}\hbar\bar{\omega} \left( \frac{15Na}{a_{\text{ho}}} \right)^{2/5}. \tag{3.12}$$

Hence, the Thomas-Fermi radii scale as $(Na)^{1/5}$. To get the typical size of a condensate, we assume $N = 10^5$, $\omega_{\text{ho}} = 2\pi \times 100$ Hz and $a = 100\ a_0$. With the mass of Chromium $m = 8.7 \times 10^{-26}$ kg, this gives $R \approx 8\ \mu$m.

## 3.2. Hydrodynamic Description of the Condensate Dynamics

The previous section showed that the typical in-trap size of a BEC is on the order of a few $\mu$m. This is close to the resolution limit of the light that is used to image the condensate. Therefore condensates are usually imaged after a short time of free expansion (a few ms). This time-of-flight simplifies the detection and reveals information on the gas properties, like the mean-field interaction energy. The free expansion of a condensate is described by a

*scaling law*. It is deduced by reformulating the time-dependent GPE

$$-i\hbar\frac{\partial}{\partial t}\psi(\boldsymbol{r},t)=\left(-\frac{\hbar^2}{2m}\boldsymbol{\nabla}^2+V_{\text{ext}}(\boldsymbol{r},t)+g|\psi(\boldsymbol{r},t)|^2\right)\psi(\boldsymbol{r},t) \tag{3.13}$$

as a set of hydrodynamic equations. For this, we rewrite the condensate wave function Eq. (3.6) in polar form

$$\psi(\boldsymbol{r},t)=\sqrt{n(\boldsymbol{r},t)}e^{i\alpha(\boldsymbol{r},t)}\,, \tag{3.14}$$

where $\alpha(\boldsymbol{r},t)$ is the phase of the condensate. After some algebra (see for example [67]) the following expressions are obtained

$$\frac{\partial n}{\partial t} = -\boldsymbol{\nabla}\cdot(n\boldsymbol{v}) \tag{3.15}$$

$$m\frac{\partial \boldsymbol{v}}{\partial t} = -\boldsymbol{\nabla}\left(-\frac{\hbar^2}{2m}\frac{\Delta\sqrt{n}}{\sqrt{n}}+\frac{mv^2}{2}+V_{\text{ext}}+gn\right)\,. \tag{3.16}$$

Equation (3.15) has the form of a continuity equation and Eq. (3.16) is similar to the Euler equation for a *superfluid*. The superfluid velocity $\boldsymbol{v}(\boldsymbol{r},t)$ is proportional to the gradient of the phase

$$\boldsymbol{v}(\boldsymbol{r},t)=\frac{\hbar}{m}\boldsymbol{\nabla}\alpha(\boldsymbol{r},t)\,. \tag{3.17}$$

Hence, the condensate motion is equivalent to the potential flow of a superfluid[4] in the presence of $V_{\text{ext}}$ and the mean field potential $gn$. A difference in Eq. (3.16) to classical hydrodynamics is the *quantum pressure* term

$$-\frac{\hbar^2}{2m}\frac{\Delta\sqrt{n}}{\sqrt{n}}\,. \tag{3.18}$$

It can be estimated by

$$\frac{\Delta\sqrt{n}}{\sqrt{n}}\sim\frac{1}{d^2}\,, \tag{3.19}$$

where $d$ denotes the typical length scale for the variation of the condensate density $n(\boldsymbol{r})$ [67]. Like the term $mv^2/2$ it originates from the kinetic energy of the condensate, but it corresponds to a different physical effect: Whereas $mv^2/2$ describes the kinetic energy of the particle motion, Eq. (3.18) describes the zero point motion (hence the name quantum pressure) [54]. For a moderate excitation of the condensate or in the course of ballistic expansion, $d$ is on the order of the size of the condensate itself. It can be shown that the quantum pressure term is then negligible in the Thomas-Fermi regime [67].

Thus, the condensate motion is described by a set of classical hydrodynamic equations in this regime. In this model each particle experiences a force

$$\boldsymbol{F}(\boldsymbol{r},t)=-\boldsymbol{\nabla}(V_{\text{ext}}(\boldsymbol{r},t)+gn(\boldsymbol{r},t))\,. \tag{3.20}$$

At $t=0$ the system is assumed to be in steady state, meaning that the density distribution is given by Eq. (3.9). If $V_{\text{ext}}$ is then switched off, the condensate motion corresponds to a

[4]The velocity potential is given by $\hbar\alpha/m$.

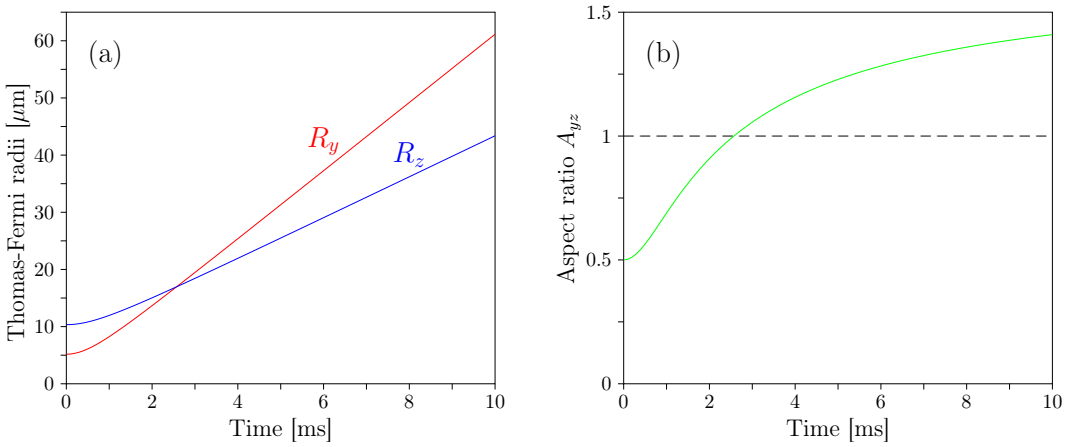


**Figure 3.3.:** *(a) Thomas-Fermi radii $R_y(t)$ and $R_z(t)$ after sudden switch-off of a trap with $(\omega_x, \omega_y, \omega_z) = 2\pi \times (200, 200, 100)$ Hz. At approximately 2.3 ms the ellipticity of the condensate inverts. (b) The aspect ratio $A_{yz}$ crosses 1 at this time.*

dilatation of the cloud, with any small piece of the fluid moving along the trajectory

$$R_i(t) = \lambda_i(t) R_i(0)\,, \tag{3.21}$$

where $R_i(0)$ are the initial Thomas-Fermi radii. An exact solution of the dynamics of the condensate can be calculated for harmonic potentials [70]. In this case the $\lambda_i(t)$ fulfill the following coupled differential equations[5]

$$\ddot{\lambda}_i = \frac{1}{\lambda_x \lambda_y \lambda_z} \frac{\omega_i^2(0)}{\lambda_i} - \omega_i^2(t)\lambda_i\,, \quad i = x, y, z\,. \tag{3.22}$$

Figure 3.3 (a) shows how the Thomas-Fermi radii $R_y$ and $R_z$ evolve after a sudden switch-off of a trap with $(\omega_x, \omega_y, \omega_z) = 2\pi \times (200, 200, 100)$ Hz. Starting at $t = 0$ with a quadratic behavior, the radii increase almost linearly for times $t > 1/\omega_i$. The slope of $R_y$ is steeper, leading to a crossing of the radii after approximately 2.3 ms: The condensate inverts its ellipticity. Unless the ratio $\omega_y/\omega_z$ is initially exactly one, the condensate always inverts its ellipticity[6], i.e. the aspect ratio $A_{yz}(t) = R_y/R_z$ changes from values smaller (larger) than one to values larger (smaller) than one (see Fig. (3.3) (b)). This is a 'smoking gun' evidence for quantum degeneracy. It can be easily understood in the classical hydrodynamics model. The density gradient $\boldsymbol{\nabla} n(\boldsymbol{r})$ is larger in the direction of higher trapping frequencies, leading to a faster acceleration in this direction (see Eq. (3.20)).

[5] The equations are exact not only for a sudden switch-off, but for any change of the external potential at $t = 0$.

[6] If only contact interaction is present.

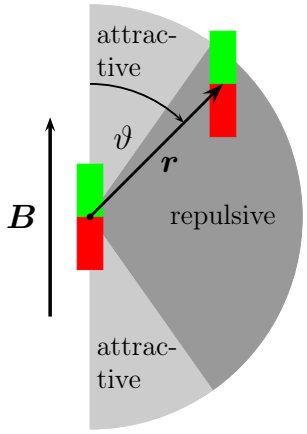


**Figure 3.4.:** *Anisotropy of the dipole-dipole interaction. Due to the angular dependence of* $V_{\mathrm{dd}}(\boldsymbol{r})$ *the interaction is attractive for* $0 \leq \cos\vartheta < \sqrt{1/3}$ *and* $(\pi - \sqrt{1/3}) < \cos\vartheta \leq \pi$*, and repulsive for* $\sqrt{1/3} < \cos\vartheta \leq (\pi - \sqrt{1/3})$*.*

## 3.3. Dipole-Dipole Interaction in a Bose-Einstein Condensate

An important difference of $^{52}$Cr compared to other atomic species condensed to date is the large magnetic dipole moment of 6 $\mu_{\mathrm{B}}$. As already explained in section 2.4, the spins of the 6 outer electrons couple to a total spin of 3, leading to the comparatively large dipole moment. This property of Chromium enabled Stuhler and coworkers [10] in 2005 to show for the first time dipolar effects in a quantum gas. For other species the dipolar effects are masked by the contact interaction, as the relative strength of dipole-dipole to contact interaction is too small. A useful dimensionless parameter to measure the relative strength is

$$\varepsilon_{\mathrm{dd}} = \frac{\mu_0 m}{12\pi\hbar^2}\frac{\mu^2}{a}\,, \tag{3.23}$$

where $\mu$ is the atomic dipole moment and $a$ is the scattering length. The *dipolar parameter* $\varepsilon_{\mathrm{dd}}$ is defined in a way that a homogenous condensate is unstable if $\varepsilon_{\mathrm{dd}} \geq 1$. Alkali atoms, which are most commonly used for ultra-cold atoms experiments, have a dipole moment of 1 $\mu_{\mathrm{B}}$. Hence $\varepsilon_{\mathrm{dd}}$ of Chromium is 36 times larger, with $a$ being on the same order.

### 3.3.1. In-Trap Condensate Shape

The interaction potential between two dipoles that are aligned by an external magnetic field $B$,

$$V_{\mathrm{dd}}(\boldsymbol{r}) = \frac{\mu_0\mu^2}{4\pi}\left(\frac{1-3(\boldsymbol{e}_\mu\cdot\hat{\boldsymbol{r}})^2}{r^3}\right)\,, \tag{3.24}$$

is anisotropic. Here $\boldsymbol{e}_\mu$ is the unit vector in the magnetic field direction and $\hat{\boldsymbol{r}} = \boldsymbol{r}/r$. $V_{\mathrm{dd}}(\boldsymbol{r})$ is partially attractive and partially repulsive (see Fig. 3.4). Another major difference to the contact interaction is that it is long range due to its $1/r^3$ dependence. This means that it cannot be described by a simple pseudo-potential, the scattering length as defined

in Eq. (2.23) diverges[7] [26]. Although the dipole-dipole interaction differs significantly from contact interaction, it is relatively easy to include in the mean-field description of BECs. As stated in [71] (explicitly shown in [72]), the mean-field dipole-dipole potential entering the GPE has the intuitive form

$$V_{\mathrm{dd}}^{\mathrm{mean}}(\boldsymbol{r}) = \int \mathrm{d}r'^3 V_{\mathrm{dd}}(\boldsymbol{r}-\boldsymbol{r}')n(\boldsymbol{r}')\,. \tag{3.25}$$

This equation corresponds to the Born approximation for binary collisions (see section 2.1) and is accurate for dipole moments on the order of 1 $\mu_{\mathrm{B}}$ and far away from shape resonances [73].

It is remarkable that the parabolic density distribution is also a self-consistent solution of the GPE including $V_{\mathrm{dd}}^{\mathrm{mean}}$, if $\varepsilon_{\mathrm{dd}}$ does not exceed one. This is shown by integrating (3.25) with a density distribution of the form (3.11). It turns out that the physical dipolar contributions of $V_{\mathrm{dd}}^{\mathrm{mean}}$ are then also quadratic like the trapping potential $V_{\mathrm{ext}}(\boldsymbol{r}) = 1/2\, m \sum_i \omega_i^2 x_i^2$ and the mean field energy $gn(\boldsymbol{r})$ of the contact interaction [73]. Therefore, the GPE contains only parabolic and constant terms in the Thomas-Fermi limit and the inverted parabola profile is still an exact solution of the problem. However, it is not trivial to obtain the condensate radii with dipole-dipole interaction present. Here I will only discuss the results, see for example [73] for details on the derivation.

The in-trap radii $R_i$ for a magnetic field pointing in $z$ direction are obtained by solving the following equations

$$\omega_j^2 = \left(\frac{15N\hbar^2 a}{m^2 R_x R_y R_z}\right)\frac{1}{R_j^2}\left[1 - \varepsilon_{\mathrm{dd}} f(A_{xz}, A_{yz}) + \varepsilon_{\mathrm{dd}} A_{jz}\frac{\partial f(A_{xz}, A_{yz})}{\partial A_{jz}}\right],\ j = x, y\,, \tag{3.26}$$

$$\omega_z^2 = \left(\frac{15N\hbar^2 a}{m^2 R_x R_y R_z}\right)\frac{1}{R_z^2}\left[1 - \varepsilon_{\mathrm{dd}} f(A_{xz}, A_{yz}) - \varepsilon_{\mathrm{dd}} A_{xz}\frac{\partial f(A_{xz}, A_{yz})}{\partial A_{xz}} - \varepsilon_{\mathrm{dd}} A_{yz}\frac{\partial f(A_{xz}, A_{yz})}{\partial A_{yz}}\right]. \tag{3.27}$$

The function $f(A_{xz}, A_{yz})$ of the aspect ratios $A_{xz} = R_x/R_z$ and $A_{yz} = R_y/R_z$ depends on the incomplete elliptic integrals of the first and second kind and is discussed in appendix C.1. With the radii the mean-field potential can be calculated. I will not discuss the complete expression here (for details see [10]), but discuss only the simpler case of a spherical condensate with radius $R_{\mathrm{TF}}$. This example contains already the relevant main characteristics. Equation (3.25) integrated with a spherical density distribution is

$$V_{\mathrm{dd}}^{\mathrm{mean}}(\boldsymbol{r}) = \frac{\varepsilon_{\mathrm{dd}} m\omega_0^2}{5}\, r^2(1 - 3(\boldsymbol{e}_z \cdot \hat{\boldsymbol{r}})^2)\,, \quad r \le R_{\mathrm{TF}}\,. \tag{3.28}$$

The potential has a *saddle-shape* with a negative curvature when moving along the $z$ direction from the saddle point and a positive curvature when moving along $x$ or $y$ (see Fig. 3.5). This means that compared to a condensate with only contact interaction, the dipolar condensate is elongated in the dipole direction and compressed in the directions perpendicular to it. This is a bit counterintuitive, as from the simple two-body interaction of dipoles (Eq. (3.24))

[7] In the description by a partial wave decomposition this means that *all* partial waves contribute.

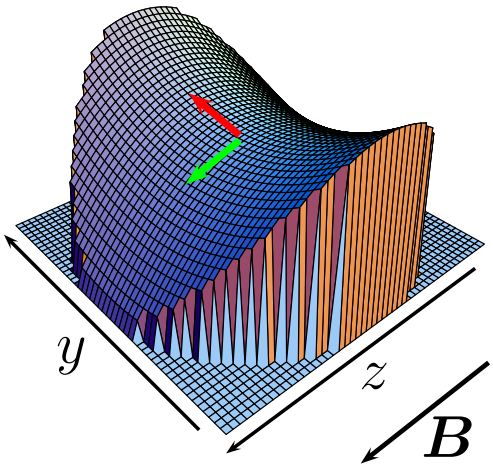


**Figure 3.5.:** *Saddle-shape mean field potential for a spherical dipolar condensate. The curvature is negative in z direction and positive in y direction. Therefore the condensate is elongated in the magnetic field direction compared to a condensate without dipole-dipole interaction.*

one could expect the opposite, because this interaction is attractive in the magnetic field direction. But the attractive interaction does not lead to a shrinking of the BEC, instead it results in a realignment of the dipoles. It is energetically favorable for the system to have more dipoles aligned in a way that they attract each other. In terms of aspect ratio this means that $A_{xz}$ and $A_{yz}$ are always smaller than without dipole-dipole interaction. This result is still valid for the free expansion, as will be shown in the next subsection.

### 3.3.2. Expansion Dynamics

The dynamics of a dipolar condensate is determined analogous to the pure contact case: With a hydrodynamic description the scaling factors of the radii are obtained through differential equations (see previous section). These equations are [74]

$$\begin{aligned}\frac{\mathrm{d}^2\lambda_j}{\mathrm{d}t^2} &= -\omega_j^2(t)\lambda_j + \frac{1}{\lambda_x\lambda_y\lambda_z}\frac{\bar{\omega}_j^2}{\lambda_j}\left[1-\varepsilon_{\mathrm{dd}}f\left(\frac{\lambda_x}{\lambda_z}A^0_{xz},\frac{\lambda_y}{\lambda_z}A^0_{yz}\right)\right.\\ &+ \left.\varepsilon_{\mathrm{dd}}\lambda_j\frac{\partial f}{\partial\lambda_j}\left(\frac{\lambda_x}{\lambda_z}A^0_{xz},\frac{\lambda_y}{\lambda_z}A^0_{yz}\right)\right], \quad j=x,y,z\,, \end{aligned} \tag{3.29}$$

where $A^0_{xz}=R^0_x/R^0_z$ and $A^0_{yz}=R^0_y/R^0_z$ are the initial in-trap aspect ratios and

$$\bar{\omega}_j^2 = \frac{15N\hbar^2 a}{m^2R^0_xR^0_yR^0_z}\frac{1}{(R^0_j)^2}\,. \tag{3.30}$$

The equations (3.29) have to be solved numerically.

Figure 3.6 shows how well the theory fits to experimental data. Shown is the evolution of the aspect ratio $A_{yz}$ with time of a $^{52}$Cr BEC for two different magnetic field directions [10]. If the field points along the long axis of the trap (red diamonds), the condensate is elongated in this direction compared to pure contact interaction (dashed line). If it is perpendicular (blue circles), the condensate is elongated in this perpendicular direction. In contrast to contact

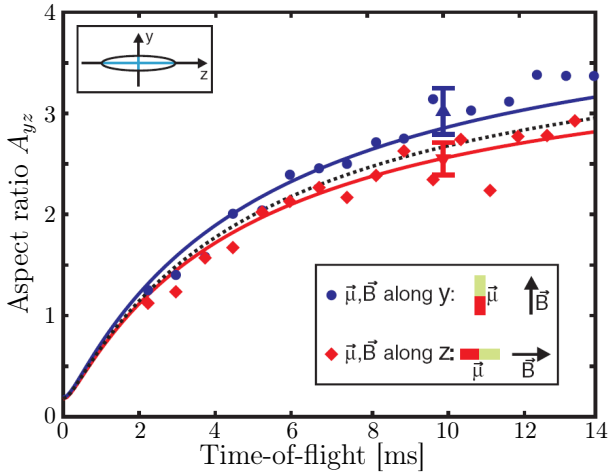


**Figure 3.6.:** *Evolution of the aspect ratio $A_{yz}$ after a sudden switch-off of the trap. The figure shows experimental data for $^{52}Cr$ with $\varepsilon_{\rm dd} = 0.16$. The theory curves are obtained by using the hydrodynamical theory described in this section. The expansion of the condensate was measured for two different magnetic field configurations. Red (diamonds): The magnetic field pointed along the long axis (z) of the trap (with trapping frequencies $(\omega_x, \omega_y, \omega_z) = 2\pi \times (942, 712, 128)$). The dipole-dipole interaction leads to an elongation of the condensate compared to pure contact interaction (dashed theory curve). Blue (circles): The magnetic field points along y and thus the aspect ratio decreases. Figure taken from [10].*

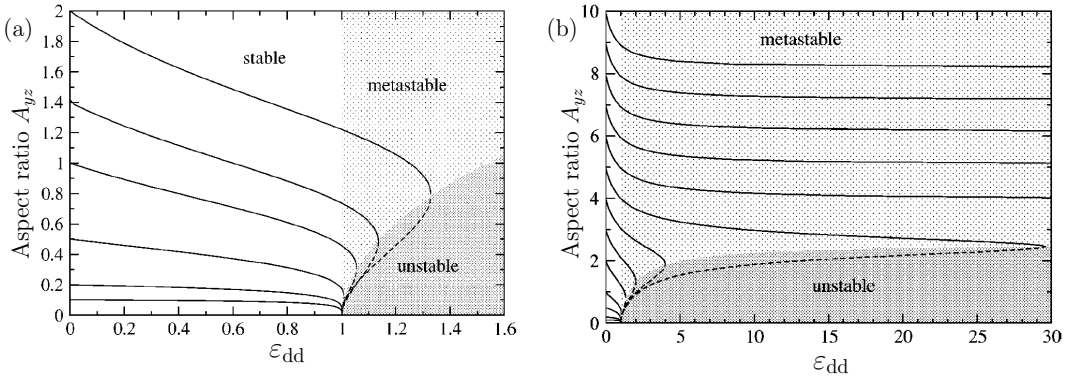


**Figure 3.7.:** *Stable and unstable regions for a dipolar condensates in a cylindrical symmetric trap. The aspect ratio $A_{yz} = A_{xz}$ of radial to axial Thomas-Fermi radii is plotted as a function of $\varepsilon_{\rm dd}$ for various ratios of the radial and axial trapping frequency $\gamma = \omega_z/\omega_y$. In (a) the region for small $\varepsilon_{\rm dd}$ of (b) is magnified. The value of $\gamma$ can be read at $\varepsilon_{\rm dd} = 0$ as this corresponds to pure contact interaction with $A_{yz} = \gamma$. The dashed lines indicate unstable branches. The metastable region corresponds to a local minimum of Eq. (3.26) and (3.27) (see text). Figure taken from [73].*

interaction, where the condensate expansion velocity depends on the gradient of the density, the dipole-dipole interaction does not lead to a faster expansion in the more compressed direction of the trap. The aspect ratio $A_{yz}$ stays always smaller than without dipole-dipole interaction (if the magnetic field points in $z$ direction).

Feshbach resonances allow to tune the scattering length $a$ and therefore to tune the relative strength of the dipole-dipole interaction to the contact interaction expressed by $\varepsilon_{\rm dd}$. Because $V_{\rm dd}$ is partially attractive, a dipolar condensate is unstable if $\varepsilon_{\rm dd}$ is larger than a critical

value $\varepsilon_{\mathrm{dd}}^{\mathrm{crit}}$. Already with the equations (3.26) and (3.27) important predictions can be made on the stability properties. This was done in [73] for a cylindrical symmetric trap with the magnetic field pointing in axial direction. Figure 3.7 shows stable and unstable regions for various trap geometries. In the Thomas-Fermi limit the trap geometry is the only parameter that determines if a condensate is stable for a given $\varepsilon_{\mathrm{dd}}$. It turns out that for $0 \leq \varepsilon_{\mathrm{dd}} < 1$ the solution of Eq. (3.26) and Eq. (3.27) corresponds to a global energy minimum and the condensate is stable for all geometries. For $\varepsilon_{\mathrm{dd}} \geq 1$ and a ratio of radial to axial trapping frequency $\gamma = \omega_z/\omega_x = \omega_z/\omega_y \leq 5.17$ two solutions exist: While one is unstable, the other one is only a local energy minimum and thus metastable. Above $\gamma = 5.17$ both solutions are metastable for all $\varepsilon_{\mathrm{dd}}$. For these extreme pancake-shaped (oblate) traps the repulsive part of $V_{\mathrm{dd}}$ leads to a stabilization. To summarize, cigar-shaped (prolate) traps with the dipoles aligned along the long axis are unstable for $\varepsilon_{\mathrm{dd}} \geq 1$, whereas for pancake traps larger $\varepsilon_{\mathrm{dd}}$ are possible.

# 4. Experimental Setup

*The experiment that is used to investigate strong dipolar effects in a Chromium BEC was set up mainly by J. Stuhler [75], P. O. Schmidt [76], S. Hensler [77], J. Werner [60] and A. Griesmaier [50]. Section 4.1 gives a coarse overview over the apparatus. For details the reader should consult the above mentioned references (see also [78] for an overview, or the diploma theses [79, 80, 81, 82]), which provide a great amount of detailed information on the setup. Section 4.2 reports on a method to measure the trapping frequencies of the optical dipole trap more precisely than with the parametric heating method which has been used before. The modifications to the setup, which are necessary to perform the experiments presented in this thesis, are described in the last two sections. Section 4.3 reports on the production of the stable, homogeneous magnetic field of 600 G to tune the scattering length. The calibration of the extra current, which runs in opposite direction in the pinch coils to compensate the curvature of the offset coils, is discussed in detail. In the last section 4.4, the high-field imaging system is described. This system allows to image the atoms at the high magnetic field close to the broadest Feshbach resonance.*

## 4.1. Bose-Einstein Condensation of Chromium

The production of a BEC of $^{52}$Cr atoms starting from 1600 ° C hot atoms which are sublimated from an oven, requires an elaborate series of trapping and cooling steps:

1. Decelerating of the hot atoms in a Zeeman Slower.
2. Trapping and cooling in a magneto-optical trap (MOT) and continuous loading of a magnetic trap (MT).
3. Doppler cooling and radio-frequency (RF) evaporation in the magnetic trap.
4. Loading into a crossed optical dipole trap (ODT) and optical pumping to the lowest Zeeman sub-state to avoid dipolar relaxation.
5. Forced evaporation in the ODT until quantum-degeneracy is reached.

This chapter will shortly describe the various parts of the experimental setup (see Fig. 4.1) following the steps sketched above.

### 4.1.1. Preparation of a Cold Sample in the Magnetic Trap

The Chromium atoms are sublimated from a high-purity sample of Chromium (99.99%) that is held within a specially designed crucible [60] in a high temperature effusion cell[1]. The oven

[1] VTS Schwarz GmbH, model HT-TA-35-10/W.

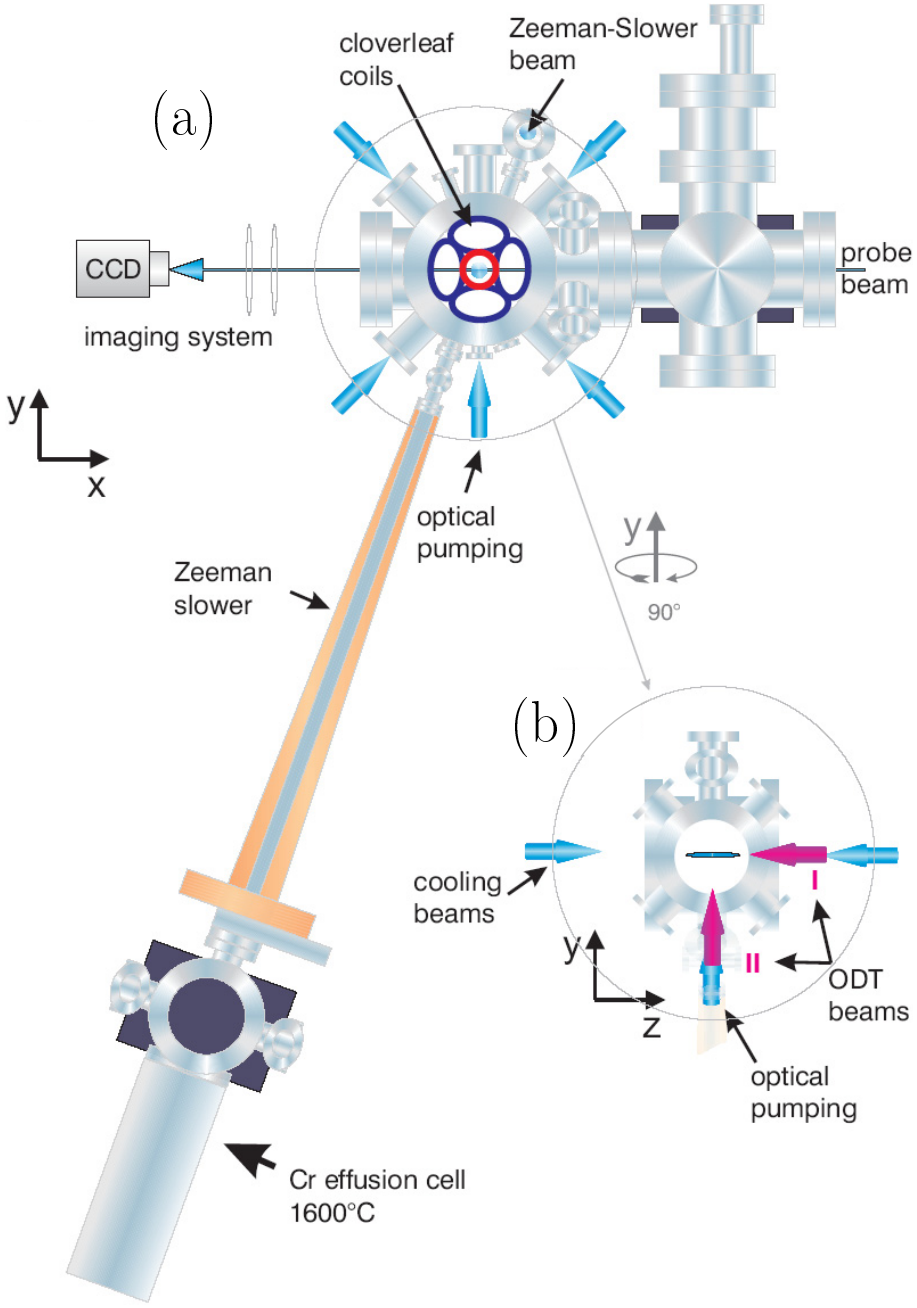


**Figure 4.1.:** *Scheme of the Chromium BEC experiment. (a) View of the complete vacuum chamber. Chromium is sublimated in a 1600° C hot oven. The atoms are then decelerated in a Zeeman slower before they are trapped and cooled in a MOT. The magnetic trap is continuously loaded via a metastable dark state. (b) 90° rotated view of the upper chamber. The two dipole trap beams are indicated. This crossed optical dipole trap is loaded from the magnetic trap after RF cooling. By ramping down the horizontal beam a BEC is produced through evaporative cooling. Figure taken from [50].*

is connected through an 80 cm long spin-flip Zeeman slower to the main chamber [81]. The Zeeman slower, which acts also as an differential pumping stage[2], decelerates atoms with an initial velocity smaller than $\sim 600$ m/s to the capture velocity of the MOT ($\sim 30$ m/s). The MOT is operated on the $^7S_3 \leftrightarrow {}^7P_4$ transition (see Figure 4.2 and appendix B.1 for details on the level structure of $^{52}$Cr).

The magnetic fields for the MOT are provided by the coils of the Ioffe-Pritchard type magnetic trap [81] (see also section 4.3). In MOT operation the cloverleaf coils create a radial gradient ($x$ and $y$ direction) of $\sim 10$ G/cm and the pinch coils an axial curvature ($z$ direction) of $\sim 15$ G/cm$^2$. The offset coils compensate the offset field of the pinch coils. Two orthogonal pairs of counter-propagating $\sigma^+/\sigma^-$-polarized laser beams confine and cool the atoms radially. In axial direction the magnetic field does not allow a MOT operation. Therefore the atoms are only Doppler-cooled in this direction using a $\sigma^+/\sigma^+$ optical molasses [76].

With a ratio of approximately 1/250000 the Chromium atoms do not decay back into the $^7S_3$ ground state, but into the metastable $^5D_4$ or $^5D_3$ states. These states have a magnetic dipole moment of 6 $\mu_B$ and 4 $\mu_B$, respectively. Atoms that are in a low-field seeking sub-state and are sufficiently cool are thus trapped in the weak confining potential of the magnetic field. As these atoms are decoupled from the light field without a repumping laser, this allows to continuously load the magnetic trap. After about 10 s a steady-state is reached, where the loading rate of the magnetic trap is equal to the losses due to light-induced collisions [76]. If the MOT beams are then switched-off and the atoms are pumped back into the ground state with the repumper[3] at 663 nm (shone in along the $z$ axis), a sample of approximately $10^8$ atoms is prepared in the MT close to the doppler temperature of 124 $\mu$K (phase space density $\sim 10^{-9}$) [50]. The atoms are pumped back via the $^7P_3$ state, as this allows faster pumping than via the $^7P_4$ state. Subsequently, the magnetic trap is compressed by ramping up the current in the cloverleaf, offset and pinch coils to 300 A. This leads to a heating of the cloud to $\sim 1$ mK. At this stage the gas is Doppler cooled with the axial $\sigma^+/\sigma^+$ beams. After the rethermalization of the sample the phase space density has increased by about 2 orders of magnitude without atom loss. The current is then ramped down adiabatically to form a magnetic trap with the highest possible overlap to the trapping potential of the horizontal dipole trap beam. In this magnetic trap RF cooling is performed. Due to the high magnetic moment of Chromium atoms it is important to have a low magnetic offset field at this stage, otherwise spin-changing collisions lead to too high atom losses at the densities that are reached during RF cooling [77]. With an additional current running through the offset coils, offset fields on the order of a few 10 mG are reached, which allow to cool down the sample to a temperature of approximately 22 $\mu$K without too high inelastic losses. About $5 \times 10^6$ atoms remain at a phase space density of $10^{-5}$. However, quantum-degeneracy cannot be reached in this way. Hence, the sample is pumped into the lowest Zeeman state $M_S = -3$, where spin-changing collisions cannot occur. This is done with a $\sigma^-$-polarized optical pumping laser at 427 nm, which pumps the atoms to the $M_S = -3$ state via the $^7P_3$ state (see Fig. 4.2 (b)). As the $M_S = -3$ state is high-field seeking, the MT has to be switched off before. The horizontal ODT beam, which is on during the whole first part of the experimental sequence, provides then the trapping potential. After ramping up also the vertical ODT beam in 5 s about $10^6$ atoms remain trapped [50].

[2] Allowing to have a 2 orders of magnitude lower pressure in the upper science chamber (about $10^{-11}$ mbar).

[3] The gain in atom number by repumping also the $^5D_3$ state atoms is small compared to using only the 663 nm repumper. Thus the $^5D_3$ atoms are not pumped back.

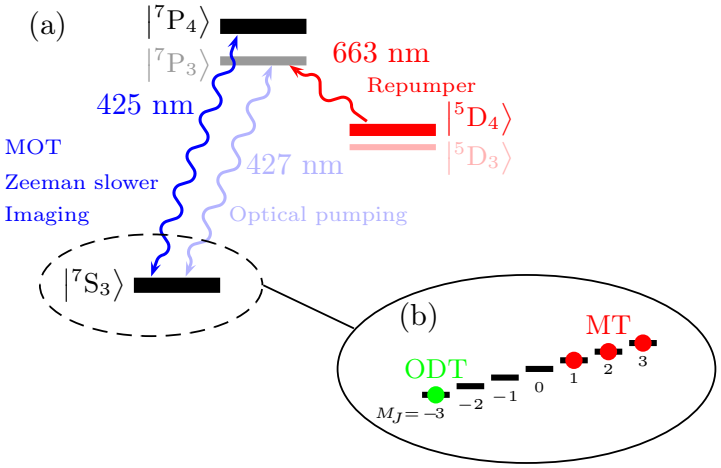


**Figure 4.2.:** *(a) Level scheme of $^{52}Cr$. The transitions that are used to cool the Chromium gas to quantum-degeneracy are indicated. The MOT and the Zeeman slower are operated on the $^7S_3 \leftrightarrow {}^7P_4$ transition. The atoms decay with a ratio of $\sim 1/250000$ to the metastable $^5D_4$ or $^5D_3$ levels. Without repumping lasers these are dark states and allow to continuously load the MT. After the MOT is switched off, the atoms in the MT are pumped back to the $^7S_3$ ground level with a repumper[3] at 663 nm. (b) Atoms in the low-field seeking substates $M_J = 1, 2, 3$ are trapped in the MT. To produce a BEC the atoms are transferred into an ODT and pumped into the lowest Zeeman level $M_J = -3$. The optical pumping is done via the $^7P_3$ level.*

### 4.1.2. Forced Evaporation in the Optical Dipole Trap

The ODT beams, which are crossed in the center of the MT, are produced by an Ytterbium fibre laser[4] at $\lambda_L = 1076$ nm. Although this laser has an output power of up to 100 W, it is typically operated with $\sim 40$ W. Higher powers lead to a deformation of the spatial laser mode. Whether this deformation is caused by the laser itself or by the optics, is not clear. However, it prevents the production of larger condensates and causes stability problems. The 40 W are split with a ratio of approximately 2 : 1 to produce the two trapping beams, whose intensities are controlled by acousto-optic modulators (AOMs)[5]. As a part of this thesis a two-frequency AOM driver was developed, which increases the pointing stability of the beams [13]. This driver is described in detail in appendix A. Behind the AOMs a maximal power of 16 W in the horizontal and 9 W in the vertical beam remains. The waist sizes $w_0$ at the focus position are 29 $\mu$m for the horizontal and 50 $\mu$m for the vertical beam [50]. Hence, typical trapping frequencies for the trap in which quantum degeneracy is reached (3 % of horizontal and 100 % of vertical power) are $(\omega_x, \omega_y, \omega_z) = 2\pi \times (650, 360, 550)$ Hz (see section 4.2).

In the crossed region (dimple) of the ODT, forced evaporative cooling is performed by ramping down the power of the horizontal beam in stepwise linear ramps. The hottest atoms fall out of the trap, leaving after rethermalization a colder sample. The speed of the ramps is optimized for maximal atom number in the condensate. Condensation occurs at about 4 % power in the horizontal beam. The BECs have a typical size of 40000 atoms. Figure 4.3 summarizes the route to a BEC in more detail in a phase space density $\rho$ vs. atom number

[4] IPG, VLR-100-L.
[5] Crystal Technology, 3110-125 and 3110-199.

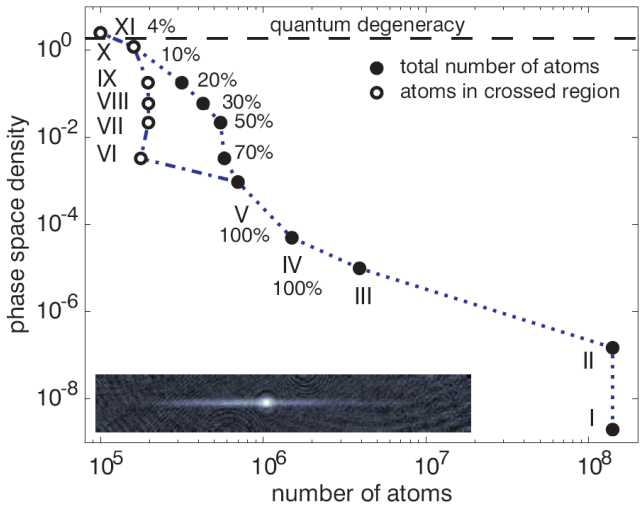


**Figure 4.3.:** *Evolution of the phase space density $\rho$ vs. atom number during the preparation process. Steps I–III correspond to MT, Doppler cooling and RF cooling. At step IV the MT is switched of and the atoms are held only with the horizontal trapping beam. Between IV and V the second ODT beam is ramped up to 100 %, plain evaporation leads to atom losses and increases $\rho$. From step V on both the atom number in the crossed region (open circles) and the total atom number in the ODT (closed circles) is shown. The horizontal beam is ramped down in stepwise linear ramps from 100 % to a value $< 4$ % to reach quantum-degeneracy. This is done in about 10 s. Figure taken from [50].*

plot. The total experimental sequence to create a BEC of Chromium atoms takes about 40 s. At the end of the sequence a picture is taken of the cloud after a short time of free expansion (a few ms) by absorption imaging. A $\sigma^-$-polarized beam resonant on the MOT transition is shone in along the $x$ axis. The beam is detected with a CCD camera, which allows to measure the density profile integrated over the $x$ direction (see also section 4.4).

## 4.2. Measurement of the Trapping Frequencies

For any theoretical prediction of the condensate dynamics, it is important to know the trapping frequencies of the optical dipole trap precisely. In principle the frequencies can be calculated, if waist size and power of the two beams at the position of the trap are known. The depth of the trapping potential is then obtained with the following formula [77]

$$V_{\mathrm{dip}}(I(\boldsymbol{r})) = -0.273 \times 10^{-36}\,\mathrm{J}\,\frac{\mathrm{m}^2}{\mathrm{W}} \times I(\boldsymbol{r})\,, \tag{4.1}$$

where $I(\boldsymbol{r})$ is the laser intensity. For a Gaussian beam a harmonic approximation around the focus position gives the trapping frequencies

$$\omega_r = \sqrt{\frac{4V_0}{mw_0^2}}\,, \quad \omega_z = \sqrt{\frac{2V_0}{mz_r^2}} \tag{4.2}$$

in radial and axial direction, where

$$V_0 = |V_{\mathrm{dip}}(I_0)|\,, \quad I_0 = \frac{2P}{\pi w_0^2}\,, \tag{4.3}$$

with the laser power $P$ and the Rayleigh range

$$z_r = \pi w_0^2/\lambda_{\mathrm{L}}\,. \tag{4.4}$$

As the square of the frequencies is proportional to the trapping potential, a quadratic summation of the frequencies of horizontal ($\omega_r^{\mathrm{h}}$, $\omega_z^{\mathrm{h}}$) and vertical ($\omega_r^{\mathrm{v}}$, $\omega_z^{\mathrm{v}}$) beam give the total trapping frequencies in $x$, $y$ and $z$:

$$\omega_x = \sqrt{(\omega_r^{\mathrm{h}})^2 + (\omega_r^{\mathrm{v}})^2}\,, \tag{4.5}$$
$$\omega_y = \sqrt{(\omega_r^{\mathrm{h}})^2 + (\omega_z^{\mathrm{v}})^2}\,, \tag{4.6}$$
$$\omega_z = \sqrt{(\omega_z^{\mathrm{h}})^2 + (\omega_r^{\mathrm{v}})^2}\,. \tag{4.7}$$

However, the real trapping frequencies depend strongly on the exact waist sizes and the relative position of the two beams at the crossing point. If the beams are for example astigmatic or elliptic, or slightly misaligned, the theoretical values are only a good estimate and have to be measured to obtain accurate values. There are two methods at hand to measure the frequencies: Heating by parametric resonances and a direct measurement by exciting a center-of-mass motion of the cloud in the trap. A parametric resonance occurs when the trapping potential is modulated at

$$\omega_{\mathrm{mod}} = \frac{2\omega_{\mathrm{trap}}}{n}\,, \quad n \in \mathbb{N} \tag{4.8}$$

with a small sinusoidal perturbation. The theory of parametric resonances is well known from classical mechanics (see for example [83]) and is described by the following differential equation in one dimension:

$$\ddot{x}(t) + \omega_{\mathrm{trap}}^2 \left(1 + \varepsilon \sin\left(\omega_{\mathrm{mod}} t\right)\right) x(t) = 0\,. \tag{4.9}$$

It can be shown that the strongest resonance occurs at $\omega_{\mathrm{mod}} = 2\omega_{\mathrm{trap}}$.

In our setup the method is realized by modulating one of the two trapping beams with $\varepsilon$ on the order of 5 %. A modulation at a resonance frequency leads to heating and atom losses. If the horizontal (respectively vertical) beam is modulated, resonances occur only if Eq. 4.8 is fulfilled for $\omega_x$ or $\omega_y$ (respectively $\omega_z$), as the axial contributions to the trapping frequencies are negligible (see Eq. (4.5)–(4.7)). Figure 4.4 shows a spectrum measured by modulating the horizontal beam. The spectrum was recorded for a trap with 8 % of the maximal power in the horizontal (approximately 1.3 W) and 100 % power in the vertical beam (approximately 9.3 W). It is evident that the assignment of the resonances is not trivial and needs a good initial guess for the frequencies. Especially in this case, were two frequencies coincide and cannot be resolved.

The direct measurement does not have this drawback. The frequencies are measured directly by applying a magnetic field gradient to the cloud in the trap. This results in a

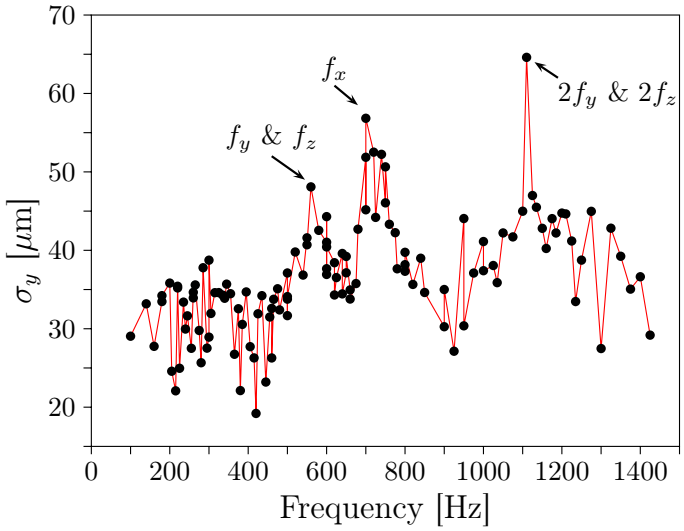


**Figure 4.4.:** *Parametric heating spectrum for the horizontal beam. Shown is the cloud size in y direction after 3 ms time-of-flight. The modulating time is 400 ms and $\varepsilon \approx 0.05$. Five resonances occur, of which the ones corresponding to $f_y$ and $f_z$ cannot be separated.*

| Trap | $f_y$ [Hz] | $f_z$ [Hz] |
|---|---|---|
| 7/42 | $(543 \pm 16)$ | $(371 \pm 8)$ |
| 3/100 | $(357 \pm 6)$ | $(566 \pm 30)$ |
| 8/100 | $(575 \pm 10)$ | $(599 \pm 18)$ |

**Table 4.1.:** *Trapping frequencies measured with the direct method for traps used in the experiments on strong dipolar effects. The notation a/b stands for percent of total power in the horizontal/vertical beam.*

constant force on the atoms which shifts the zero position of the trap. If the gradient is then switched off abruptly, the cloud oscillates in the trap. The oscillation frequency is obtained by measuring the cloud position after a short time-of-flight by varying the holding time in the trap. Figure 4.5 shows the $y$ position for a variable holding time for a trap with 3 % power in the horizontal and 100 % in the vertical beam. For these measurements a single pinch coil[6] was used to produce a gradient on the order of 10 G/cm. The gradient is ramped up in 100 ms to adiabatically shift the center-of-mass position. Directly after this it is switched off and the cloud is held in the trap for a variable time up to 5 ms. This procedure results in a 20 $\mu$m large oscillation amplitude of the $y$ position after 10 ms of time-of-flight. Table 4.1 summarizes the trapping frequencies obtained with this method for three different traps, which are used in the experiments on strong dipolar effects. The frequency in $x$ direction cannot be measured, because the cloud is imaged in the $yz$-plane. But $f_x = (f_y^2 + f_z^2)^{1/2}$ is already a very good estimate, as the unknown axial contributions to $f_y$ and $f_z$ are negligible.

[6] At the end of this thesis new electronics were set up, which allow now to produce a ten times larger gradient by using both pinch coils with conversely running current (see section 4.3).

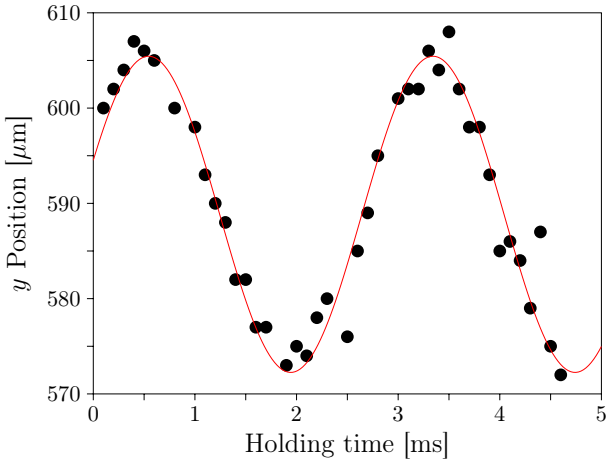


**Figure 4.5.:** *Direct measurement of the trapping frequencies. The cloud position after 10 ms of time-of-flight is measured for a variable holding time after exciting a center-of-mass motion of the cloud. Shown here is the y position of the cloud. A sinusoidal fit (red line) to the data gives* $f_y = (357 \pm 6)$ *Hz.*

## 4.3. Producing a Homogeneous Magnetic Field of 600 Gauss

The stability of the magnetic field $B$ to tune the scattering length $a$ with a Feshbach resonance has to be much better than the width of the resonance $\Delta B$. Therefore, in the experiments described in this thesis the broadest resonance at 589.1 G is used, as it allows to fulfill this condition most easily. However, for magnetic fields on this order of magnitude even small inhomogeneities lead to forces on the atoms which can significantly disturb the forced evaporative cooling in the ODT and even prevent the formation of a BEC[7]. Nevertheless, the evaporative cooling has to be done in the presence of $B$, as the Feshbach resonance cannot be crossed without destroying the quantum-degeneracy at the densities reached in a BEC (typically on the order of $10^{14}$ cm$^{-3}$). Due to the geometric constraints of the vacuum chamber, the currents to provide a magnetic field of $\sim 600$ G at the position of the atoms are on the order of 400 A. The water-cooled coils of the magnetic trap are thus a natural choice to create the $B$ field. This section describes the steps that are necessary to produce a stable and homogeneous enough magnetic field with these MT coils.

### 4.3.1. Curvature Compensation

The coils are sketched in Fig. 4.6. They consist of two pairs of: pinch, offset and 4 cloverleaf coils (for technical details on the coils see [81]). In MT operation the current runs conversely in pinch and offset coils. The pinch coils create an axial curvature with an offset field, which is compensated by the current in the offset coils. The cloverleaf coils provide the gradient for radial confinement. Only the offset coils create a relatively homogenous field, as they are almost in Helmholtz configuration (distance approximately 75 mm and radius approximately 60 mm).

[7] Also the field should vary much less than $\Delta B$ over the cloud, because otherwise the scattering length depends on the position in the cloud.

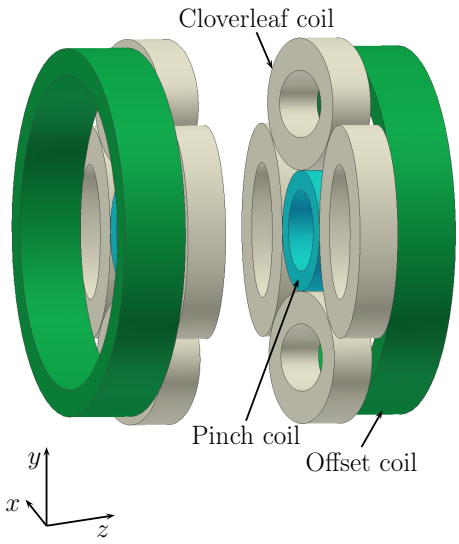


**Figure 4.6.:** *Coils of the magnetic trap. The pair of pinch coils create an axial curvature with an offset field. This field is compensated by the offset coils. The two pairs of 4 cloverleaf coils create the gradient for radial confinement.*

First tests showed quickly that the field of the offset coils is still not homogenous enough: In the presence of their magnetic field it is not possible to cool down to quantum degeneracy. The absolute value of the field at the center of the coaxial coils — where the atoms are held in the ODT — has a saddle-shape with an axial curvature $b''$ that has opposite sign and is twice as large as the radial curvature:

$$B = B_0 + \frac{1}{2}b''\left(z^2 - \frac{1}{2}r^2\right) . \tag{4.10}$$

Expressed in terms of trapping frequencies[8]

$$f_j = \frac{1}{2\pi}\sqrt{\frac{-6\mu_\mathrm{B}}{m}\frac{\partial^2 B}{\partial j^2}}\,, \quad j = r, z \tag{4.11}$$

for atoms in the $M_J = -3$ state, this condition reads as

$$f_z^2 = -2f_r^2 . \tag{4.12}$$

The derivation of Eq. (4.10)–(4.12) is given in appendix C.2. Figure 4.7 (a) shows a theoretical calculation of the field of the offset coils in axial direction for a current of 385 A. The calculation shows that the axial curvature is positive. Hence, the atoms are repelled in axial direction and trapped radially. This radial trapping prevents efficient evaporative cooling, as some of the atoms that fall out of the ODT stay trapped.

As the pinch coils create an approximately 25 times larger curvature than the offset coils (for the same offset field), they can compensate the curvature created by the offset coils with

[8]To simplify the theoretical description, the concept of imaginary trapping frequencies is used. Imaginary frequencies result in an repulsive force on the atoms (anti-trapping).

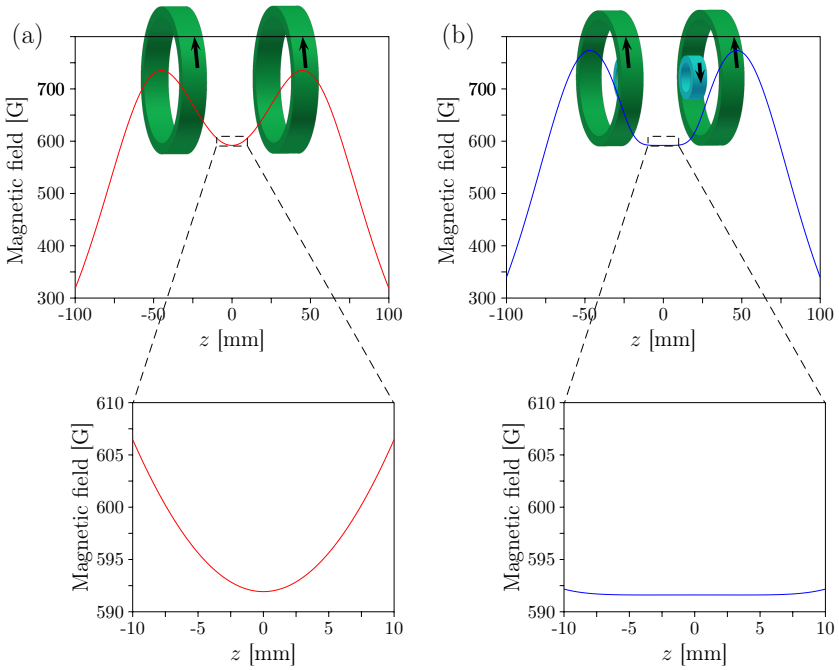


**Figure 4.7.:** *Compensation of the curvature of the offset coils. (a) Without the extra current in the pinch coils the magnetic field has a saddle shape with a positive curvature in axial direction. (b) With a small current (about 16 A in the experiment) running in opposite direction in the pinch coils, the curvature is compensated. The ratio in this theoretical calculation is approximately* $I_{\mathrm{pinch}}/I_{\mathrm{offset}} = 0.06$*, which is in reasonable agreement with the experimental determined value of* 0.04 *(see subsection 4.3.3) taking into account that the exact distances, diameters and relative alignment of the coils are known only to about 5 %.*

a small current running in opposite direction (see Fig. 4.7 (b)). Let us discuss this in more detail. The magnetic field close to the center of two coaxial coils has the following form (see appendix C.2):

$$\boldsymbol{B}(r,z) = -\frac{1}{2}b''zr\,\boldsymbol{e}_r + \left[B_0 + \frac{1}{2}b''\left(z^2 - \frac{1}{2}r^2\right)\right]\boldsymbol{e}_z\,. \tag{4.13}$$

Adding the pinch and offset field with $b''_{\mathrm{offs}} = b''_{\mathrm{pinch}} = b''$ results in

$$\boldsymbol{B}(r,z) = (B_0^{\mathrm{offs}} - B_0^{\mathrm{pinch}})\,\boldsymbol{e}_z - b''zr\,\boldsymbol{e}_r\,. \tag{4.14}$$

Up to second order in $r$ and $z$ the absolute value is therefore constant

$$B = (B_0^{\mathrm{offs}} - B_0^{\mathrm{pinch}})\,. \tag{4.15}$$

If $b''_{\mathrm{pinch}} < b''_{\mathrm{offs}}$, a radial trapping and axial repulsive curvature remains. If $b''_{\mathrm{pinch}} > b''_{\mathrm{offs}}$, the curvature is *over-compensated*, leading to an axially trapping and radially repulsive potential. The complete compensation is possible of course only under perfect conditions. If the centers of the two coil pairs do not coincide, or if any of the coils is tilted or not coaxial, the curvature cannot be compensated completely. In addition to the remaining curvature a gradient occurs, as is shown in subsection 4.3.3.

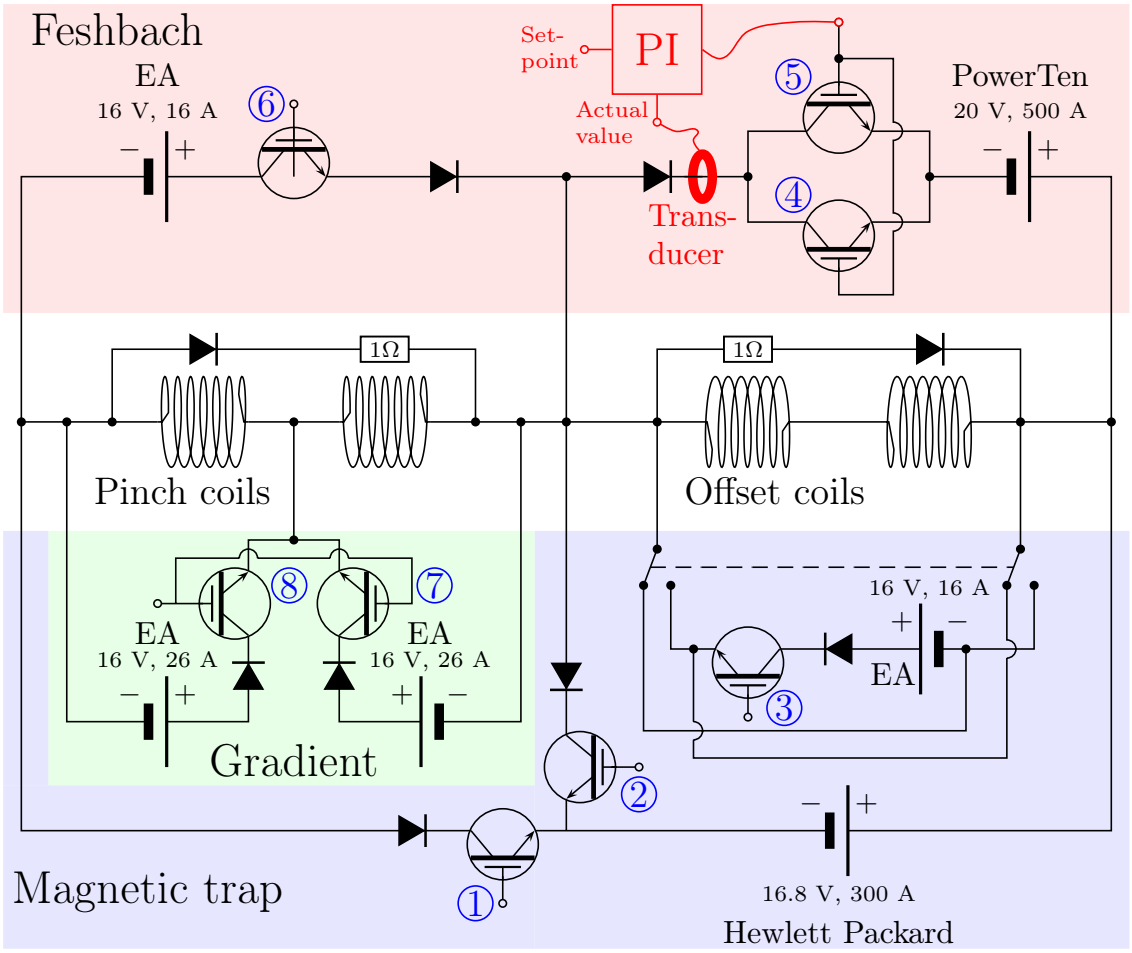


**Figure 4.8.:** *Scheme of the electronics to provide the current for pinch and offset coils. The electronics is divided in three parts. The MT part (blue) is used for the MOT and MT. The Feshbach part (red) was set up to be able to create a stable, homogeneous magnetic field at 600 G. The gradient part (green) is used to measure trapping frequencies. The usage of the numbered IGBTs is explained in the text. Sketched in red is the closed-loop control of the current for the high magnetic field. For a clear illustration some varistors and diodes are not shown in the scheme. They are used to protect the power supplies and IGBTs against high induction voltages.*

### 4.3.2. Technical Realization

To provide the large current in the offset coils and the small conversely running current in the pinch coils, the experimental setup is modified. Figure 4.8 shows a scheme of the modified electronics to control the currents. The electronics is divided in three groups: The magnetic trap (blue), Feshbach (red) and gradient (green) part. The diodes that are in series with the insulated gate bipolar transistors (IGBTs) separate the different circuits. The MT electronics is used in the first part of the experimental sequence. The IGBT ①switches the current of the Hewlett Packard power supply[9] which runs through the offset coils and in opposite direction through the pinch coils. IGBT ② allows to by-pass the pinch coils, but is not used at the moment. As stated in section 4.1, during RF cooling the magnetic offset field has to be as

[9]Hewlett Packard, 6682A.

low as possible. Hence, an additional current running in the offset coils is used to compensate the remaining offset field. This current is switched with IGBT ③ and can be send in either direction through the offset coils by the use of two switches (connected with the dashed line in Fig. 4.8). Parallel to offset and pinch coils are ring-down circuits consisting of a small resistor and a diode to protect the system against high induction voltages caused by fast switching of the magnetic fields.

The Feshbach part is used to produce the homogenous 600 G field. IGBT ④ and ⑤ control the current of the PowerTen power supply[10]. The current is actively stabilized with a closed-loop control. The set-point is given by a voltage (0 to −10 V), which is produced by a 12 bit digital-to-analog board. This results in a resolution of about 80 mG for a control range of 100 A. The actual value is measured with a high precision current transducer[11] with an output noise (rms) and a linearity on the order of $10^{-6}$. An additional TTL signal is used to switch on the current initially with the proportional-integral controller (PI). With this setup a peak-to-peak magnetic field stability of $10^{-4}$ ($3 \times 10^5$ rms) is reached. The magnetic field is switched on to 600 G in about 5 ms. This corresponds to a speed of approximately 50 G/ms at the position of the 589.1 G resonance. This speed is necessary to minimize inelastic losses when crossing the resonance. IGBT ⑥ switches the pinch current of the curvature compensation. It is controlled by a push-pull circuit with a TTL signal to be able to switch on fast.

The gradient part was set up at the end of this thesis. The IGBTs ⑦ and ⑧ switch up to 26 A each, which run conversely through the two pinch coils. This produces a gradient of up to 100 G/cm. The gradient can be used to measure trapping frequencies (see section 4.2) and was used in the experimental efforts to detect $Cr_2$ molecules (see outlook).

### 4.3.3. Calibration of the Curvature Compensation

In order to calibrate the ratio $I_{\text{pinch}}/I_{\text{offset}}$ for the best curvature compensation, a series of measurements of the remaining curvature is done in a single optical dipole trap beam. The single beam confines the atoms in two dimensions, which allows us to measure oscillations on a few seconds timescale in the third dimension. The remaining curvature is extracted from the oscillation period. Depending on the current in the pinch coils the potential produced by the magnetic field is either trapping in radial or in axial direction: At small currents $I_{\text{pinch}}$ the curvature of the offset coils is larger and the atoms are trapped radially and repelled axially. It is the inverse, if the offset curvature is over-compensated. Hence, for small currents the single vertical beam and for larger currents the single horizontal beam is used to measure the oscillations in the inhomogeneous magnetic field.

The measurements are done with a sample of approximately 30000 atoms at a temperature and density close to quantum-degeneracy. The preparation of the sample is sketched in Fig. 4.9. The figure shows the experimental sequence after the vertical ODT beam has been ramped to full power. The power of the horizontal beam is then ramped down to 2.5 % of its initial value in approximately 8 s. At the time it reaches 30 %, the current in offset and pinch coils is switched on. This switch-on point is chosen because atom losses are minimal at this time: If the current is switched on earlier, some atoms are still in the wings of the horizontal trapping beam and not in the strongly confined crossed region. These atoms are lost from

[10] PowerTen, R63D-20500.
[11] Danfysik, ULTRASTAB 860R.

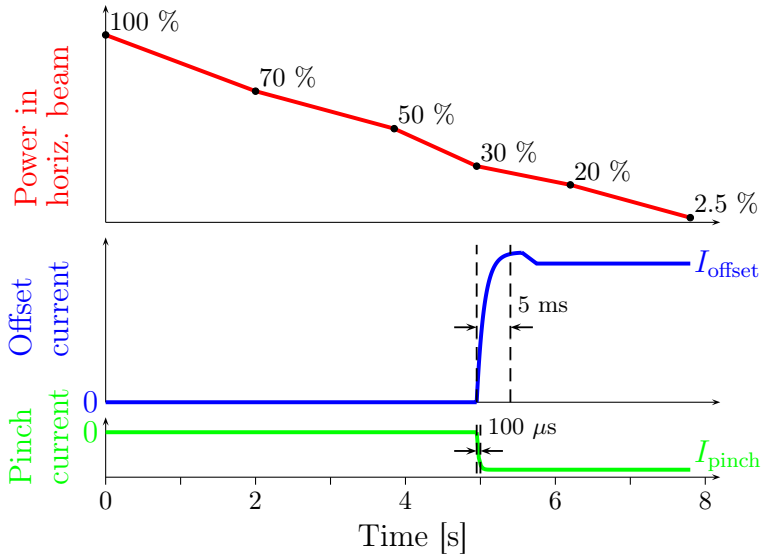


**Figure 4.9.:** *Preparation sequence of the cold atomic sample. Sketched is the power in the horizontal ODT beam and the current in the offset and pinch coils during the sequence. The power in the horizontal beam is ramped down in stepwise linear ramps to 2.5 % of its initial value. The current in the offset and pinch coils is switched on when the power reaches 30 %. In order to cross all Feshbach resonances as fast as possible, the current in the offset coils is switched on to* $\sim 450$ *A (*$\sim 700$ *G). This takes about 5 ms. After this the current is ramped down to* $I_{\text{offset}} = 390$ *A (*$\sim 615$ *G) close to the broadest resonance at* 589.1 *G. The current in the pinch coils is switched on to a constant value* $I_{\text{pinch}}$*. Due to the lower inductance of these coils this takes only* $\sim 100$ $\mu s$*.*

the trap due to the inhomogeneity of the magnetic field, which cannot be avoided during the $\sim 5$ ms it takes until the field reaches its maximum value. If the current is switched on at a later stage when the density of the cloud is already much higher, the crossing of the Feshbach resonances leads to inelastic atom losses.

After the 2.5 % power in the horizontal beam are reached, either the vertical or the horizontal beam is switched off, depending if the curvature is over-compensated or not. To provide a sufficient stabilization against gravity for measurements in the single horizontal beam, its power is ramped back up to 30 % in 100 ms before the vertical beam is switched off. Subsequently, the cloud position is determined after a variable holding time in the single beams. Figure 4.10 (a) shows absorption images of oscillations in the horizontal beam for $I_{\text{pinch}} = 20$ A. The cloud oscillates around a zero position that is shifted by approximately 2 mm from the center of the coils due to a magnetic field gradient. This gradient is a first indication that pinch and offset coils are not aligned in a cylindrically symmetric way. It is on the order of 1 G/cm (see subsection 4.3.4). The shape oscillations of the cloud at twice the frequency of the center of mass motion correspond to the monopole mode[12].

In Fig. 4.10 (b) the variation of the $z$ position with time is shown. A fit allows to determine the oscillation frequency precisely. This is done for three values of $I_{\text{pinch}}$ with radial trapping and two with axial trapping (see table 4.2). The measured values have to be corrected for the weak axial trapping potentials of the single dipole trap beams. In the vertical beam the

[12]When releasing the atoms from the tight ODT potential into the weak potential of the magnetic field, first the cloud expands. Due to the harmonicity of the potential, all particles oscillate with the same frequency and thus the initial cloud shape is recovered twice in an oscillation period of the center-of-mass motion.

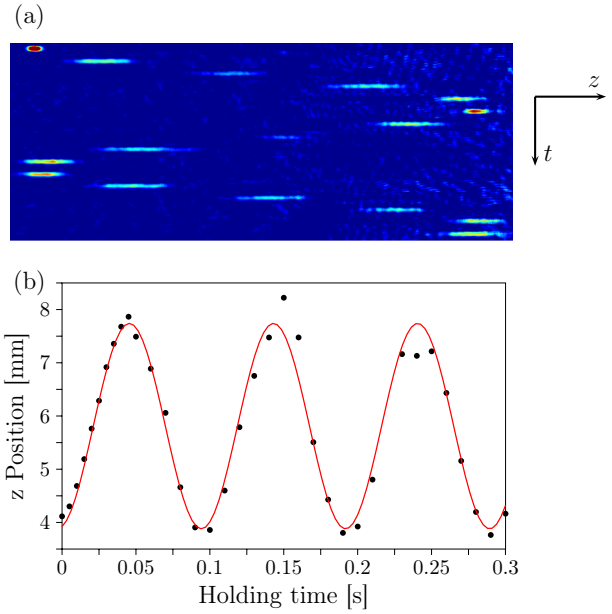


**Figure 4.10.:** *(a) Absorption images of the oscillations of the atomic cloud in the horizontal ODT beam. The time between two subsequent pictures is 100 ms. The field of view for each picture is* $0.1 \times 4.1$ *mm (b) z position of the cloud corresponding to the oscillation shown above. The fit frequency (red line) is* $10.3 \pm 0.1$ *Hz.*

| Pinch current [A] | Direction | Measured [Hz] | Corrected [Hz] |
|---|---|---|---|
| 0 | radial | $(11.6 \pm 0.1)$ | $11.3 \pm 0.3$ |
| 5 | radial | $(9.2 \pm 0.1)$ | $8.8 \pm 0.3$ |
| 10 | radial | $(6.1 \pm 0.1)$ | $5.6 \pm 0.2$ |
| 20 | axial | $(10.3 \pm 0.1)$ | $7.5 \pm 3.9$ |
| 23 | axial | $(13.2 \pm 0.1)$ | $11.2 \pm 2.6$ |

**Table 4.2.:** *Measured and corrected oscillation frequencies for various pinch currents.*

cloud oscillates in a range smaller than the Rayleigh length $z_r$ (Eq. (4.4)) and the harmonic approximation (Eq. (4.2)) is a good estimate. It gives $\omega_y = 2\pi \times 2.5$ Hz. As the waist of the horizontal beam is smaller, the cloud in the horizontal beam moves in a range larger than $z_r$ of this beam. Therefore the influence of the beam can only be estimated. A numerical simulation showed it should be approximately $\omega_z \approx 2\pi \times 7$ Hz. Whereas the uncertainty of $\omega_y$ is smaller than 10 %, because waist and power of the vertical beam are known quite precisely, the uncertainty of $\omega_z$ is estimated to be on the order of 30 % due to mainly two reasons: The influence of the anharmonicity is not exactly known, as well as the exact focus position. The corrected values of the measured frequencies are also listed in table 4.2.

Subsection 4.3.1 showed that for perfect coaxial alignment of pinch and offset coils, the axial curvature would have opposite sign and be twice as large as the radial curvature. This is valid for small currents $I_{\text{pinch}}$ leading to radial trapping, as well as for large $I_{\text{pinch}}$, which over-compensate the curvature. Hence, to obtain the current corresponding to the best

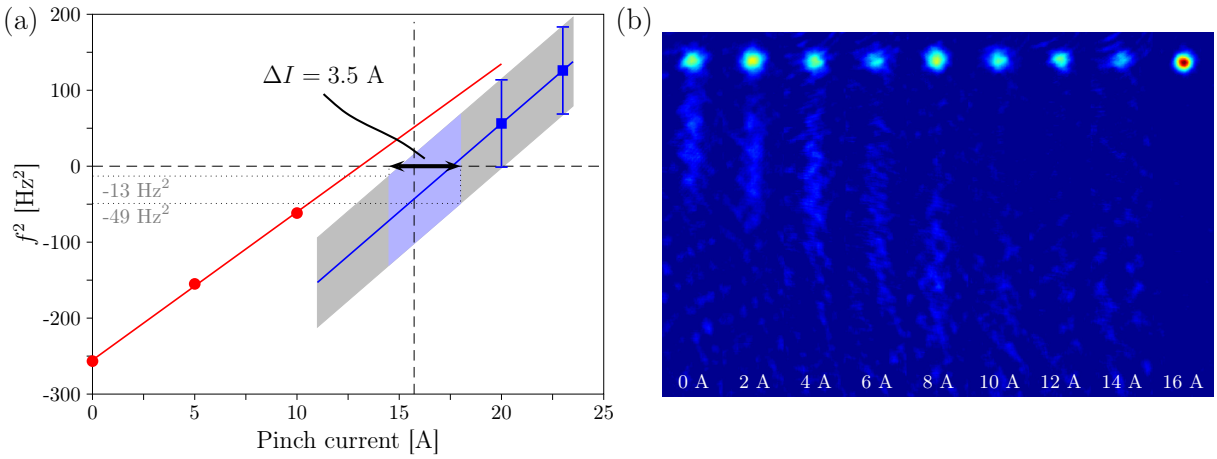


**Figure 4.11.:** *(a) Determination of the optimal curvature compensation. Plotted is $-2f_r^2$ (red circles) and $f_z^2$ (blue squares) for the corrected radial and axial trapping frequencies as a function of compensation current $I_{\mathrm{pinch}}$. The lines correspond to an extrapolation to higher (lower) currents in the pinch coil. The gray-shaded area indicates the systematic uncertainty of $f_z^2$ due to the error arising from the uncertainty of the effect of the horizontal trapping beam. With the condition $f_r^2 = f_z^2$ the current range of $\Delta I = 3.5$ A is obtained (see text). The blue-shaded area indicates the uncertainty of $f_z^2$ in this range. The vertical dashed line corresponds to the value $I_{\mathrm{pinch}} = 15.6$ A, which is used in the experiments on strong dipolar effects. (b) Absorption images for various compensation currents. The field of view is $2.9 \times 0.3$ mm for each picture. The pictures show that for higher pinch currents the radial confinement decreases: the hot atoms that are trapped below the ODT move away. Above 16 A condensation is possible, as the hot atoms do not prevent the condensation anymore.*

curvature compensation, $-2f_r^2$ and $f_z^2$ are plotted vs. $I_{\mathrm{pinch}}$ in Fig. 4.11 (a). For a perfect alignment of the coils the 5 data points would fall on a straight line and the zero crossing of this line would correspond to complete compensation. It is obvious that this is not the case. Even including the systematic error due to the 30 % uncertainty of the effect of the horizontal trapping beam (gray-shaded area) the deviation is significant. Thus, the coils are not aligned symmetrically. Nevertheless, the current $I_{\mathrm{pinch}}$ of optimal compensation can be determined. As shown in the Fig. 4.11 (a) this current lies in the range 14.5 to 18 A for an offset current of 390 A. To determine these values, the simple condition $f_r^2 = f_z^2$ is applied to the linear extrapolation function of the values measured radially (red line) and the extrapolation function corresponding to the upper (respectively lower) error-bars. At $I_{\mathrm{pinch}} = 14.5$ A the condition is $f_r^2 = f_z^2 = -13$ Hz$^2$ and at $I_{\mathrm{pinch}} = 18$ A it is $f_r^2 = f_z^2 = -49$ Hz$^2$ (dotted lines). Thus, within this current range the potential of the magnetic field is repulsive radially ($f_r$ imaginary), with $3.5 \geq |f_r| \geq 7$ Hz. It is either repulsive or trapping axially with $f_z$ lying in the blue-shaded area. The current used in the experiments on strong dipolar effects is $I_{\mathrm{pinch}} = 15.6$ A. At this current, the axial frequency $f_z$ is smaller than 10 Hz and the radial $|f_r|$ is smaller than 5 Hz.

Figure 4.11 (b) shows how the curvature compensation effects the evaporative cooling process. For small values of $I_{\mathrm{pinch}}$ hot atoms are trapped below the ODT and quantum-degeneracy is not reached. At 16 A this changes, as the hot atoms are so weakly confined (or repelled, respectively), that an effective evaporation is not prevented. This does not change for higher currents, as the potential stays repulsive in radial direction. However, the curvature has of course also an effect on the expansion of the BEC. Thus, the curvature has

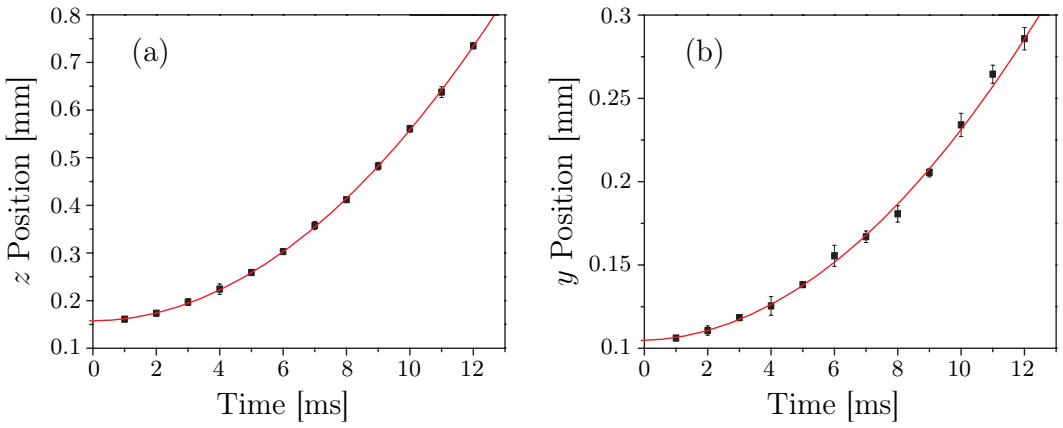


**Figure 4.12.:** *Determination of the magnetic field gradient. Shown in the figure is the movement of the atomic cloud in z direction (a) and y direction (b), respectively, after releasing it from the ODT. Due to the constant force caused by the gradient, the trajectory is parabolic. With a polynomial fit (red lines) up to second order the resulting gradient of the magnetic field in both directions is obtained.*

to be compensated as good as possible.

### 4.3.4. Magnetic Field Gradient

As could already be seen by the shift of the zero position of the oscillations in the horizontal beam, the misalignment of pinch and offset coils results also in a magnetic field gradient. This gradient can be determined if both beams are switched off and the atoms expand freely. The motion of the cold cloud at timescales much smaller than the oscillation period (caused by the remaining curvature) is determined by gravity and the magnetic field gradient. Figure 4.12 shows the time dependence of $y$ and $z$ position after releasing the atoms from the ODT. A constant force gives rise to a quadratic increase of the cloud position with time, therefore the axial and radial gradient of approximately 1.2 G/cm (exact within 5 %) is obtained by fitting the movement with a polynomial up to second order. In radial direction the acceleration due to gravity has to be subtracted to determine the magnetic field gradient. Both gradients are on the order of gravity (for Chromium $mg/\mu \approx 1.5$ G/cm). They have no effect on the atoms besides a small shift of the trap position and a constant acceleration of the atoms during the TOF. They do *not* change the expansion dynamics of the cloud.

## 4.4. High-Field Imaging System

The broadest Feshbach resonance of $^{52}$Cr occurs at a magnetic field of 589.1 G [12]. To provide such a high magnetic field (for brevity called high-field (HF)) at the position of the atoms, the coils of the magnetic trap are used, as explained in the previous section. The imaging of the BEC has to be done at HF, since too many atoms are lost if the magnetic field is switched off first. The reason for this is that all 14 resonances are crossed during the switch-off process. Hence, $Cr_2$ molecules are produced coherently due to the ramp over the resonances and via three-body collisions (see section 2.2 and 2.3). The molecules are not

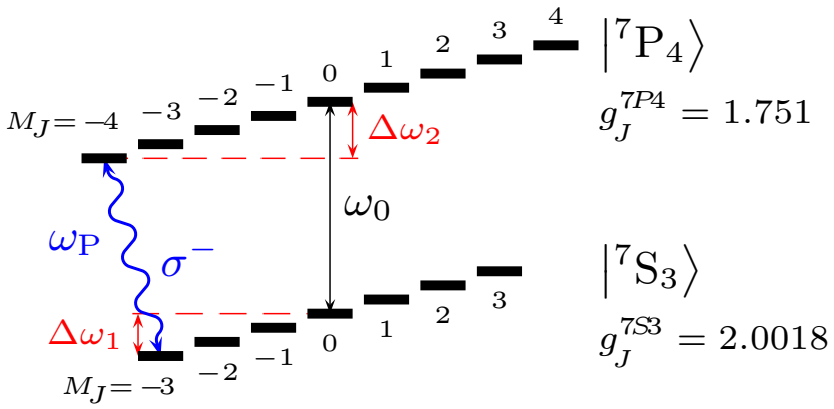


**Figure 4.13.:** *Scheme of the imaging transition to determine the Zeeman shift. To scatter enough photons the atoms in the $M_J = -3$ substate of the $^7S_3$ ground state are imaged with $\sigma^-$-polarized light. This light drives the $\Delta M_J = -1$ transition to the $M_J = -4$ substate of the $^7P_4$ level. The Zeeman shift $\Delta\omega$ of this transition is given by $\Delta\omega = \Delta\omega_2 - \Delta\omega_2 = \mu_B B(-4g_J^{7P4} + 3g_J^{7S3})/\hbar \approx -\mu_B B/\hbar$. Here $B$ is the magnetic field applied. Thus, the frequency of the imaging light $\omega_P$ has to be $\omega_P = \omega_0 + \Delta\omega$.*

detected with the absorption imaging, or even lost from the trap in the case of the inelastic three-body collisions. In addition, the lifetimes of the molecules are expected to be extremely short [84]. The binding energy released in the dissociation process leads to a heating of the cloud and atom losses. In this section I first describe the imaging system used to detect the atoms at low magnetic fields (LF), and then based on this discussion report on the realization of the HF system.

### 4.4.1. Imaging at Low Magnetic Fields

Absorption imaging requires a cycling transition, because the atoms need to scatter many photons to be detectable with a CCD camera. In LF this is realized with $\sigma^-$-polarized light on the $^7S_3 \leftrightarrow {}^7P_4$ transition (see Fig. 4.13). The LF imaging system is able to detune the 425 nm light by $-10\Gamma$ to $+15\Gamma$ ($-50$ to $+75$ MHz) relative to the unperturbed resonance frequency $\omega_0$.

Figure 4.14 shows a scheme of the LF and HF imaging system. The path of the LF imaging light is depicted in blue. With the magnetically mounted mirrors $M_1$ and $M_2$ the light can be redirected (red line) through the HF setup. I first discuss only the LF part. The light has initially a detuning of $-200$ MHz. It is a reflex of about 15 mW of the frequency-doubling cavity (for details on the laser system see e.g. [50]). The light is shifted to the required frequency with an AOM in double-pass operation. In LF the 1$^{st}$ order beam of an AOM[13] with center frequency 110 MHz is used. This allows to tune the light in the above mentioned range. After the double pass the light is injected into a polarization-maintaining fibre and brought to the experiment. It is shone into the chamber along the $x$ axis, allowing to image the atoms in the $yz$ plane. The magnetic field to keep the atoms polarized is approximately 11 G and points also into the $x$ direction (see Fig. 4.15 (a)). Therefore the light is polarized left-circular with retarding plates after the fibre to drive the cycling $\sigma^-$-transition.

To extract the atom number from an absorption image, the cross section of a photon-atom

[13] AA Optoelectronic, AA.MT.15.

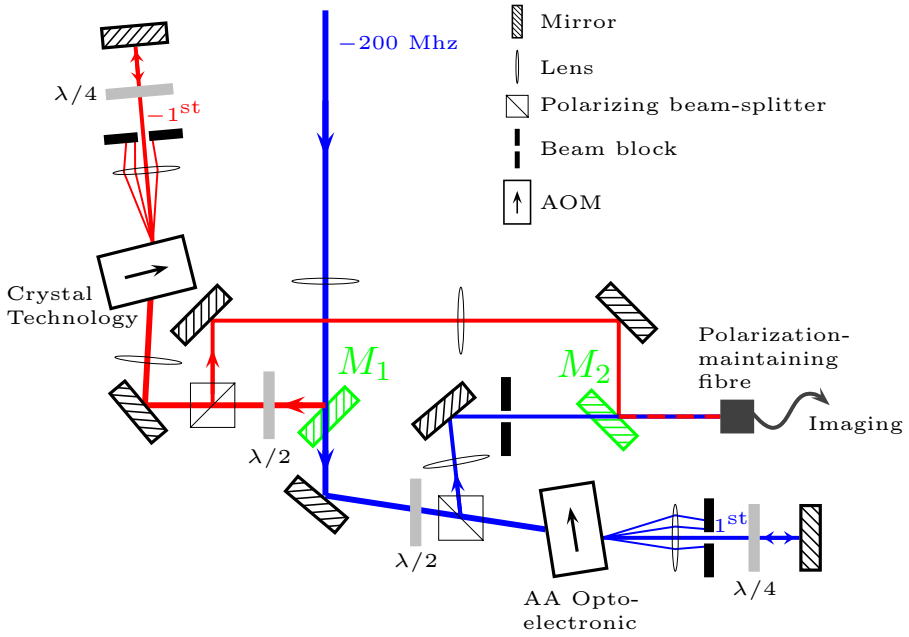


**Figure 4.14.:** *Low-field and high-field imaging setup. With the magnetically mounted mirrors $M_1$ and $M_2$ (green) the light of the LF imaging (blue line) is redirected through the HF setup (red line). In both cases a double-pass is used to shift the light to the right frequency. The AA Optoelectronic has a center frequency of 110 MHz, the Crystal Technology a center frequency of 270 MHz. In the LF system the $1^{\text{st}}$ order is used, whereas in the HF system the $-1^{\text{st}}$ order is used. The light is brought to the experiment with a polarization-maintaining fibre.*

scattering process has to be known. For a two-level system the resonant scattering cross section is given by the expression

$$\sigma_0 = 6\pi \left(\frac{\lambda_0}{2\pi}\right)^2 , \tag{4.16}$$

where $\lambda_0$ is the resonance wavelength (see for example [85] for details on atom-light interaction). In real atoms also the polarization has to be taken into account. The scattering cross section depends on the orientation of the electrical atomic dipole moment with respect to the polarization of the light. In the resonant case the relation holds

$$\sigma \propto \mu_{\text{eg}}^2 \propto \left|\langle\psi_{\text{e}}|\, \hat{\boldsymbol{\varepsilon}} \cdot \boldsymbol{r}\, |\psi_{\text{g}}\rangle\right|^2 , \tag{4.17}$$

where $\mu_{\text{eg}}$ is the dipole moment matrix element, $|\psi_{\text{e}}\rangle$ and $|\psi_{\text{g}}\rangle$ represent the excited and ground state and $\hat{\boldsymbol{\varepsilon}}$ is the polarization unit vector. With the Lambert-Beer's law

$$I_{\text{out}} = I_{\text{in}} e^{-\sigma_0 \int \mathrm{d}x\, n(\boldsymbol{r})} , \tag{4.18}$$

the integrated density profile of the atomic cloud in $x$ direction is obtained by the logarithm of incoming and outgoing light intensity:

$$\int \mathrm{d}x\, n(\boldsymbol{r}) = -\frac{1}{\sigma_0} \ln\left(\frac{I_{\text{out}}}{I_{\text{in}}}\right) = \frac{\text{OD}}{\sigma_0} . \tag{4.19}$$

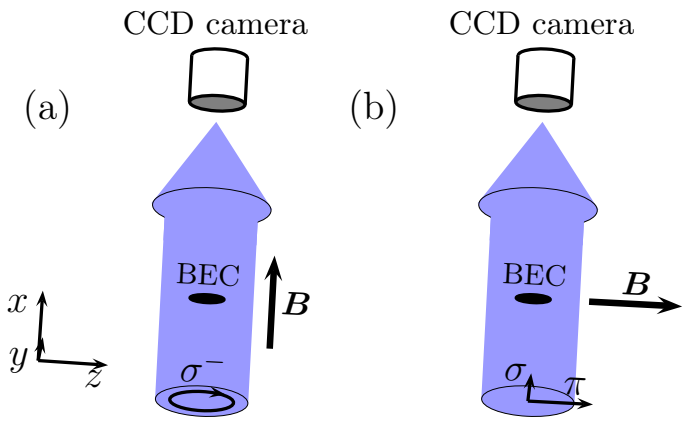


**Figure 4.15.:** *Light polarization for LF and HF imaging. (a) In LF the magnetic field points in $x$ direction. Left-circular polarized light ($\sigma^-$) drives therefore the $\Delta M_J = -1$ transition. (b) In HF there are only the possibilities of linear polarized light perpendicular to the magnetic field ($\sigma$) and parallel light ($\pi$). The $\pi$ light cannot be used as it leads to $\Delta M_J = 0$ transitions, which is not cycling.*

Here I introduced the optical density

$$\mathrm{OD} := -\ln\left(\frac{I_{\mathrm{out}}}{I_{\mathrm{in}}}\right). \tag{4.20}$$

To prepare the discussion of the scattering cross section in HF, I now describe the effect of the polarization on the cross section in LF. The LF imaging light is resonant on the $\Delta M_J = -1$ transition only. Therefore the exited state in Eq. (4.17) is in good approximation solely given by the $M_J = -4$ substate. The system is an effective two-level system and the cross section is equal to $\sigma_0$. This is of course valid only for $\sigma^-$-photons. If the imaging beam contains also a $\sigma^+$-component, the absorption of these $\sigma^+$-photons is strongly suppressed, because the light is not in resonance with the $\Delta M_J = +1$ transition. Thus, the cross section for $\sigma^+$-photons is close to zero. Linear polarized light shone in along the $x$ direction can be decomposed in $\sigma^-$ and $\sigma^+$-light, which means that a maximum of 50 % of this light is absorbed by the atomic sample. In terms of optical density this means that the OD cannot exceed $-\ln(1/2) \simeq 0.693$ (see Fig. 4.16). The functional form

$$y = -ln\left(\frac{1+e^{-x}}{2}\right) \tag{4.21}$$

of the dependence of the OD of linear polarized light ($y$) on the OD of $\sigma^-$-light ($x$) is derived in appendix C.3.

### 4.4.2. Imaging at High Magnetic Fields

The LF imaging system cannot detune the light far enough to image the atoms in HF, because the Zeeman shift is too large. The shift is approximately $-\mu_{\mathrm{B}}B/\hbar$ (see Fig. 4.13). This gives a detuning of $-840$ MHz at 600 G. Therefore a new HF imaging system had to be set up. As already described in the previous subsection, magnetically mounted mirrors are used to redirect the LF light through the HF imaging system (see Fig. 4.14). With the $-1^{\mathrm{st}}$ order

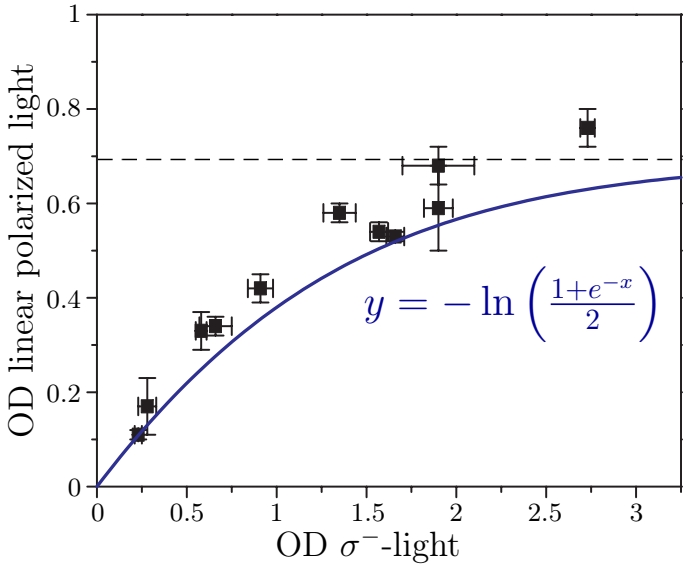


**Figure 4.16.:** *Measured optical density for linear polarized light (y) compared to $\sigma^-$-light (x). The optical densities of both polarizations were measured for various atomic densities. The blue line shows the expected relation. In the limit of total absorption for $\sigma^-$ light, the* OD *of linear polarized light goes to $-\ln(1/2)$. The error-bars correspond to the standard deviation of 3 measurements.*

of an AOM[14] with a center frequency 270 MHz in double pass operation, a detuning range of about −600 to −900 MHz is realized. This light is brought to the chamber with the same polarization-maintaining fibre as in LF. The magnetic field in HF points in $z$ direction (see Fig. 4.15 (b)), because it is produced with the offset coils of the magnetic trap. As the light is still sent in along the $x$ axis, a different polarization than in LF has to be chosen, because left-circular polarized light does not correspond to $\sigma^-$-light any more. Linear polarized light in $z$ direction is $\pi$-light driving the $\Delta M_J = 0$ transition. It cannot be used as this is not a cycling transition and the atoms scatter not enough photons. This leaves only the alternative of linear polarized light in $y$ direction ($\sigma$).

Hence, the question of the scattering cross section of this light arises. As the traveling direction of the light is perpendicular to the magnetic field, a decomposition in $\sigma^-$ and $\sigma^+$ light looses its physical meaning. Still, mathematically it can be used to give a simple argumentation that the cross section $\sigma_{\text{perp}}$ is $\sigma_0/2$ for $\sigma$-light: We can decompose the polarization vector $\hat{\boldsymbol{\varepsilon}} = \hat{\boldsymbol{y}}$ in spherical unit vectors [85]

$$\hat{\boldsymbol{u}}_{\sigma^-} = \sqrt{\frac{1}{2}}(\hat{\boldsymbol{x}} - i\hat{\boldsymbol{y}})\,, \quad \hat{\boldsymbol{u}}_{\pi} = \hat{\boldsymbol{z}}\,, \quad \hat{\boldsymbol{u}}_{\sigma^+} = -\sqrt{\frac{1}{2}}(\hat{\boldsymbol{x}} + i\hat{\boldsymbol{y}})\,. \tag{4.22}$$

Thus,

$$\hat{\boldsymbol{y}} = \frac{i}{\sqrt{2}}(\hat{\boldsymbol{u}}_{\sigma^-} + \hat{\boldsymbol{u}}_{\sigma^+})\,. \tag{4.23}$$

Like in LF the light is detuned to be resonant on the $\Delta M_J = -1$ transition only[15], conse-

[14] Crystal Technology, 3250-190.

[15] The cross section for the $\pi$-component of the light is therefore close to zero, similar to the $\sigma^+$-component in the LF case.

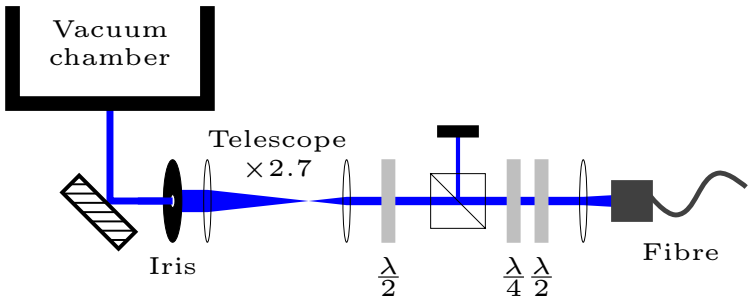


**Figure 4.17.:** *Optical elements after the polarization-maintaining fibre that brings the imaging light to the vacuum chamber. The first lens after the fibre collimates the beam coming out of the fibre. With the two lambda plates and the cube the intensity of the beam is controlled. After the cube an additional $\lambda/2$ in HF ($\lambda/4$ in LF) polarizes the beam before it is enlarged with a telescope. The iris is placed after the telescope, before the beam is directed into the chamber with a mirror.*

quently just $\hat{\boldsymbol{u}}_{\sigma^-}$ contributes to $\mu_{\mathrm{eg}}$ (Eq. 4.17). It is therefore smaller by a factor of $\sqrt{2}$ than in the LF case and the cross section $\sigma_{\mathrm{perp}}$ is smaller by a factor 2. But in contrast to linear polarized light propagating in $x$ direction, *all* photons of $\sigma$-light can be absorbed.

### 4.4.3. Fringe Reduction

With the factor 2 smaller cross section in HF the quality of the absorption images decreases, as the optical density is lower. Therefore it is more difficult to determine the density profile of the atomic cloud, because the influence of fringes increases. These interference patterns are produced by any small dust particle on the optical elements behind the fibre that brings the imaging light to the chamber. These optical elements are shown in Fig. 4.17. Besides a $\lambda/2$ and a $\lambda/4$ retarding plate and a polarizing beam-splitter to adjust the intensity, and a $\lambda/2$ (respectively $\lambda/4$ in LF) retarding plate for the polarization, there are three lenses to collimate and enlarge the beam before it is sent into the chamber with a mirror under 45 °. If the position of the dust particles on these elements was stable in the first two of the three images that are taken for absorption imaging (see for example [50] for information on the exact procedure), the fringes would cancel out in the final processed image. However, on the timescale of 350 ms between these two pictures, the position is not stable and fringes remain. Figure 4.18 (a) shows an absorption image of a condensate in HF after 8 ms time-of-flight. It is evident that the interference pattern deforms the absorption profile of the cloud.

In reference [50] a method is described to reduce the fringes in the images by postprocessing the images. Here I describe a very effective *experimental* method to reduce the fringes. It does not need a postprocessing of the images and works at least as good as the method described in [50]. The idea is to place an iris in the optical path of the imaging light to spatially filter it. The iris is placed after the telescope to enlarge the beam. It diffracts the light, which reduces the spot size on the camera to about $1 \times 1$ mm. The method is therefore only applicable for atomic clouds with a size smaller than 1 mm. This condition is fulfilled for a Bose-Einstein condensate, even after long time-of-flights. The diffracted light on the camera has a shape similar to a Gaussian profile with almost no fringes visible. If the cloud is imaged with this light, absorption pictures as shown in Fig. 4.18 (b) are obtained. Shown is a condensate in HF after 8 ms time-of-flight like in Fig. 4.18 (a). This high quality images

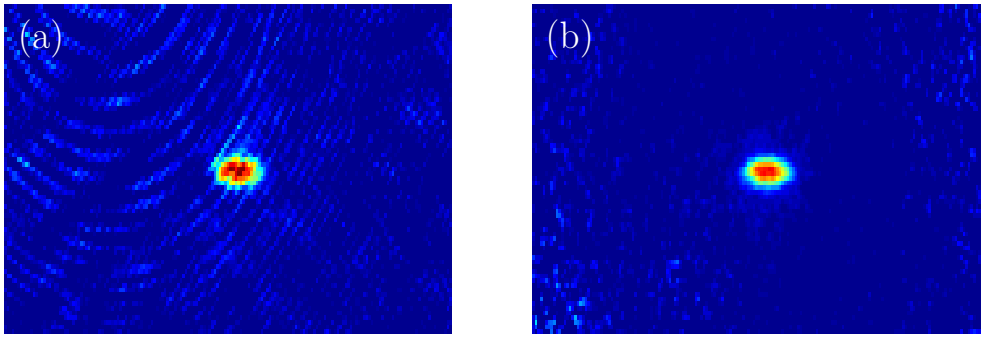


**Figure 4.18.:** *Fringe reduction with the iris method. (a) Absorption image with the normal imaging without using the iris. The interference pattern deforming the absorption profile makes it more difficult to determine the density profile of the cloud. (b) With the two irises in the optical path of the imaging light, the spatial filtering leads to a suppression of the fringes and the quality of the images improves significantly. The field of view is* $450 \times 450$ $\mu m$ *in both pictures.*

allow to determine the density profile even for low optical densities. It is not completely clear, why the method works so well. It seems that dust particles in the outer regions of the imaging beam cause most of the fringes which occur without the iris. The influence of these dust particles is strongly reduced by the cut-off of the iris, as well as by the reduced beam size after the iris.

# 5. Strong Dipolar Effects in a Chromium Bose-Einstein Condensate

*This chapter summarizes the experimental results on strong dipolar effects in a Bose-Einstein condensate. With a Feshbach resonance the scattering length is reduced by up to a factor of 5 and thus the dipolar parameter $\varepsilon_{\mathrm{dd}}$ is increased accordingly. This means that the dipolar parameter is tuned close to one, where a dipolar collapse of the BEC is expected for the trap geometries used. Our experimental control on the system is demonstrated with a series of time-of-flight measurements for various relative strengths of the dipole-dipole interaction. For the largest values reached it is shown, that even the standard 'smoking gun' evidence for Bose-Einstein condensation, an inversion of the ellipticity of the condensate during the free expansion, does not apply anymore. The results presented here constitute the first realization of a quantum-degenerate gas with such strong dipolar effects [1]. They are the first step in the exploration of the unique properties of quantum ferrofluids. This chapter is organized as follows: In section 5.1 the Feshbach resonance at 589.1 G is characterized, which is used to tune the scattering length. Both the lifetime of the condensate and the scattering length close to the resonance are presented. In section 5.2 the enhancement of the relative strength of the dipole-dipole to the contact interaction is investigated. The dependence of the condensate aspect ratio on the dipolar parameter is discussed. Finally the series of time-of-flight measurements for various $\varepsilon_{\mathrm{dd}}$ is presented.*

## 5.1. Lifetime and Scattering Length Close to a Feshbach Resonance

The realization of a Bose-Einstein condensate at high magnetic fields (described in section 4.3) allows us to study the properties of the quantum-degenerate gas in the vicinity of the Feshbach resonance at 589.1 G. This resonance is chosen for the experiments, as it is predicted to have the largest width ($\Delta B$ = 1.7 G) of the 14 resonances found in 2004 [12]. Therefore the requirement on the magnetic field stability is least stringent and the condensate properties are measured with the highest precision. The absolute position $B_{\mathrm{res}}$ of the resonance is found to coincide with the value measured in [12] by observing enhanced inelastic losses in a thermal cloud. The magnetic field is calibrated both with the knowledge of the position of lower lying resonances, which have been determined precisely with RF spectroscopy in [12], and with the measured optimal detuning of the high-field imaging system. The error in the determination of the absolute position is approximately 1 %.

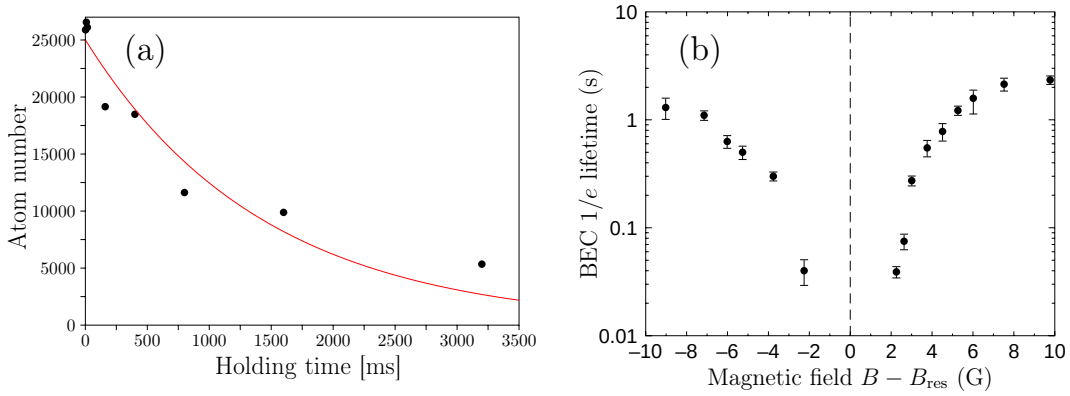


**Figure 5.1.:** *(a) Decay curve of a condensate at a magnetic field 10 G below the resonance. For simplicity the data is fitted with an exponential decay law (red line) to obtain the lifetime (*$1.4 \pm 0.3$ *s). (b) 1/e lifetimes determined with this fit function for various magnetic fields close to the resonance position* $B_{\mathrm{res}} = 589.1$ *G (dashed line). On both sides of the resonance the lifetime decreases strongly.*

### 5.1.1. Lifetime of the Condensate

In a first series of measurements the lifetime of the BEC close to the resonance is measured. Already in these measurements a variation of the condensate size and shape close to the resonance is apparent. However, this effect has been studied in more detail in separate experiments, which is described in subsection 5.1.2 and section 5.2. Three-body losses are greatly enhanced near a resonance and lead to a rapid decay of the condensate. As discussed in section 2.2, the three-body loss coefficient $L_3$ is predicted to scale universally with the fourth power of $a$ for large scattering lengths [56]. This scaling law explains enhanced losses for a diverging scattering length. But also for a decreasing scattering length enhanced losses were observed, for example in [57]. In our case we observe also enhanced inelastic losses on both sides of the Feshbach resonance.

The experimental sequence to measure the lifetime is as follows: First a Bose-Einstein condensate is produced with the sequence described in section 4.3. The curvature compensation current is set to $I_{\mathrm{pinch}} = 15.6$ A to be able to condense. Due to the enhanced three-body losses, the resonance cannot be crossed without destroying the BEC. Therefore the magnetic field at which the forced evaporation is done in the dipole trap is set to 600 G or 575 G respectively, depending whether the resonance is approached from above or below in the measurement. After the evaporation the magnetic field is ramped to a value $B$ close to the resonance in 50 ms. The cloud is kept at the field $B$ for a variable holding time and imaged after 6 ms of free expansion. If both background collisions and two-body collisions are neglected, the decrease of the atom number with the holding time is determined by Eq. (2.28). However, for simplicity the decay curves are fitted with an exponential decay law.

Figure 5.1 (a) shows the decrease in atom number with time at a magnetic field about 10 G below the resonance. The $1/e$ lifetime determined with the exponential fit (red line) is $1.4 \pm 0.3$ s. The relatively large deviation of the fit curve cannot be contributed to the too simple fit function used, as the typical dispersion of the measured atom number is on the order of the deviation. In Fig. 5.1 (b) the $1/e$ lifetime is plotted for various magnetic fields close to the resonance. Similar to the observations in [57], the lifetime decreases strongly when the resonance is approached from either side. However, the lifetime of about 40 ms at 2 G above

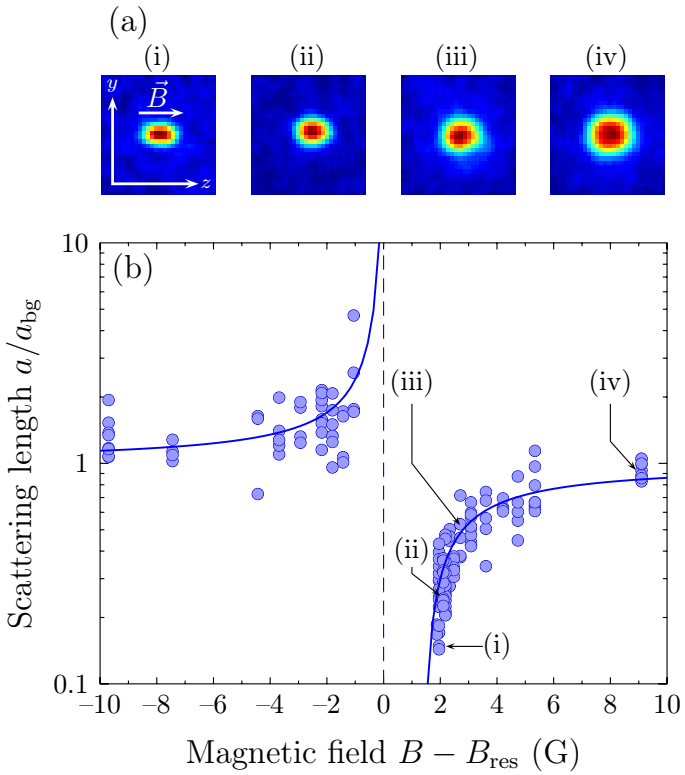


**Figure 5.2.:** *(a) Series of absorption images for various magnetic field values close to the resonance ($B - B_{res} = 2$, 2.2, 2.7 and 9 G for (i),(ii),(iii) and (iv), respectively). The images are taken after 5 ms of free expansion. The field of view is $260 \times 260$ $\mu$m. The cloud shrinks when approaching the resonance because the scattering length decreases. Moreover a significant change of the condensate shape is visible, a clear sign of strong dipolar effects. (b) Relative variation of the scattering length with the magnetic field. The scattering length is deduced from the absorption images by using the hydrodynamic theory described in section 3.3 (see text). The scattering length shows the expected dispersive shape. A fit with the function $a(B)$ describing this behaviour (solid line) yields a width of $\Delta = 1.4 \pm 0.1$ G.*

the resonance is still large enough to observe an enhancement of dipolar effects due to the decreasing scattering length.

### 5.1.2. Tuning the Scattering Length

The variation of the scattering length in the vicinity of the Feshbach resonance leads to a decrease (respectively increase) of the Thomas-Fermi radii of the condensate. This is clearly visible in the absorption images shown in Fig. 5.2 (a). The images are taken after 5 ms of time-of-flight at various magnetic field values above the resonance (see caption of Fig. 5.2) with an experimental sequence that is optimized for a minimal time spent near the resonance. The first part of this sequence is equal to the sequence described in the previous section. After quantum-degeneracy is reached, the ramp to the final value $B$ is done in $t_{ramp} = 10$ ms instead of $t_{ramp} = 50$ ms, which is used in the lifetime measurements. The condensate is then held at this field $B$ for 2 ms to allow eddy currents induced by the magnetic field change to settle down. Subsequently, the dipole trap with trapping frequencies $(\omega_x, \omega_y, \omega_z) =$

$2\pi \times (885, 575, 599)$ Hz (8/100, see section 4.2) is switched off to let the condensate expand freely. From the absorption images the atom number $N$ of the BEC (taking into account the smaller cross section of the high-field imaging) and the Thomas-Fermi radii in $y$ and $z$ direction are obtained by a fit of the density profile.

Without dipole-dipole interaction the relative change of the scattering length to the background value $a_{\mathrm{bg}}$ far from the resonance could be easily extracted from the absorption images by using the fact that both Thomas-Fermi radii would scale as $(Na)^{1/5}$ (see section 3.1). This is not applicable in our case due to the strong dipole-dipole interaction between Chromium atoms. Already the absorption images shown in Fig. 5.2 (a) clearly demonstrate that the condensate shape changes when the scattering length decreases. This effect is a clear indication of the relative enhancement of the anisotropic dipole-dipole interaction close to the resonance, it cannot be explained with the isotropic contact interaction. Because the Thomas-Fermi radii of the BEC change significantly due to the dipole-dipole interaction, the extraction of the scattering length has to be done by using the hydrodynamic equations (3.29), which describe the condensate dynamics including dipole-dipole interaction. The equations have to be solved for the scattering length with the observed Thomas-Fermi radii $R_y$ and $R_z$, atom number $N$ and trapping frequencies as parameters.

The results of this evaluation are shown in Fig. 5.2 (b). The scattering length is plotted vs. the magnetic field in the vicinity of the resonance. Each data point corresponds to the evaluation of one absorption image. The characteristics of the Feshbach resonance (position $B_{\mathrm{res}}$ and width $\Delta B$) are extracted by fitting the data with the function $a(B)$ (Eq. (2.27)) derived in section 2.3. The position $B_{\mathrm{res}}$ obtained with this fit is used only to determine the relative position of the magnetic field value $B$ to the resonance, as the uncertainty of the absolute position is much larger. The width obtained with the fit is $\Delta B = 1.4 \pm 0.1$ G. This is in good agreement with the theoretical prediction of 1.7 G [12]. Figure 5.2 (b) shows that in total the scattering length is tuned by one order of magnitude. Above the resonance $a$ is reduced by a factor of 5. This reduction allows us to observe strong dipolar effects, which is discussed in the next section.

In the remaining part of this subsection I discuss the assumptions that are underlying the data analysis. Three assumptions are made:

1. The remaining curvatures in radial and axial do not influence the condensate expansion on the time-of-flight timescale.

2. The condensate stays in equilibrium during the magnetic field ramps.

3. The Thomas-Fermi approximation is valid and thus also the classical hydrodynamics approximation described in chapter 3.

The first assumption can be checked with a small calculation. The cloud has a size of about 100 $\mu$m after 5 ms time-of-flight. With a maximal remaining curvature corresponding to 10 Hz (see section 4.3) two atoms separated by 100 $\mu$m are accelerated with a difference of $\Delta a \approx 0.4$ m/s$^2$. In 5 ms this leads to a relative change of their positions by 5 $\mu$m, which is still smaller than the resolution of our imaging system and therefore negligible.

The second assumption is checked with the adiabaticity criterion $\dot{E}/E \ll \omega_{\mathrm{min}}$, where $\omega_{\mathrm{min}}$ is the smallest trap frequency. The important energy in this context is the chemical potential

$\mu$ (Eq. (3.12)). Hence, the conditions that have to be checked are

$$\dot{a}/a \ll \omega_{\min} \quad \text{and} \quad \dot{N}/N \ll \omega_{\min}\,. \tag{5.1}$$

Whereas the condition $\dot{N}/N \ll \omega_{\min}$ is largely fulfilled for our data, checked with the measured lifetimes, the used ramp speed results in an $\dot{a}/a$ which starts to be on the order of $\omega_{\min}$ for the measurements closest to the resonance. For these data points $\dot{a}/a$ is approximately 2.3 $\mathrm{ms}^{-1}$, whereas $\omega_{\min} \approx 3.6\ \mathrm{ms}^{-1}$. Therefore it is ensured in an additional series of experiment, that no collective oscillations of the condensate are excited. This is done by varying the holding time at the magnetic field $B$ before the condensate is released from the trap. No temporal change of the Thomas-Fermi radii of the condensate is observed. Hence, the second assumption is also fulfilled, the scattering length is changed adiabatically.

The third assumption is valid if the parameter $Na/a_{\mathrm{ho}}$ describing the applicability of the Thomas-Fermi approximation (see section 3.1) is much larger than 1. Indeed, when calculating this value with the atom number $N$, the extracted scattering length $a$ and the measured trapping frequencies, it turns out to be always larger than $\sim 60$ for our parameters. Thus, also the third assumption is fulfilled.

## 5.2. Strong Dipolar Effects

This section discusses the main results of this thesis. The tuning of the scattering length $a$ allows us to observe strong dipolar effects in a Bose-Einstein condensate way beyond the perturbative regime. These dipolar effects induce a change of the condensate shape, which is measured with the aspect ratio $A_{yz} = R_y/R_z$ of the Thomas-Fermi radii. For the smallest values of the scattering length reached, the dipolar parameter $\varepsilon_{\mathrm{dd}}$ is close to one, leading even to a suppression of the inversion of the ellipticity of the condensate. The results constitute the first realization of a quantum ferrofluid.

### 5.2.1. Variation of the Condensate Aspect Ratio

In the absorption images shown in the previous section (Fig. 5.2 (a)) the change of the condensate aspect ratio when approaching the resonance is evident. The deviation of the condensate shape compared to a BEC with pure contact interaction depends on the relative strength of the dipole-dipole interaction, expressed by the dipolar parameter $\varepsilon_{\mathrm{dd}}$ (Eq. (3.23)). This dipolar parameter is calculated with the scattering length obtained in the previous section. The analysis shows that $\varepsilon_{\mathrm{dd}}$ is tuned reliably in a range of approximately 0.1 to 0.8 from the background value of $\varepsilon_{\mathrm{dd}}^{\mathrm{bg}} = 0.16$.

In Fig 5.3 the variation of the aspect ratio with $\varepsilon_{\mathrm{dd}}$ is shown. One can clearly see, that with increasing $\varepsilon_{\mathrm{dd}}$ the dipole-dipole interaction starts to dominate the cloud shape. The condensate gets elongated in the magnetic field direction ($z$), leading to a decrease of the aspect ratio $A_{yz}$. As explained in section 3.3 this is a clear indication of the dipole-dipole interaction: The mean-field potential $V_{\mathrm{dd}}^{\mathrm{mean}}$ (Eq. (3.25)) has a saddle shape, which results in an elongation in the magnetic field direction and a reduction of the size in the directions perpendicular to it. With increasing $\varepsilon_{\mathrm{dd}}$ the influence of the contact interaction on the condensate shape decreases and this effect becomes more apparent. The data is in very good agreement with the hydrodynamic theory describing a quantum-degenerate gas with

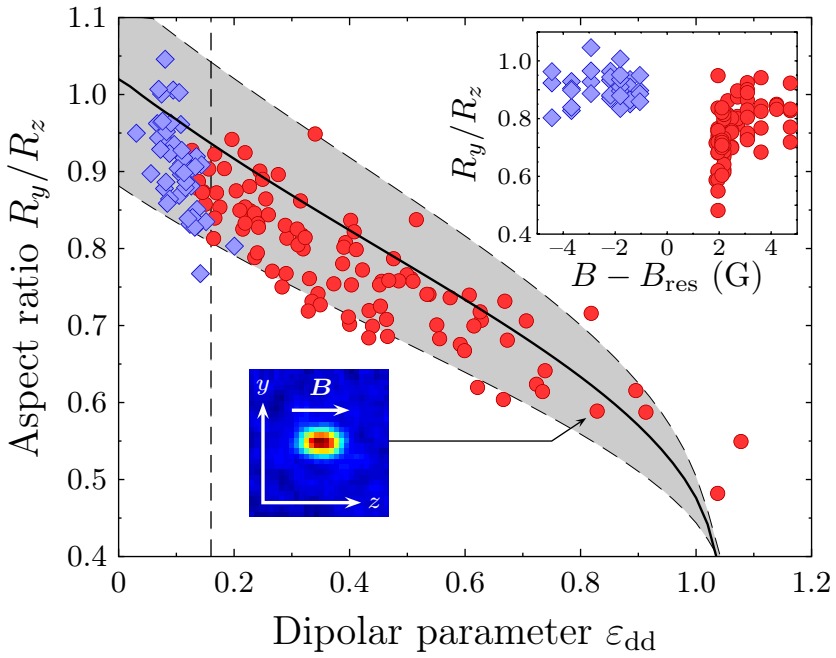


**Figure 5.3.:** *Variation of the aspect ratio $A_{yz}$ with increasing dipolar parameter $\varepsilon_{\rm dd}$. The diamonds (blue) correspond to data taken below the resonance, the circles (red) to data taken above. The vertical dashed line indicates $\varepsilon_{\rm dd}^{\rm bg} = 0.16$ which corresponds to the background scattering length $a_{\rm bg}$. The solid theory curve is obtained by solving the hydrodynamic equations (3.29), without any adjustable parameter. The gray shaded area results from the uncertainty of the trapping frequencies of approximately ±5 % (see text). The inset in the top right corner shows the variation of $A_{yz}$ with the magnetic field. It changes significantly only just above the resonance, where the scattering length approaches zero. The absorption image shows an example of a condensate with strong dipole-dipole interaction.*

dipole-dipole interaction (solid line). No adjustable parameter is used to calculate the theory curve.

Let us discuss the results in more detail. The diamonds (blue) correspond to data taken below the resonance. As can be seen in the inset of Fig. 5.3, the aspect ratio does not vary significantly when the resonance is approached from below. In the $A_{yz}$ vs. $\varepsilon_{\rm dd}$ plot nearly all of these data points are left to the vertical dashed line, which marks $\varepsilon_{\rm dd}^{\rm bg} = 0.16$, in full consistency with the hydrodynamic theory. Approaching the resonance from above, the aspect ratio does not vary significantly, too, until $B - B_{\rm res} \lesssim 3$ G. At this point it starts to decrease strongly in the range down to $B - B_{\rm res} \approx 2$ G, which is still addressable without a collapse of the condensate. The used trap geometry is cigar-shaped, which is predicted to lead to instabilities if $\varepsilon_{\rm dd}$ exceeds one (see section 3.3). However, this dipolar collapse cannot be distinguished from a collapse due to a negative scattering length for our parameters. With the realization of a pancake-shaped trap and a better magnetic field stability it should be possible to explore also the stability properties (see outlook).

The largest uncertainty in the theoretical prediction of $A_{yz}(\varepsilon_{\rm dd})$ arises from the trapping frequencies. As described in section 4.2, the frequencies can be determined with high precision by exciting a center of mass motion. However, the frequencies depend strongly on the alignment of the dipole trap beams. The accuracy of the measured values is therefore

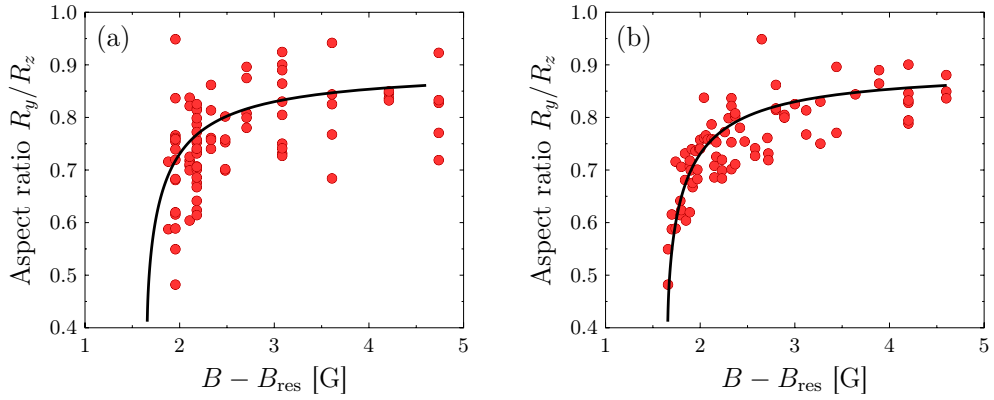


**Figure 5.4.:** *Comparison of (a) the dispersion of a presentation of $A_{yz}$ vs. the measured magnetic field, with (b) the dispersion of $A_{yz}$ vs. the extracted magnetic field. Shown is in both cases the variation of the aspect ratio when approaching the resonance from above. In the presentation vs. the measured magnetic field, systematic errors in the magnetic field determination lead to a dispersion of approximately* 0.3*. If $A_{yz}$ is plotted vs. the magnetic field value that is extracted from the absorption images (see text for details), the dispersion decreases by a factor of 3.*

estimated to be ±5 %. This 5 % uncertainty gives rise to the gray shaded area indicated in Fig 5.3. Nearly all data points lie within this area. Whereas the dispersion in the $A_{yz}$ vs. $B$ graph is relatively large close to the resonance (about 0.3), the dispersion in the presentation vs. $\varepsilon_{\mathrm{dd}}$ is about 3 times smaller[1]. This is because the presentation vs. $\varepsilon_{\mathrm{dd}}$ is *not sensitive* to systematic errors arising from an uncertainty in the determination of the magnetic field. The aspect ratio $A_{yz}$ and $\varepsilon_{\mathrm{dd}}$ are extracted directly from the absorption images without using the measured magnetic field value. The magnetic field drift, which is on the order of 0.5 G during several hours, has therefore no influence.

One can even go a step further and make a reversed analysis: The magnetic field value corresponding to each absorption image can be calculated from the scattering length which is obtained from the image. If the aspect ratio $A_{yz}$ is plotted as a function of this *extracted* magnetic field value, the systematic error of the *measured* magnetic field is avoided. Figure 5.4 compares the dispersion of the aspect ratio when using the extracted $B$ with the dispersion when plotting vs. the measured magnetic field. It is evident that the dispersion is reduced by a factor of 3 in this way like in the graph of $A_{yz}(\varepsilon_{\mathrm{dd}})$ (Fig. 5.3). With the reduced dispersion the data agrees much better with the solid theory curve (again calculated using the hydrodynamic theory without any adjustable parameter).

### 5.2.2. Time-of-Flight Measurements

As an application of the tunability of the dipolar parameter $\varepsilon_{\mathrm{dd}}$, the expansion of the BEC is studied for two different orientations of the magnetic dipoles with respect to the trap. This measurement has been done already at low magnetic fields by Stuhler and coworkers [10] for the background value $\varepsilon_{\mathrm{dd}}^{\mathrm{bg}}$. However, in these measurements the dipole-dipole interaction corresponded only to a small perturbative effect. The tunability of $\varepsilon_{\mathrm{dd}}$ allows us now to access a much larger parameter range. The method described in [10] consisted of changing

[1] Excluding data points that are obviously far off the typical range.

the orientation of the magnetic field with respect to the trap. This method is not applicable in our case, as the high magnetic field required to tune $\varepsilon_{\mathrm{dd}}$ can only be produced along the $z$ direction. Therefore, in our case the trap orientation is changed with respect to the magnetic field. This is done by exchanging $\omega_y$ and $\omega_z$, while keeping the same frequency in $x$ direction.

Two traps that fulfill this condition are found experimentally by measuring trapping frequencies: Trap 1 (3/100) has the frequencies $(\omega_x, \omega_y, \omega_z) = 2\pi \times (669, 357, 566)$ Hz and trap 2 (7/42) has $(\omega_x, \omega_y, \omega_z) = 2\pi \times (658, 543, 371)$ Hz (see section 4.2). Hence, within the estimated 5 % accuracy level, $\omega_y$ (respectively $\omega_z$) of trap 1 is equal to $\omega_z$ (respectively $\omega_y$) of trap 2 and $\omega_x$ stays constant. Without dipole-dipole interaction the aspect ratio $A_{yz}$ of a BEC released from these traps would evolve inversely, as in this case the Thomas-Fermi radius in $y$ direction of the one trap would be equal to the radius in $z$ of the other trap and vice versa (see Eq. (3.22)). Thus, if we define the aspect ratio $A_1$ of trap 1 as $A_1 := R_z/R_y$ and the aspect ratio $A_2$ of trap 2 as the inverse $A_2 := R_y/R_z$, $A_1$ and $A_2$ would evolve equally.

Due to the anisotropy of the dipole-dipole interaction this is not valid in our case. The elongation in the magnetic field direction $z$ (respectively reduction of the size in $y$) results in a difference of the $y$ radii to the $z$ radii of the different traps. The difference of $A_1$ to $A_2$ is equal to the difference of $A_{yz}$ for a magnetic field pointing in $z$ direction to $A_{yz}$ for a field pointing in $y$ direction, which was measured in [10]. Our experimental protocol is completely equivalent to the change of the magnetic field orientation with respect to the trap.

Figure 5.5 presents experimental results on the temporal evolution of $A_1$ and $A_2$ at various magnetic field values in the vicinity of the Feshbach resonance. Before I discuss these results, I describe the additional measurement shown in panel (a), which is done to confirm that the two trap configurations are equal except for an exchange of $\omega_y$ and $\omega_z$. The measurement is done with the magnetic field of 11.5 G which is used for the low-field imaging (see section 4.4). This field points in $x$ direction and therefore the magnetic dipoles of the atoms are aligned perpendicular to the observation plane (see inset in panel (a)). An exchange of the trapping frequencies does thus *not* affect the aspect ratio, as the interaction between two aligned dipoles is cylindrically symmetric. Consequently, with the rotation of the trap (and hence the density distribution) around the magnetization axis also the dipole-dipole mean-field potential is rotated, leading to $A_1 = A_2$ for the two traps, similar to the situation with pure contact interaction described above. Indeed, the experimental data shows that the evolution of the aspect ratios is the same and agrees well with the theory curve (black solid line).

The aspect ratios $A_1$ and $A_2$ are measured for 5 different time-of-flights in total. The shortest time-of-flight is 4 ms. Even shorter times would allow us to investigate also the initial increase of the aspect ratios and not only the approximately constant part after $\sim 2$ ms. However, at shorter time-of-flights the condensate is too small to obtain reliable values of the Thomas-Fermi radii with the imaging system as it is now. This could be changed for example by using a larger magnification and using a weaker trap with larger Thomas-Fermi radii of the condensate.

The figures 5.5 (b)–(f) present the aspect ratios of trap 1 and 2 at the five different time-of-flight values for the high magnetic field pointing in $z$ direction. The diamonds (blue) correspond to an alignment of the long axis of the trap perpendicular to the field, the circles (red) to an alignment in the field direction (see inset in panel (b)). In Fig. 5.5 (b) the magnetic field is set to a value about 10 G above the Feshbach resonance. At this value the dipolar parameter $\varepsilon_{\mathrm{dd}}$ is approximately given by the background value $\varepsilon_{\mathrm{dd}}^{\mathrm{bg}}$. Therefore the measurement is equivalent to the situation in [10]. The results presented in this reference

are recovered, the aspect ratios $A_1$ and $A_2$ differ due to the dipole-dipole interaction. The hydrodynamic theory curves (red and blue solid line) are in good agreement with the data, without any adjustment of the parameters.

In the figures 5.5 (c)–(f) the magnetic field is subsequently set to values closer to the resonance (2.6, 2.5, 2.3 and 2.2 G respectively). With $\varepsilon_{\mathrm{dd}}$ approaching one, these measurements are far beyond the perturbative regime. The deviation of $A_1$ and $A_2$ increases, indicating the enhancement of the relative strength of the dipole-dipole interaction. At $\varepsilon_{\mathrm{dd}} = 0.75$ (panel (f)) even the standard 'smoking gun' evidence of quantum-degeneracy, an inversion of the ellipticity (see section 3.1) of the condensate, does not apply anymore. The dashed line indicating the inversion is not crossed by both the blue and the red line. $R_z$ stays always larger than $R_y$ for both traps. The black solid line indicates the theory curve without dipole-dipole interaction. The large deviation of the data to this curve is evident. However, the hydrodynamic theory including dipole-dipole interaction does still describe the evolution of the aspect ratios correctly.

In conclusion, the experiments demonstrate the first investigation of the unique properties of a quantum ferrofluid. We observe a strong modification of the condensate shape when the contact interaction is reduced. In a series of time-of-flight measurements our control on the system is demonstrated. The hydrodynamic theory introduced in section 3.3 is in excellent agreement with the measured data.

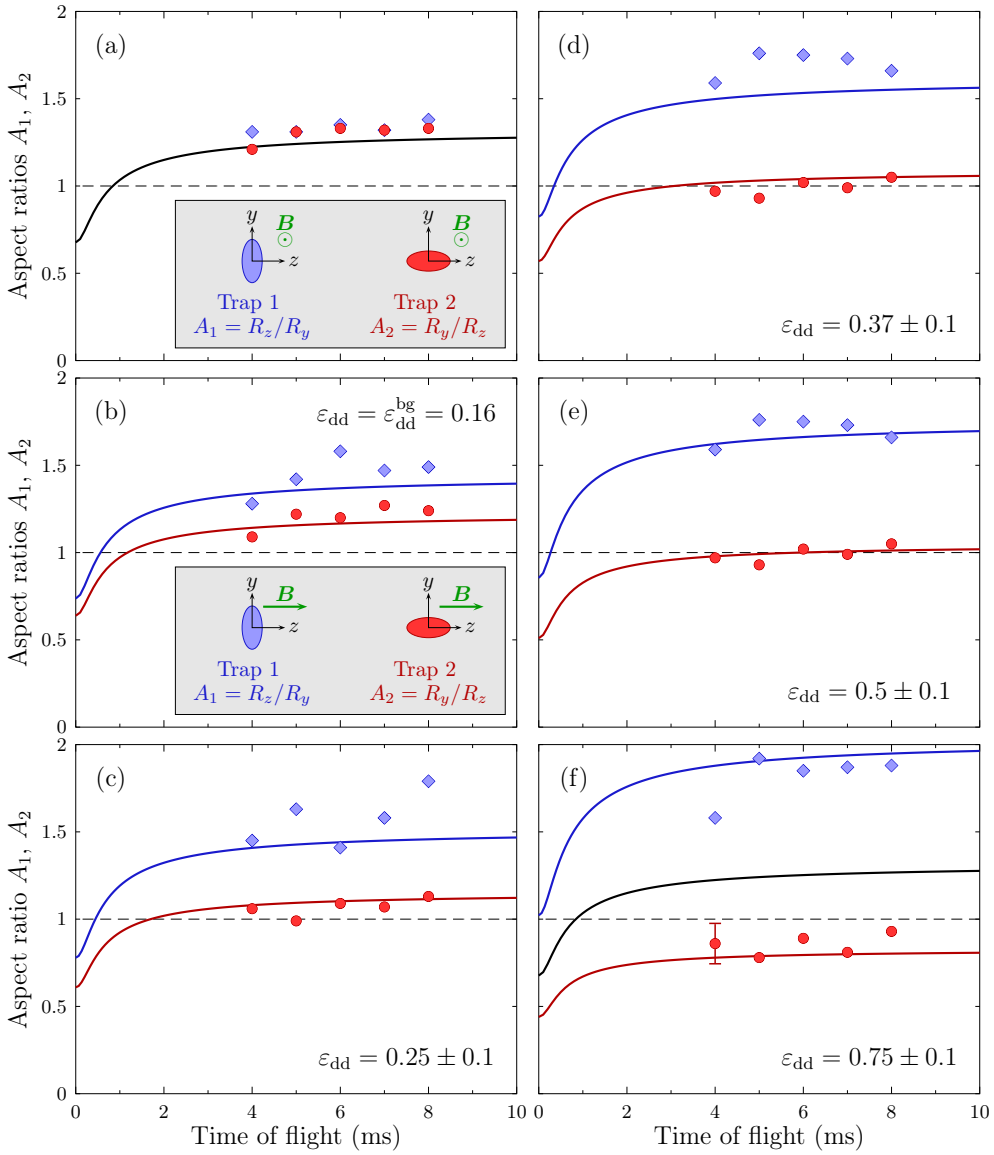


**Figure 5.5.:** *Series of time-of-flight measurements for the two traps with interchanged trapping frequencies in y and z direction (see text). The diamonds (blue) correspond to trap 1, the circles (red) to trap 2. The theory curves are obtained with the hydrodynamic theory including dipole-dipole interaction. As an example for the typical dispersion of the measured aspect ratios an error bar is included in panel (d). (a) The magnetic field points in x direction (see inset), therefore the trap is rotated around the magnetization axis and $A_1 = A_2$. (b)–(f) The trap is rotated relative to the magnetic field direction z (see inset in (b)). Therefore $A_1$ and $A_2$ start to differ. The difference increases with increasing $\varepsilon_{dd}$ (see lower, respectively upper right corner of the figures). At $\varepsilon_{dd} = 0.75$ (panel (f)) the inversion of the condensate ellipticity is suppressed by the dipole-dipole interaction. The dashed line indicating the inversion point is not crossed by both blue and red line. In this panel also the theory curve for an expansion without dipole-dipole interaction is shown (black line) to demonstrate the large deviation of the measured data to the pure contact case.*

# 6. Conclusion and Outlook

This thesis presented an experimental demonstration of strong dipolar effects in a quantum gas. Such a quantum ferrofluid is a novel kind of superfluid that promises the discovery of many new physical phenomena. The approach used in this work is based on decreasing the contact interaction with a Feshbach resonance, which results in an enhancement of the relative strength of the dipole-dipole interaction. The parameter describing the relative strength, $\varepsilon_{\mathrm{dd}}$, has been increased reliably by a factor of five to $\varepsilon_{\mathrm{dd}} = 0.8$. This corresponds to dipolar effects way beyond the perturbative regime.

The first two chapters introduced the theoretical concepts underlying the physical phenomena studied in this work. Chapter 2 discussed the theory of Feshbach resonances in general and specialized on the resonances of Chromium. Chapter 3 reported on the properties of dipolar quantum gases. After setting up this theoretical background, chapter 4 presented the apparatus that has been used to perform the experiments. The chapter focussed on the modifications of the setup which have been necessary to tune the contact interaction at the high magnetic fields. In addition, a method was described to measure the trapping frequencies of our optical dipole trap with high precision.

Finally in chapter 5 the experiments on strong dipolar effects were presented. In the first part the broadest Feshbach resonance at 589.1 G was characterized. The measured width of $1.4 \pm 0.1$ G was found to be in good agreement with the theoretical prediction of 1.7 G. The lifetime of the condensate near the resonance was found to decrease rapidly probably due to enhanced three-body losses. By approaching the resonance from above, the scattering length has been reduced by up to a factor of five. In the second part the effect of this reduction on the condensate properties was discussed. The condensate dynamics in this strong dipolar regime has been studied in a series of time-of-flight measurements.

The realization of a two-frequency acousto-optic modulator driver was another part of this thesis. The measurements on its performance to improve the pointing stability of a laser beam, were described in the appendix A. It has been shown that the stability is increased by a factor of $\sim 20$. Additionally it has been shown that also the laser power is stabilized after rapidly switching the RF driving power. Two of these drivers are now included in the experimental setup to control the intensity of the optical dipole trap beams.

The future perspectives of the experiment are very promising. The realization of a quantum gas with strong dipolar effects opens up many avenues to study the properties of this system. The next step will be to study the stability properties of a dipolar condensate. To be able to address a wide parameter range, a one-dimensional optical lattice has been set up, which now allows us to realize a stack of pancake-shaped traps. This lattice is produced by two linearly polarized laser beams at 1064 nm sent in under an angle of about $\pm 4\,^\circ$ to the imaging axis. The beams are produced with an Ytterbium fibre laser[1] with a linewidth of 70 kHz.

[1] IPG, YLR-20-1064-LPSF.

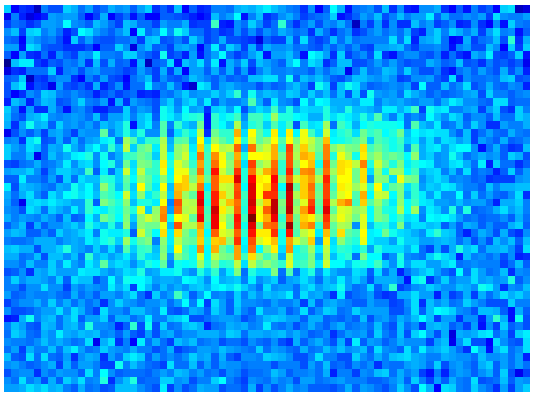

**Figure 6.1.:** *Interference pattern produced with the newly set-up one-dimensional lattice. The pattern results from an overlap of condensates of two or more different lattice sites after 15 ms time-of-flight. The phase information imprinted in these images could be used in future experiments to explore for example the physics of a double well system with dipolar interaction.*

This results in a lattice spacing of about 8 $\mu$m. The condensate can be loaded into a variable number of the lattice sites. Figure 6.1 shows an absorption image of the interference pattern produced by overlapping condensates of different sites after a time-of-flight of 15 ms. Although the near future experiments will not make use of the phase information imprinted in these interference patterns, but make use only of the new trap geometry, this is an interesting prospect for future investigations. For instance it could allow to investigate a double-well system of dipolar condensates.

For the condensate stability experiments also the magnetic field stability has to be improved further. For this reason new more stable power supplies are installed in the setup. Furthermore the closed-loop control will be replaced and the switching of the magnetic field will be separated from the current stabilization. With this steps a field stability of $10^{-5}$ peak-to-peak should be realizable, resulting in a much higher control on the scattering length $a$.

Another future direction could be the production of $Cr_2$ molecules by magnetic field ramps over one of the Feshbach resonances. These molecules will show even stronger dipole-dipole interaction, as their magnetic dipole moment can be as large as 12 $\mu_B$. In a first series of experiments molecules produced with the resonances at 589.1 and 499.9 G could not be detected. Two different detection schemes were tested. The first one was to blow away remaining atoms in the condensate with resonant light after the field was ramped over the resonance, and then dissociate the molecules by ramping back and detect them. The second scheme consisted of separating remaining atoms and molecules with a gradient produced by the pinch coils and then dissociate and detect. Also a combination of the two schemes was tested.

It is most likely that a detection failed due to the extremely short lifetime of the molecules [84] and the enhanced inelastic three-body losses. The production efficiency for molecules should be on the order of a few percent [86, 87, 88], hence, starting with $\sim$ 30000 atoms in a condensate, a few thousand molecules should be produced. The speed of the magnetic field ramps is limited due to the electronics used and eddy currents. Therefore the sequence of producing molecules, blowing away the atoms or separating them and ramping back takes $\sim$ 5 ms. With an estimated lifetime of less than 1 ms, the signal of the molecules is too weak to be

detectable. In the future the experiments could be redone with the use of the one-dimensional lattice. The quasi two-dimensional confinement in the stack of pancake traps could lead to a stabilization of the molecules due to the repulsive interaction in the pancake plane.

# A. Two-Frequency Acousto-Optic Modulator Driver

*This appendix describes the two-frequency acousto-optic modulator (AOM) driver that is used to improve the pointing stability of our optical dipole trap beams [13]. Section A.1 gives an introduction to acousto-optic modulation. Based on this, the problem of beam movement due to thermal effects is introduced in section A.2 and the two-frequency method is presented as a way to suppress this movement. Section A.3 reports on the technical realization of a two-frequency driver, including the details of an electronic circuit used for it. The last section A.4 presents the measurements that were done to test the performance of the two-frequency method.*

## A.1. Introduction to Acousto-Optic Modulation

Acousto-optic modulators are an important tool to manipulate laser beams. They are used mainly for three purposes: to deflect, to shift in frequency and to modulate the intensity of a beam [89]. Technical applications exist among many others in telecommunications or laser printing. In Atomic, Mesoscopic and Optical Physics (AMO) especially their ability to tune frequencies and modulate intensities is widely used, for example in cold atoms experiments these parameters need to be controlled precisely for many laser beams. This section gives a short introduction to the theory of acousto-optic modulation following mostly the treatment in [90]. A more detailed description can be found also in [91].

The working principle of an AOM is *Brillouin scattering* [92], i.e. the diffraction of light by a sound wave inside a crystal. A sound wave is a periodic density perturbation, which causes also a periodic change of the index of refraction. This 'grating' with a lattice spacing given by the sound wavelength $\lambda_s$ diffracts an incoming optical beam. In the limit of a thick grating, i.e. the optical path length in the perturbed region is large compared to $\lambda_s$, a theoretical description is given by the Bragg diffraction analogous to the diffraction of X-rays in a crystal: If the path difference $2d$ between reflection on two adjacent acoustic wave fronts (see Fig. A.1) is an integer multiple $m$ of the light wavelength $\lambda$[1], the reflected beams interfere in phase, which leads to a bright diffraction peak. The angle of incidence at which this condition is fulfilled is called Bragg angle $\theta_B$. It can be calculated by using $d = \sin\theta_i \lambda_s$, where $\theta_i$ is the angle between incoming beam and sound wave. Hence, the condition reads

$$2\lambda_s \sin\theta_B = m\lambda\,. \tag{A.1}$$

In the Bragg limit it is possible to diffract up to 100% of the light in one order $m$, whereas in

[1] Actually one has to use the wavelength in the crystal $\lambda/n$, where $n$ is the refractive index. But, due to refraction at the surface air - crystal, the $n$ cancels out in the final equation for the Bragg angle and is not taken into account.

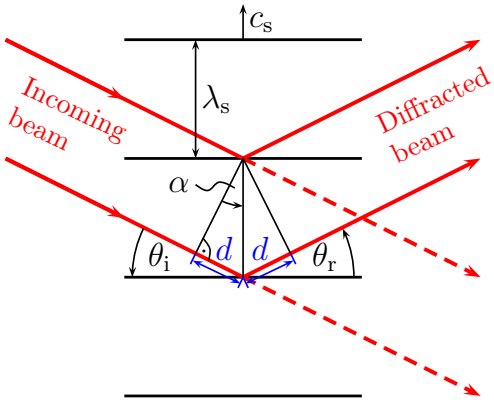


**Figure A.1.:** *Diffraction of an optical beam by a sound wave with wavelength $\lambda_s$ and velocity $c_s$. The periodic modulation of the index of refraction leads to a partial reflection of the incoming beam on the acoustic wave fronts at an angle $\theta_r = \theta_i$. The distance $d$, which is half the path difference between reflection on two adjacent wave fronts, is given by $d = \lambda_s \sin\alpha$, where $\alpha$ is equal to $\theta_i$.*

the limit of a thin grating (the so called Raman-Nath regime) the periodic modulation leads only to a small phase shift and the light is diffracted in many orders [93]. This regime is not discussed here, as acousto-optic devices are operated usually in the Bragg regime.

Up to now the fact that the 'grating' is moving has not been taken into account. With the picture in mind that the wavefronts act as small partially reflecting mirrors it is easy to understand that the movement gives rise to a Doppler shift of the diffracted light. A different approach of understanding this is by the use of phonons. In a particle picture diffraction corresponds to absorption or stimulated emission of phonons by photons. An incoming photon with energy $\hbar\omega_i$ and momentum $\hbar\mathbf{k}_i$ absorbs/emits one or more phonons with $\hbar\omega_s$ and $\hbar\mathbf{k}_s$. Energy and momentum are conserved in such a process, hence for one absorption this gives

$$\omega_d = \omega_i + \omega_s\,, \tag{A.2}$$

$$\mathbf{k}_d = \mathbf{k}_i + \mathbf{k}_s \tag{A.3}$$

for the outgoing photon. Thus, the diffracted light is shifted in frequency by $f_s = \omega_s/2\pi$. The momentum conservation is equivalent to the Bragg condition since the sound frequencies of interest are on the order of $10^8$ Hz (radio-frequencies) and therefore much smaller than the light frequency (around $10^{14}$ Hz). Hence, $\omega_d \approx \omega_i$ and consequently $k_d \approx k_i$, which gives

$$k_s = 2k_i \sin\theta_B \tag{A.4}$$

(see Fig. A.2) and recovers Eq. (A.1) by using $k_s = 2\pi/\lambda_s$.

The intense sound wave in the crystal is generated with a radio-frequency (RF) signal by a piezo-electric transducer. Commonly used crystals consist for example of Tellurium Dioxide ($TeO_2$) for the visible and near-infrared, or of Germanium (Ge) for the mid-infrared. The creation of a standing wave is avoided by absorbing the sound wave at the end face. The fraction of light that is diffracted out of an incoming laser beam is determined by the intensity of the acoustic wave $I_{\text{acoustic}}$, and thus by the power of the RF signal $P_{\text{RF}}$. The ratio

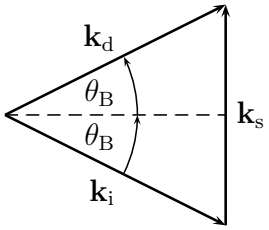


**Figure A.2.:** *Momentum conservation in a phonon absorption process. The momenta of photon $\hbar\mathbf{k}_\mathrm{i}$ and phonon $\hbar\mathbf{k}_\mathrm{s}$ add up to the momentum of the diffracted photon $\hbar\mathbf{k}_\mathrm{d}$. Using $k_\mathrm{d} \approx k_\mathrm{i}$ recovers the Bragg condition (see text).*

of diffracted to incoming light

$$\frac{I_\mathrm{diffr.}}{I_\mathrm{incom.}} = \sin\left(\frac{\pi l}{\sqrt{2}\lambda}\sqrt{M I_\mathrm{acoustic}}\right)^2, \tag{A.5}$$

depends on the diffraction figure of merit $M$ [90]. The figure of merit is equal to

$$M = \frac{n^6 p^2}{\rho c_\mathrm{s}^3}, \tag{A.6}$$

when expressed in terms of sound velocity $c_\mathrm{s}$, refractive index $n$, photo-elastic constant $p$ and mass density $\rho$. $c_\mathrm{s}$ depends on the direction of propagation and the polarization, which is either longitudinal or transversal (sheer mode). Therefore Eq. (A.5) shows that the RF power $P_\mathrm{max}$ needed for maximum diffraction efficiency is determined by the material and the acoustic mode. A typical value for a $TeO_2$ crystal using a longitudinal mode with $c_\mathrm{s} = 4200$ m/s is $P_\mathrm{max} = 2.5$ W. The Bragg angle is 13.9 mrad for a wavelength $\lambda = 1060$ nm and a radio-frequency of $f = 110$ MHz.

## A.2. Improving the Beam Stability with the Two-Frequency Method

In our setup one important application of AOMs is to control the intensity of the optical dipole trap beams. As explained in section 4.1 our trap is formed by two far off-resonant beams which are overlapped on a 10 $\mu$m scale. The depth and shape of this trap is changed by varying the power of either beam. In addition, the trap characteristics depend on the relative position of the beams, which has to be controlled on the 10 $\mu$m length scale. This requirement gets even more stringent with the newly set up one-dimensional optical lattice (see outlook). It turns out that the pointing stability of a beam that is diffracted by an AOM can thus cause problems: When the RF power $P_\mathrm{RF}$ driving the AOM is changed in order to change the diffracted light intensity, thermal effects inside the AOM lead to a movement of the beam which is on the order of 1 mrad and takes place on a timescale of several seconds. One way to circumvent this, is to use a single-mode optical fibre behind the AOM, but this cannot be done for high power lasers[2]. Another option is to adjust the RF frequency

[2]Such as $CO_2$ or Ytterbium fibre lasers.

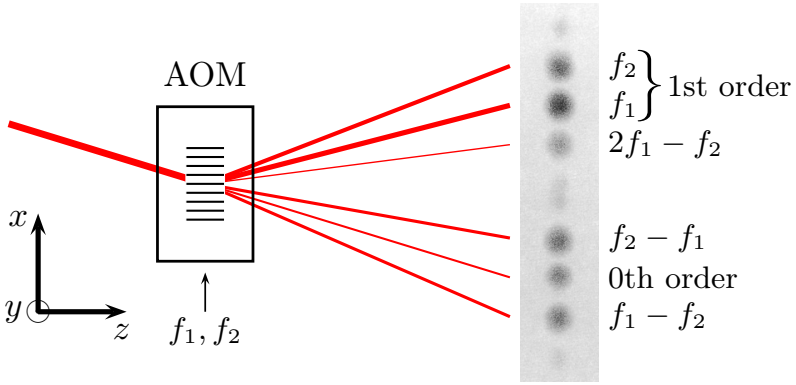


**Figure A.3.:** *Schematic of an AOM that is driven by two frequencies. The incoming laser beam is diffracted in many different orders. The image shows a picture of these multiple diffraction orders, whose frequency shifts are indicated on the right hand side of the image.*

to compensate the movement. However, in this section a different approach is discussed, which is adaptable to any AOM and easier to realize than a compensation by changing the frequency[3]. Furthermore, it stabilizes also the diffracted light intensity.

If $P_{\mathrm{RF}}$ is reduced, less power has to be absorbed at the end face of the crystal. This changes the temperature of crystal and surrounding parts, which causes the beam movement. The idea of the two-frequency method is to drive the AOM always with the same power $P_{\mathrm{RF}}$ and thus keep the temperature stable. For this, the AOM is driven with two frequencies $f_1$ and $f_2$ and the power $P_2$ of $f_2$ is adjusted relative to $P_1$ of $f_1$ to keep the total power $P_{\mathrm{RF}} = P_1 + P_2$ constant. Light diffracted by an AOM driven by two frequencies is diffracted in many different beams, as is shown in Fig. A.3. Besides the zeroth and first order of $f_1$ and $f_2$, second and even third order beams corresponding to multiple absorption and stimulated emission of phonons can be seen [94].

Three things have to be kept in mind when choosing the frequencies $f_1$ and $f_2$: The difference $f_2 - f_1$ has to be sufficiently large to ensure that the two first order beams are easy to separate. However, the frequencies have to be still within the bandwidth of the AOM. In addition, the power reflected of the AOM at the two frequencies should be approximately equal, which guarantees that $P_{\mathrm{RF}}$ is constant not only after the RF source, but also in the AOM.

## A.3. Technical Realization of a Two-Frequency Driver

As a part of this thesis 2 two-frequency drivers were realized, which are now included in the setup to control the intensity of the dipole trap beams. They were built using standard Mini-Circuits RF components and are described in this section. A schematic illustration of a two-frequency driver is shown in Fig. A.4, together with a single frequency driver. The latter one consists of a voltage-controlled oscillator (VCO)[4], which generates an RF signal

[3] Because it does not need a calibration that is dependend on the speed of the change of $P_{\mathrm{RF}}$, which is crucial for the frequency compensation.

[4] Mini-Circuits, POS-150.

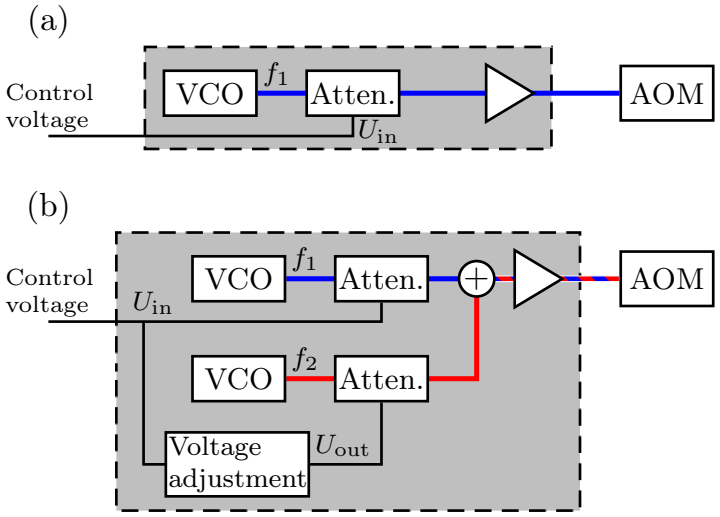


**Figure A.4.:** *(a) Typical setup for driving an AOM with variable RF power. A voltage-controlled oscillator (VCO) generates the radio-frequency $f_1$ (blue line), which is attenuated to a value given by the control voltage $U_{\text{in}}$. The signal is then amplified before going to the AOM. (b) For the two-frequency driver an extra VCO and attenuator is added. The additional VCO generates the second RF signal $f_2$ (red line), whose power is adjusted relative to $f_1$ to keep the total power in the AOM constant. This adjustment is done by modifying the control voltage $U_{\text{in}}$ with an electronic circuit.*

whose amplitude can be changed by an electronic attenuator[5] before it is amplified with a constant gain[6]. Hence, by changing the voltage applied to the attenuator the output power of the driver is changed. For the two-frequency driver a second identical VCO and attenuator is added. The power $P_2$ of frequency $f_2$ generated by the second VCO is adjusted relative to the power $P_1$ of $f_1$ by modifying the control voltage $U_{\text{in}}$. The electronic circuit used for this is explained in detail in the next paragraph. The transfer function of the circuit $U_{\text{out}}(U_{\text{in}})$ has to be a nonlinear function due to the nonlinear dependence of the output power on the control voltage. The required transfer function is obtained by measuring the control voltage of frequency $f_2$ which keeps the total power $P_{\text{RF}}$ constant *behind* the amplifier, for various powers of $f_1$. It is important to measure the total power behind the amplifier, as saturation effects can have an influence on the calibration of $P_{\text{RF}}$.

Figure A.5 shows a diagram of the electronic circuit that is used to generate the nonlinear function. The circuit approximates the measured calibration curve by a stepwise linear function[7]. The main idea of the circuit is to use an inverting amplifier whose gain is changed when a Zener diode gets conducting. For example, if $U_{\text{in}}$ is smaller than 4.3 V, the Zener voltage of the first diode, the gain of the first amplifier is just given by

$$-\frac{R_{11}+R_{12}}{R_1+R_2}\,. \tag{A.7}$$

[5]Mini-Circuits, PAS-3.
[6]Mini-Circuits, ZHL-1-2W.
[7]With this circuit only monotonic functions can be approximated.

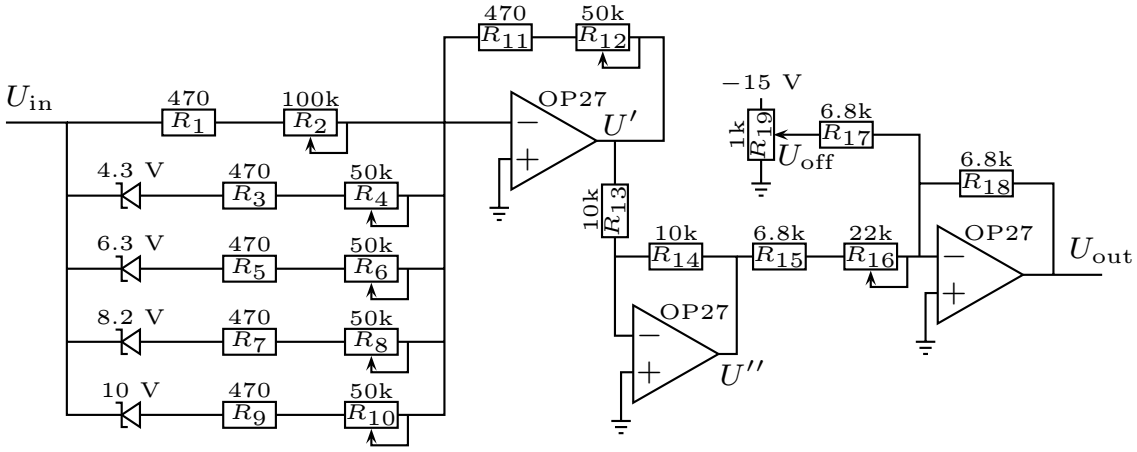


**Figure A.5.:** *Diagram of the electronic circuit for adjusting the control voltage. The gain of the first inverting amplifier depends on the voltage $U_{\text{in}}$ due to the Zener diodes. After inverting the amplified voltage $U'$ of this first stage to $U''$, it is added with a variable gain to $U_{\text{off}}$ to obtain the output voltage $U_{\text{out}}$.*

If $4.3\,\text{V} \leqslant U_{\text{in}} \leqslant 6.3$ V, the first Zener diode gets conducting and the gain increases to

$$-\frac{(R_{11}+R_{12})}{(R_1+R_2) \parallel (R_3+R_4)}\,, \tag{A.8}$$

where $\parallel$ means parallel connection of the resistors. Hence, by using many diodes a stepwise linear function is generated. In our case four diodes with Zener voltages of 4.3 V, 6.3 V, 8.2 V and 10 V are used[8]. The 50 kΩ and 100 kΩ potentiometers allow for a flexible transfer function. The voltage $U'$ at the output of the first operational amplifier is inverted to $U''$ before the offset voltage $U_{\text{off}}$ is added. The potentiometer $R_{16}$ allows for an extra gain in the last step. The transfer function of the circuit is shown in Fig. A.6, together with $P_{\text{RF}}$ (measured after the amplifier). $P_{\text{RF}}$ stays constant within 10 %, which is enough to strongly suppress the beam movement. However, if required, the system could be improved with a more exact calibration.

## A.4. Measurements of the Position Stability

The experimental setup that is used to measure the position stability of a beam diffracted by an AOM is shown in Fig. A.7. The $1/e^2$ beam radius of an Ytterbium fibre laser[9] at 1064 nm with 10 W output power is reduced from 2.1 mm to 0.7 mm with a telescope before going through the AOM. Behind the AOM all beams are blocked except one, which is attenuated by using only the transmission through two dielectric mirrors. The remaining laser power of less than 1 mW is monitored with a charged coupled device (CCD) camera at a distance of 1.4 m from the AOM. The images taken with this camera are evaluated by using a Matlab

[8]The use of Zener diodes with even smaller Zener voltages did not improve the quality of the transfer function, because their increase of conductivity at the Zener voltage is not as abrupt as for diodes with higher Zener voltages.

[9]IPG,YLR-20-1064-LPSF.

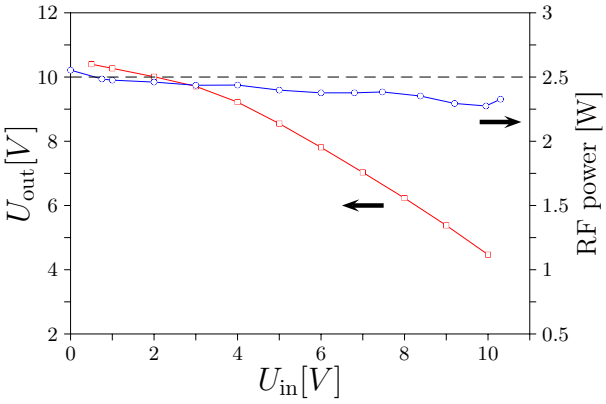


**Figure A.6.:** *Measured transfer function of the circuit for adjusting the control voltage $U_{\text{in}}$ (red squares). The blue line shows that $P_{\text{RF}}$ stays constant within 10 % when the circuit is used. $P_{\text{RF}}$ is measured after the amplifier with a spectrum analyzer.*

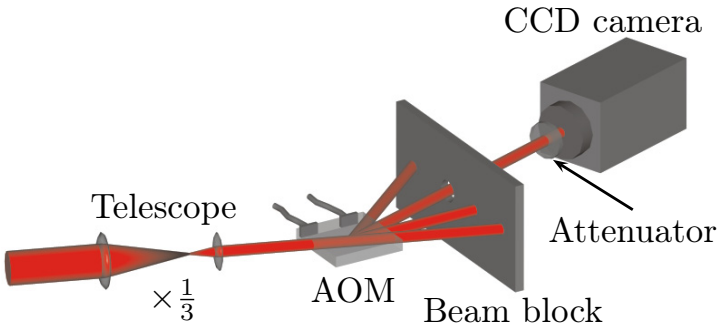


**Figure A.7.:** *Setup for measuring the position stability of a beam that is diffracted by an AOM. The size of the laser beam is reduced with a telescope before it enters the AOM. One diffracted beam is attenuated and monitored with a CCD camera, while the others are stopped with a beam block.*

routine, which fits a two-dimensional Gaussian profile to the images and records the peak position and beam size in the plane of diffraction ($x$) and perpendicular to it ($y$) about every 0.5 s.

Figure A.8 shows the time dependence of beam size and position on the camera in $x$ and $y$ direction of the first order beam for a Crystal Technology (CT) AOM[10] . At $t = 0$ the RF power is decreased from 2 W to 0.2 W, which leads to a beam movement due to thermal effects. Directly after switching the beam intensity drops, therefore the Matlab routine is not able to fit the images correctly for about 2 s. This leads e.g. to the peak of the $y$ size. After this it takes about 30 s until a new steady state is reached. Whereas the $y$ position changes by more than 1 mm, the $x$ position stays relatively constant. The sizes change both by approximately 0.05 mm, but in different directions.

To compare the position stability of the CT AOM using the above mentioned two-frequency driver with single frequency operation, the steady state value[11] is recorded for various RF powers. Figure A.9 shows the angular movement relative to the initial position as a function of laser power in the first order[12]. Also included in the figure are the results of two different

[10] Crystal Technology, 3110-199.
[11] Average of 20 fit values.
[12] For the two-frequency method the first order of $f_1$ is used. The two frequencies are: $f_1 = 99$ MHz and

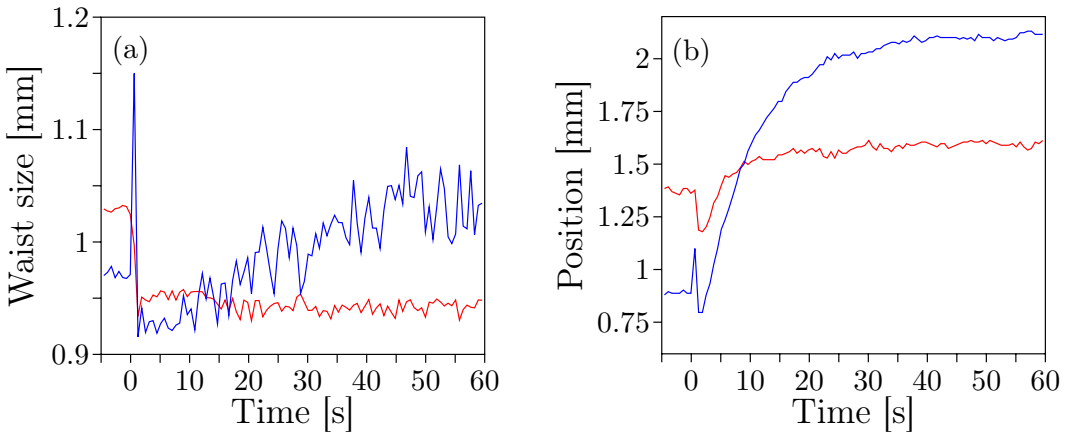


**Figure A.8.:** *Data taken with the experimental setup. Shown is the time dependence of size (a) and position (b) of the diffracted beam on the camera in x (red line) and y direction (red line) after decreasing the RF power by a factor of 10.*

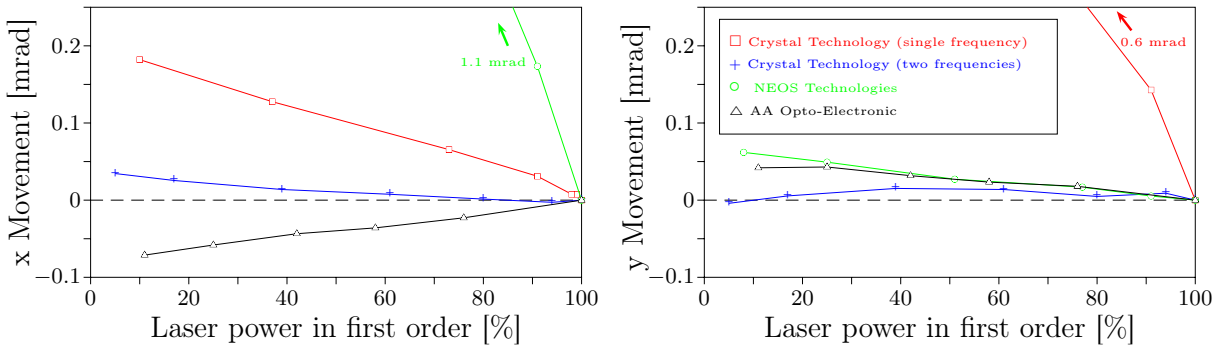


**Figure A.9.:** *Measured angular movement of the first order beam in x and y direction as a function of laser power in this beam. The movement is shown for the CT AOM both with and without the second frequency, and in addition for two other models driven with one frequency (see legend and text). For visibility reasons the movement is plotted only up to* 0.25 *mrad. The values at about 10 % laser power are indicated, if this range is exceeded.*

AOM models[13] that are driven by one frequency. The beam movement is smallest for the CT AOM with two frequencies, only up to 0.03 mrad in $x$ and 0.02 mrad in $y$ direction. This is a reduction by a factor of 7 in $x$ and 30 in $y$ direction compared to the same AOM driven by only one frequency. The NEOS AOM shows the largest movement (1.1 mrad in $x$). Its movement in $x$ is much larger than in $y$, whereas it is the opposite for the CT AOM. This is probably due to the different design of the AOMs, as both use the same crystal ($TeO_2$) and acoustic mode (longitudinal, sound velocity 4200 m/s). The A-A Opto-Electronic model is an acousto-optic *deflector*. It uses a sheer-mode acoustic mode with a 6 times smaller sound velocity and thus a 6 times larger deflection angle. It needs only 0.5 W RF power for maximum diffraction efficiency, which is the reason why its beam movement is nearly as small as for the two-frequency AOM. However, a drawback of this model is that (due to the

$f_2 = 123$ MHz. They are well within the bandwidth of the AOM, which is determined by measuring the back-reflected power of the AOM with a directional coupler (Mini-Circuits ZDC-10-1).

[13] A-A Opto-Electronic, MTS80-A3-1064Ac; NEOS Technologies, 23080-3-1.06-LTD.

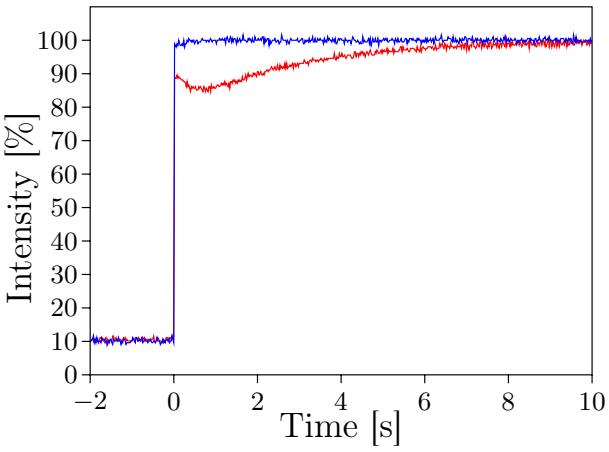


**Figure A.10.:** *Time dependence of the laser intensity when switching the RF power rapidly. Without the second frequency (red) it takes nearly 10 seconds for the intensity to stabilize to its steady state value. With the second frequency (blue) there is only a small transient effect in the first second.*

smaller sound velocity) the rise time, i.e. the time it takes until the diffracted laser power reaches its maximum, is 10 $\mu$s[14]. This limits the bandwidth for modulating laser light, e.g. to measure trap frequencies with parametric excitation.

The two-frequency method stabilizes also the laser power $P_\mathrm{L}$ in the first order when switching the RF power rapidly. This can be seen in Fig. A.10, which shows the time dependence $P_\mathrm{L}(t)$ for the CT AOM with and without the second frequency. With only one frequency it takes about 10 seconds until the steady state value is reached when switching $P_\mathrm{L}$ abruptly from 10 to 100%. The beam movement takes place over the same time scale. The intensity changes only by less than 2 % in the first second after switching when the second frequency is used. Although no quantitative statement can be made on the dependency of the waist size on the RF power[15], it seems clear that it is not affected by the two-frequency method. This suggests that it has a different origin than the movement of the beam, like thermal lensing in the crystal.

In conclusion, the measurements have shown that the beam properties strongly improve when an AOM is driven with two frequencies. The beam movement is reduced by a factor of 7 in $x$ and 30 in $y$ direction. The intensity is stabilized after a fast switching of the RF power to a variation of less than 2 %. These results have been confirmed by Bernd Kaltenhäuser, Harald Kübler and Stefan Müller with a $CO_2$ laser[16] and an AOM using a Germanium crystal[17]. Although the AOM needs 30 W RF power for maximum diffraction efficiency, the movement could be reduced by a factor of 10. The method is easy to implement in existing experimental setups and does not have the disadvantage of long rise times. Therefore its use is reasonable whenever a high position stability is needed and no single-mode fibre can be used.

[14]This value is measured with a photodiode.
[15]Whereas the peak position could be determined very precisely, the sizes depended strongly on the amount of light on the camera and its settings.
[16]Coherent, GEM100L.
[17]IntraAction Corp., AGM-406B1.

# B. Chromium

## B.1. General Properties

Chromium is a transition metal. It has an atomic number of 24 with 4 stable isotopes (see table B.1). $^{52}$Cr has the highest natural abundance of 83.79 % and is a Boson. The six outer

| Mass [au] | Natural abundance | Nuclear spin $I$ | statistics |
|---|---|---|---|
| 50 | 4.35 % | 0 | bosonic |
| 52 | 83.79 % | 0 | bosonic |
| 53 | 9.5 % | 3/2 | fermionic |
| 54 | 2.36 % | 0 | bosonic |

**Table B.1.:** *Natural abundance, spin and statistics of the four Chromium isotopes.*

electrons couple to a total spin of $S = 3$, leading to the total angular momentum of $J = 3$ of the $^7S_3$ ground state. The level scheme of Chromium is fortunate for the applicability of laser cooling techniques. The relevant transitions for the cooling are depicted in Fig. B.1. The

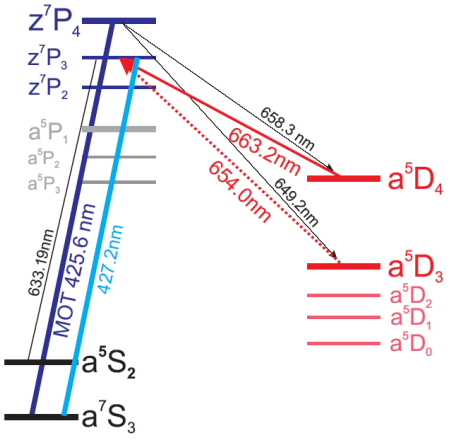


**Figure B.1.:** *Level scheme of $^{52}$Cr. Shown are the transitions that are relevant for laser cooling (see text).*

magneto-optical trap is operated on the $^7S_3 \leftrightarrow {}^7P_4$ transition with a wavelength of 425.6 nm. The atom decays to the metastable D states with a ratio of $\sim 1/250000$ from the excited P state. This $\lambda$-scheme is used to continuously load the magnetic trap. The repumping wavelength of the $^5D_4$ state via the $^7P_3$ state is 663.2 nm. The $^7P_3$ state is also used to optically pump the Chromium atoms into the lowest Zeeman state $M_J = -3$. The wavelength of the $^7S_3 \leftrightarrow {}^7P_3$ is 427.2 nm. More properties of $^{52}$Cr are summarized in table B.2.

| | |
|---|---|
| Mass | $8.7 \times 10^{-26}$ kg |
| Landé factor of $^7S_3$ | $g_J = -2.0018$ |
| Landé factor of $^7P_4$ | $g_J = -1.751$ |
| Doppler temperature $T_D$ | 124 $\mu$K |
| Recoil temperature $T_{rec}$ | 1.02 $\mu$K |
| Line width $\Gamma/2\pi$ | 5.02 MHz |
| Saturation intensity $I_{sat}$ | 8.52 mW/cm$^2$ |
| Scattering length $a_6$ [12] | $102 \pm 13\ a_0$ |

**Table B.2.:** *Properties of $^{52}Cr$.*

## B.2. Feshbach Resonances

Table B.3 summarizes the properties of the 14 Feshbach resonance that have been found for $^{52}$Cr [12]. For more information see also [60].

| Exp. Pos. [G] | Theo. Pos. [G] | Exp. $\Delta$ ($\frac{1}{\sqrt{e}}$) [mG] | Theo. $\Delta$ [mG] | $L_3$ [cm$^6$/s] | $l_i$;$SM_S$;$lm_l$ |
|---|---|---|---|---|---|
| 4.1 | 4.0 | 40 | ... | $3 \times 10^{-28}$ | 2; 6, −4; 0 , 0 |
| 6.1 | ... | 8 | ... | $8 \times 10^{-29}$ | ... |
| 8.2 | 8.1 | 100 | ... | $4 \times 10^{-27}$ | 2; 6, −5; 0 , 0 |
| 50.1 | 50.1 | 140 | $< 1 \times 10^{-3}$ | $2 \times 10^{-26}$ | 0; 6, −2; 4, −4 |
| 65.1 | 64.9 | 90 | $6 \times 10^{-3}$ | $5 \times 10^{-26}$ | 0; 6, −3; 4, −3 |
| 98.9 | 98.5 | 90 | 0.30 | $1 \times 10^{-24}$ | 0; 6, −4; 4, −2 |
| 143.9 | 143.2 | 120 | 0.12 | $1 \times 10^{-26}$ | 0; 4, −2; 4, −4 |
| 188.3 | 187.9 | 150 | 0.22 | $4 \times 10^{-26}$ | 0; 4, −3; 4, −3 |
| 205.8 | 205.6 | 420 | 12 | $4 \times 10^{-24}$ | 0; 6, −5; 4, −1 |
| 286.6 | 288.0 | 430 | 12 | $6 \times 10^{-25}$ | 0; 4, −4; 4, −2 |
| 290.3 | 290.7 | 470 | 51 | $1 \times 10^{-25}$ | 0; 6, −4; 2, −2 |
| 379.2 | 379.2 | 140 | 0.42 | $1 \times 10^{-25}$ | 0; 2, −2; 4, −4 |
| 499.9 | 499.2 | 370 | 81 | $1 \times 10^{-24}$ | 0; 4, −4; 2, −2 |
| 589.1 | 589.2 | 680 | 1700 | $3 \times 10^{-24}$ | 0; 6, −5; 2, −1 |

**Table B.3.:** *Feshbach resonances of $^{52}Cr$ observed in [12]. Besides the experimental determined widths, also the theoretical values arising from multi-channel calculations are given. $L_3$ is the theoretical three-body loss coefficient. In the last column quantum numbers are assigned to the resonances.*

# C. Mathematical Supplement

## C.1. Incomplete Elliptic Integral Function

The function $f(A_{xz}, A_{yz})$ that appears in the hydrodynamic equations describing a dipolar condensate depends on the incomplete elliptic integrals of the first and second kind $\mathrm{F}(\varphi/\alpha)$ and $\mathrm{E}(\varphi/\alpha)$ [95]. The discussion of the function in this appendix follows closely [74]. The function is given by the following expression

$$f(A_{xz}, A_{yz}) = 1 + 3A_{xz}A_{yz}\frac{\mathrm{E}(\varphi/\alpha) - \mathrm{F}(\varphi/\alpha)}{(1 - A_{yz}^2)\sqrt{1 - A_{xz^2}}}\,, \tag{C.1}$$

with

$$\sin\varphi = \sqrt{1 - A_{xz}^2}\,, \tag{C.2}$$

$$\sin^2\alpha = \frac{1 - A_{yz}^2}{1 - A_{xz}^2} \tag{C.3}$$

(see Fig. C.1). It is symmetric

$$f(x, y) = f(y, x) \tag{C.4}$$

and a smooth and limited function with the property that

$$1 \geq f(x, y) \geq -2\,. \tag{C.5}$$

If one of its arguments is zero, the function is equal to one

$$f(x, 0) = f(0, y) = 1\,. \tag{C.6}$$

The asymptotic behaviour, if one of the arguments is very large, is

$$f_\infty(x) = f(x, \infty) = 1 - 3\frac{(1 - x)x}{1 - x^2}\,. \tag{C.7}$$

For both arguments large, $f$ becomes

$$f(\infty, \infty) = -2\,. \tag{C.8}$$

The special case of equal arguments results in

$$f_\mathrm{s}(A) = f(A, A) = \frac{1 + 2A^2}{1 - A^2} - \frac{3A^2\tanh^{-1}\sqrt{1 - A^2}}{(1 - A^2)^{3/2}}\,, \tag{C.9}$$

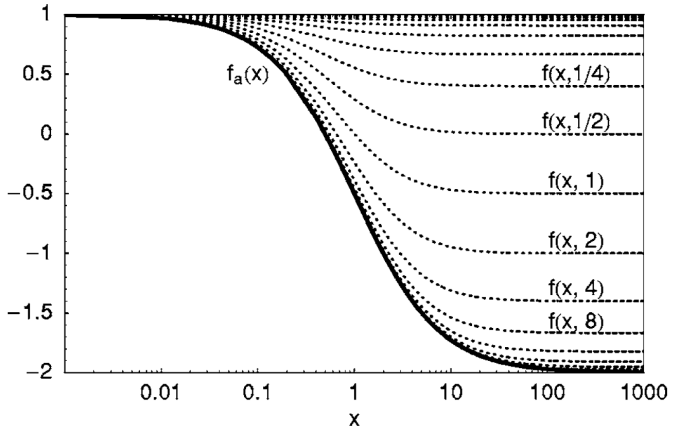


**Figure C.1.:** *Log-linear plot of the function $f(x, y)$ vs. $x$ and for different $y$ (dashed lines). The solid line corresponds to $f_\infty(x)$ defined in Eq. (C.7). Figure taken from [74].*

which corresponds to a cylindrically symmetric trap. Moreover $f$ obeys the sum rule

$$f(x, y) + f\left(\frac{y}{x}, \frac{1}{x}\right) + f\left(\frac{1}{y}, \frac{x}{y}\right) = 0\,, \tag{C.10}$$

with the physical meaning that the average over all directions of the polarization gives zero contribution to the dipolar energy [74]. One can use this expression to calculate a polynomial expression of $f$ around the point $(x, y) = (1, 1)$, which represents a spherical condensate. A third order approximation which gives an error smaller than 7 % for aspect ratios in the range $A = 0.5$ to $A = 1.6$ is

$$f(1 + x, 1 + y) \approx \frac{-2(x + y)}{5} + \frac{9(x^2 + y^2) - 8xy}{35} + \frac{12(x^2y + xy^2) - 16(x^3 + y^3)}{105}\,. \tag{C.11}$$

## C.2. Magnetic Field of a Cylindrically Symmetric Current Distribution

In this appendix C.2 I derive the relation $f_z^2 = -2f_r^2$, which is used to calibrate the curvature compensation. The relation is valid close to the origin ($r = 0, z = 0$) for a magnetic field produced by a cylindrically symmetric current distribution with a parabolic field distribution

$$\boldsymbol{B}(0, z) = f(z)\,\boldsymbol{e}_z = \left(B_0 + \frac{1}{2}b''z^2\right)\,\boldsymbol{e}_z \tag{C.12}$$

on axis. The on-axis field (up to second order in $z$) of a pair of coaxial coils with the current running in the same direction is exactly of this kind (see for example [96]).

Symmetry considerations (see Fig. C.2) show that the field of a cylindrical current distribution has the following form:

$$\boldsymbol{B}(z, r) = B_r(r, z)\,\boldsymbol{e}_r + B_z(r, z)\,\boldsymbol{e}_z\,. \tag{C.13}$$

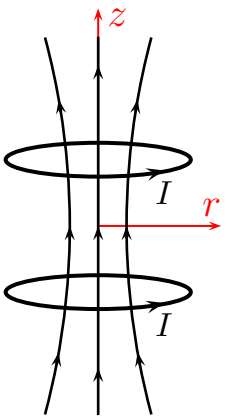


**Figure C.2.:** *Illustration of the magnetic field produced by a cylindrically symmetric current distribution. Due to the symmetry the field has only components in r and in z direction. Upon reflection on a plane including the z axis, the z component is symmetric, whereas the r component is antisymmetric.*

Moreover, $B_r(r,z)$ depends only on odd powers of $r$, as for this component $B_r(r,z) = -B_r(-r,z)$, and $B_z(r,z)$ depends only on even powers ($B_r(r,z) = B_r(-r,z)$). If the coefficients are expanded around the origin, this implies that

$$B_r(r,z) = \sum_{n=0}^{\infty} c_{2n+1}(z) r^{2n+1}\,, \tag{C.14}$$

$$B_z(r,z) = \sum_{n=0}^{\infty} d_{2n}(z) r^{2n}\,. \tag{C.15}$$

For $n = 0$ we see that $d_0(z) = f(z)$ because of Eq. (C.12).

In a current-free region both divergence and curl of the magnetic field are zero. Expressed in cylindrical coordinates this gives:

$$\frac{\partial}{\partial z} B_r - \frac{\partial}{\partial r} B_z = 0\,, \tag{C.16}$$

$$\frac{1}{r}\frac{\partial}{\partial r}(r B_r) + \frac{\partial}{\partial z} B_z = 0\,. \tag{C.17}$$

If we now include Eq. (C.14) and (C.15) into Eq. (C.16) and (C.17), we get recursion relations for the expansion coefficients:

$$c'_{2n+1}(z) = (2n+2) d_{2n+2}(z)\,, \tag{C.18}$$

$$c_{2n+1}(z) = -\frac{1}{2n+2} d'_{2n}(z)\,. \tag{C.19}$$

The coefficients $d_{2n}(z)$ are obtained by inserting Eq. (C.19) in Eq. (C.18) and solving the resulting equation. With this solution also the $c_{2n+1}(z)$ are obtained. Knowing that $d_0(z) =$

$f(z)$, we get:

$$c_{2n+1}(z) = \frac{(-1)^{n+1}}{2^{2n+1}(n+1)!n!} f^{(2n+1)}(z)\,, \tag{C.20}$$

$$d_{2n}(z) = \frac{(-1)^{n}}{2^{2n}(n!)^2} f^{(2n)}(z)\,. \tag{C.21}$$

Please note that these relations are of course valid also for an arbitrary function $f(z)$.

Let us now calculate $B_r$ and $B_z$ up to second order in $r$ and $z$ for the parabolic field distribution on axis. With Eq. (C.20) and (C.21) we directly obtain

$$B_r(r,z) \approx -\frac{1}{2}b''zr\,, \tag{C.22}$$

$$B_z(r,z) \approx B_0 + \frac{1}{2}b''\left(z^2 - \frac{1}{2}r^2\right)\,. \tag{C.23}$$

Thus, $B^2$ up to second order is

$$B^2 = B_r^2 + B_z^2 \approx B_z^2 \approx B_0^2 + B_0 b''\left(z^2 - \frac{1}{2}r^2\right)\,. \tag{C.24}$$

Hence, finally we get to $f_z^2 = -2f_r^2$, if we recall that $f_z^2 \propto \partial_z^2 B$ and $f_r^2 \propto \partial_r^2 B$ and use

$$B = B_0\sqrt{1 + \frac{b''}{B_0}\left(z^2 - \frac{1}{2}r^2\right)} \approx B_0 + \frac{1}{2}b''\left(z^2 - \frac{1}{2}r^2\right)\,. \tag{C.25}$$

## C.3. Dependence of the Optical Density of Linear Polarized Light to $\sigma^-$-Light

Linear polarized light traveling in the magnetic field direction can be decomposed in $\sigma^-$ and $\sigma^+$-light. Thus the linear polarized light can be written in terms of the spherical unit vectors introduced in section 4.4

$$\boldsymbol{E}_{\text{in}} = E_0(\hat{\boldsymbol{u}}_{\sigma^+} + \hat{\boldsymbol{u}}_{\sigma^-})\,. \tag{C.26}$$

Only the $\sigma^-$-component is absorbed, which results in an outgoing electric field

$$\boldsymbol{E}_{\text{out}} = E_0(\hat{\boldsymbol{u}}_{\sigma^+} + e^{\frac{-x}{2}}\hat{\boldsymbol{u}}_{\sigma^-})\,, \tag{C.27}$$

where $x$ denotes the optical density that is observed for $\sigma^-$-light. With the definition of the optical density (4.20) we get the dependence of the OD of linear polarized light (denoted with $y$) on $x$:

$$y = -ln\left(\frac{I_{\text{out}}}{I_{\text{in}}}\right) = -ln\left(\frac{|E_{\text{out}}|^2}{|E_{\text{in}}|^2}\right) = -ln\left(\frac{1+e^{-x}}{2}\right)\,. \tag{C.28}$$

# Bibliography


[1] T. Lahaye, T. Koch, B. Fröhlich, M. Fattori, J. Metz, A. Griesmaier, S. Giovanazzi and T. Pfau, *Strong dipolar effects in a quantum ferrofluid*, Nature, **448**, 672 (2007). 1, 4, 57

[2] M. Baranov, Ł. Dobrek, K. Góral, L. Santos and M. Lewenstein, *Ultracold Dipolar Gases — a Challenge for Experiments and Theory*, Physica Scripta, **2002**, 74–81 (2002). 1, 4

[3] P. Kapitza, *Viscosity of liquid helium below the gimel-point*, Nature, **141**, 74 (1938). 1, 3

[4] J. F. Allen and A. D. Misener, *Flow phenomena in liquid helium II*, Nature, **142**, 643–644 (1938). 1, 3

[5] D. D. Osheroff, R. C. Richardson and D. M. Lee, *Evidence for a New Phase of Solid He-3*, Physical Review Letters, **28**, 885 (1972). 1, 3

[6] M. H. Anderson, J. R. Ensher, M. R. Matthews, C. E. Wieman and E. A. Cornell, *Observation of Bose-Einstein Condensation in a Dilute Atomic Vapor*, Science, **269**, 198 (1995). 1, 3, 23

[7] K. B. Davis, M. O. Mewes, M. R. Andrews, N. J. van Druten, D. S. Durfee, D. M. Kurn, and W. Ketterle, *Bose-Einstein Condensation in a Gas of Sodium Atoms*, Physical Review Letters, **75**, 3969 (1995). 1, 3, 23

[8] M. W. Zwierlein, J. R. Abo-Shaeer, A. Schirotzek, C. H. Schunck and W. Ketterle, *Vortices and superfluidity in a strongly interacting Fermi gas*, Nature, **435**, 1047 (2005). 1, 3

[9] A. Griesmaier, J. Werner, S. Hensler, J. Stuhler and T. Pfau, *Bose-Einstein Condensation of Chromium*, Physical Review Letters, **94**, 160401 (2005). 1, 3, 4

[10] J. Stuhler, A. Griesmaier, T. Koch, M. Fattori, S. Giovanazzi, P. Pedri, L. Santos and T. Pfau, *Observation of Dipole-Dipole Interaction in a Degenerate Quantum Gas*, Physical Review Letters, **95**, 150406 (2005). 1, 4, 29, 30, 31, 32, 63, 64

[11] S. Inouye, M. R. Andrews, J. Stenger, H.-J. Miesner, D. M. Stamper-Kurn and W. Ketterle, *Observation of Feshbach resonances in a Bose-Einstein condensate*, Nature, **392**, 151 (1998). 1, 3

[12] J. Werner, A. Griesmaier, S. Hensler, J. Stuhler, T. Pfau, A. Simoni and E. Tiesinga, *Observation of Feshbach Resonances in an Ultracold Gas of* $^{52}Cr$, Physical Review Letters, **94**, 183201 (2005). 1, 4, 18, 21, 50, 57, 60, 82

[13] B. Fröhlich, T. Lahaye, B. Kaltenhäuser, H. Kübler, S. Müller, T. Koch, M. Fattori and T. Pfau, *Two-frequency acousto-optic modulator driver to improve the beam pointing stability during intensity ramps*, Review of Scientific Instruments, **78**, 043101 (2007). 2, 5, 38, 71

[14] A. Einstein, *Quantentheorie des einatomigen idealen Gases, Zweite Abhandlung*, Sitzungsber. Kg. Preuss. Akad. Wiss., page 3 (1925). 3, 23

[15] D. Vollhardt and P. Wölfle, *The Superfluid Phases of Helium 3*, Taylor & Francis, London (1990). 3

[16] C. C. Bradley, C. A. Sackett, J. J. Tollett and R. G. Hulet, *Evidence of Bose-Einstein Condensation in an Atomic Gas with Attractive Interactions*, Physical Review Letters, **75**, 1687 (1995). 3

[17] D. G. Fried, T. C. Killian, L. Willmann, D. Landhuis, S. C. Moss, D. Kleppner and T. J. Greytak, *Bose-Einstein Condensation of Atomic Hydrogen*, Physical Review Letters, **81**, 3811 (1998). 3

[18] S. L. Cornish, N. R. Claussen, J. L. Roberts, E. A. Cornell and C. E. Wieman, *Stable $^{85}Rb$ Bose-Einstein Condensates with Widely Tunable Interactions*, Physical Review Letters, **85**, 1795–1798 (2000). 3

[19] A. Robert, O. Sirjean, A. Browaeys, J. Poupard, S. Nowak, D. Boiron, C. I. Westbrook and A. Aspect, *A Bose-Einstein Condensate of Metastable Atoms*, Science, **292**, 461 (2001). 3

[20] G. Modugno, G. Ferrari, G. Roati, R. J. Brecha, A. Simoni and M. Inguscio, *Bose-Einstein Condensation of Potassium Atoms by Sympathetic Cooling*, Science, **294**, 1320 (2001). 3

[21] T. Weber, J. Herbig, M. Mark, H.-C. Nägerl and R. Grimm, *Bose-Einstein Condensation of Cesium*, Science, **299**, 232–235 (2003). 3

[22] Y. Takasu, K. Maki, K. Komori, T. Takano, K. Honda, M. Kumakura, T. Yabuzaki and Y. Takahashi, *Spin-Singlet Bose-Einstein Condensation of Two-Electron Atoms*, Physical Review Letters, **91**, 040404 (2003). 3

[23] G. Roati, M. Zaccanti, C. D'Errico, J. Catani, M. Modugno, A. Simoni, M. Inguscio and G. Modugno, *39-K Bose-Einstein condensate with tunable interactions*, Preprint at <http://arxiv.org/abs/cond-mat/0703714> (2007). 3

[24] D. S. Jin, J. R. Ensher, M. R. Matthews, C. E. Wieman and E. A. Cornell, *Collective Excitations of a Bose-Einstein Condensate in a Dilute Gas*, Physical Review Letters, **77**, 420–423 (1996). 3

[25] M. R. Matthews, B. P. Anderson, P. C. Haljan, D. S. Hall, C. E. Wieman and E. A. Cornell, *Vortices in a Bose-Einstein Condensate*, Physical Review Letters, **83**, 2498–2501 (1999). 3

[26] J. Dalibard, *Collisional dynamics of ultra-cold atomic gases*, in M. Inguscio, S. Stringari and C. Wieman, editors, *Proceedings of the International School of Physics - Enrico Fermi*, page 321, IOS Press (1999). 3, 7, 11, 12, 30

[27] B. DeMarco and D. S. Jin, *Onset of Fermi Degeneracy in a Trapped Atomic Gas*, Science, **285**, 1703 (1999). 3

[28] J. S. J. Bardeen, L. Cooper, *Microscopic Theory of Superconductivity*, Physical Review, **106**, 162–164 (1957). 3

[29] T. Loftus, C. A. Regal, C. Ticknor, J. L. Bohn and D. S. Jin, *Resonant Control of Elastic Collisions in an Optically Trapped Fermi Gas of Atoms*, Physical Review Letters, **88**, 173201 (2002). 3

[30] K. Dieckmann, C. A. Stan, S. Gupta, Z. Hadzibabic, C. H. S. W. and Ketterle, *Decay of an Ultracold Fermionic Lithium Gas near a Feshbach Resonance*, Phys. Rev. Lett., **89**, 203201 (2002). 3

[31] K. M. O'Hara, S. L. Hemmer, M. E. Gehm, S. R. Granade and J. E. Thomas, *Observation of a Strongly Interacting Degenerate Fermi Gas of Atoms*, Science, **298**, 2179 (2002). 3

[32] C. A. Regal, M. Greiner and D. S. Jin, *Observation of Resonance Condensation of Fermionic Atom Pairs*, Physical Review Letters, **92**, 040403 (2004). 3

[33] M. W. Zwierlein, C. A. Stan, C. H. Schunck, S. M. F. Raupach, A. J. Kerman and W. Ketterle, *Condensation of Pairs of Fermionic Atoms near a Feshbach Resonance*, Physical Review Letters, **92**, 120403 (2004). 3

[34] M. Greiner, C. A. Regal and D. S. Jin, *Probing the excitation spectrum of a fermi gas in the BCS-BEC crossover regime*, Physical Review Letters, **94**, 070403 (2005). 3

[35] W. Ketterle and Y. il Shin, *Fermi gases go with the superfluid flow*, Physics World, **20**, 39–43 (2007). 3

[36] K. Goral, L. Santos and M. Lewenstein, *Quantum Phases of Dipolar Bosons in Optical Lattices*, Physical Review Letters, **88**, 170406 (2002). 4

[37] O. Dutta and P. Meystre, *Ground-state structure and stability of dipolar condensates in anisotropic traps*, Preprint at <http://arxiv.org/abs/cond-mat/0703044> (2007). 4

[38] S. Ronen, D. C. E. Bortolotti and J. L. Bohn, *Radial and Angular Rotons in Trapped Dipolar Gases*, Physical Review Letters, **98**, 030406 (2007). 4

[39] Y. Kawaguchi, H. Saito and M. Ueda, *Einstein–de Haas Effect in Dipolar Bose-Einstein Condensates*, Physical Review Letters, **96**, 080405 (2006). 4

[40] L. Santos and T. Pfau, *Spin-3 Chromium Bose-Einstein Condensates*, Physical Review Letters, **96**, 190404 (2006). 4

[41] S. Yi and H. Pu, *Spontaneous Spin Textures in Dipolar Spinor Condensates*, Physical Review Letters, **97**, 020401 (2006). 4

[42] L. Santos, G. Shlyapnikov and M. Lewenstein, *Roton-Maxon Spectrum and Stability of Trapped Dipolar Bose-Einstein Condensates*, Physical Review Letters, **90**, 250403 (2003). 4

[43] R. K. J. Doyle, B. Friedrich and F. Masnou-Seeuws, *Quo vadis, cold molecules?*, European Physical Journal D, **31**, 149 (2004). 4

[44] M. Köhl, H. Moritz, T. Stöferle, K. Günter and T. Esslinger, *Fermionic Atoms in a Three Dimensional Optical Lattice: Observing Fermi Surfaces, Dynamics, and Interactions*, Physical Review Letters, **94**, 080403 (2005). 4

[45] C. Ospelkaus, S. Ospelkaus, L. Humbert, P. Ernst, K. Sengstock and K. Bongs, *Ultracold Heteronuclear Molecules in a 3D Optical Lattice*, Physical Review Letters, **97**, 120402 (2006). 4

[46] J. M. Sage, S. Sainis, T. Bergeman and D. DeMille, *Optical Production of Ultracold Polar Molecules*, Physical Review Letters, **94**, 203001 (2005). 4

[47] M. Marinescu and L. You, *Controlling Atom-Atom Interaction at Ultralow Temperatures by dc Electric Fields*, Physical Review Letters, **81**, 4596–4599 (1998). 4

[48] S. Giovanazzi, D. O'Dell and G. Kurizki, *Density Modulations of Bose-Einstein Condensates via Laser-Induced Interactions*, Physical Review Letters, **88**, 130402 (2002). 4

[49] J. C. Cohen-Tannoudji, *Atom-Atom Interactions in Ultracold Quantum Gases — Lectures on Quantum Gases Institut Henri Poincaré*, available online at http://www.phys.ens.fr/∼castin/ (2007). 4, 13, 15, 16, 17

[50] A. Griesmaier, *Dipole-dipole interaction in a degenerate quantum gas – Bose-Einstein condensation of chromium atoms*, Dissertation, University of Stuttgart (2006). 5, 35, 36, 37, 38, 39, 51, 55

[51] J. C. Cohen-Tannoudji, *Quantum mechanics 2*, de Gruyter (1999). 7, 10, 11

[52] J. J. Sakurai, *Modern Quantum Mechanics — Revised Edition*, Addison-Wesley publishing Company (1994). 7

[53] W. Nolting, *Quantenmechanik 2*, Verlag Zimmermann-Neufang (1992). 7, 9, 11

[54] C. Pethick and H. Smith, *Bose-Einstein Condensation in Dilute Gases*, Cambridge University Press (2004). 12, 15, 23, 25, 27

[55] L. Pitaevskii and S. Stringari, *Bose-Einstein Condensation*, Oxford Science Publications (2003). 14, 23

[56] E. Braaten and H. Hammer, *Universality in Few-body Systems with Large Scattering Length*, Physics Reports, **428**, 259–390 (2006). 14, 58

[57] J. Stenger, S. Inouye, M. R. Andrews, H.-J. Miesner, D. M. Stamper-Kurn and W. Ketterle, *Strongly Enhanced Inelastic Collisions in a Bose-Einstein Condensate near Feshbach Resonances*, Physical Review Letters, **82** (1999). 14, 58

[58] V. A. Yurovsky and A. Ben-Reuven, *Atom loss from Bose-Einstein condensates due to Feshbach resonances*, Physical Review A, **60**, R765 (1999). 14

[59] T. Köhler, K. Góral and P. S. Julienne, *Production of cold molecules via magnetically tunable Feshbach resonances*, Reviews of Modern Physics, **78**, 1311 (2006). 15, 18

[60] J. Werner, *Observation of Feshbach resonances in an ultracold gas of $^{52}Cr$*, Dissertation, University of Stuttgart (2006). 15, 18, 21, 35, 82

[61] Z. Pavlovic, B. O. Roos, R. Cote and H. R. Sadeghpour, *Collisional properties of trapped cold chromium atoms*, Physical Review A (Atomic, Molecular, and Optical Physics), **69**, 030701 (2004). 18, 20

[62] W. J. Childs and L. S. Goodman, *Electronic g Factors of Low-Lying Levels of Fe I, Cr I and Mn I*, Physical Review A (Atomic, Molecular, and Optical Physics), **140 (2A)**, A447 (1965). 19

[63] H. Haken and H. C. Wolf, *Atom- und Quantenphysik*, Springer-Verlag (1990). 19

[64] F. H. Mies, C. J. Williams, P. S. Julienne and M. Krauss, *Estimating Bounds on Collisional Relaxation Rates of Spin-Polarized 87Rb Atoms at Ultracold Temperatures*, Journal of Research of the National Institute of Standards and Technology, **101**, 521 (1996). 20

[65] W. Demtröder, *Molekülphysik*, Oldenbourg Wissenschaftsverlag (2003). 20

[66] W. Ketterle, D. Durfee and D. Stamper-Kurn, *Making, probing and understanding Bose-Einstein condensates*, in M. Inguscio, S. Stringari and C. Wieman, editors, *Proceedings of the International School of Physics - Enrico Fermi*, page 67, IOS Press (1999). 23, 24

[67] Y. Castin, *Bose-Einstein condensates in atomic gases: simple theoretical results*, available online at http://www.phys.ens.fr/cours/notes-de-cours/castin/castin.pdf (2000). 23, 27

[68] F. Schwabl, *Statistische Mechanik*, Springer-Lehrbuchverlag (2000). 23

[69] W. Greiner, *Thermodynamik und Statistische Mechanik*, Verlag Harri Deutsch (1987). 23

[70] Y. Castin and R. Dum, *Bose-Einstein Condensates in Time Dependent Traps*, Physical Review Letters, **77**, 5315 (1996). 28

[71] K. Goral, K. Rzazewski and T. Pfau, *Bose-Einstein condensation with magnetic dipole-dipole forces*, Physical Review A, **61**, 051601 (2000). 30

[72] S. Yi and L. You, *Trapped condensates of atoms with dipole interactions*, Physical Review A, **63**, 053607 (2001). 30

[73] C. Eberlein, S. Giovanazzi and D. H. J. O'Dell, *Exact solution of the Thomas-Fermi equation for a trapped Bose-Einstein condensate with dipole-dipole interactions*, Physical Review A, **71**, 033618 (2005). 30, 32, 33

[74] S. Giovanazzi, P. Pedri, L.Santos, A. Griesmaier, M. Fattori, T. Koch, J. Stuhler and T. Pfau, *Expansion dynamics of a dipolar Bose-Einstein condensate*, Physical Review A, **74**, 013621 (2006). 31, 83, 84

[75] J. Stuhler, *Kontinuierliches Laden einer Magnetfalle mit lasergekühlten Chromatomen*, Dissertation, University of Stuttgart (2001). 35

[76] P. O. Schmidt, *Scattering properties of ultra-cold chromium atoms*, Dissertation, University of Stuttgart (2003). 35, 37

[77] S. Hensler, *Wechselwirkung in ultrakalten dipolaren Gasen*, Dissertation, University of Stuttgart (2004). 35, 37, 39

[78] A. Griesmaier, J. Stuhler and T. Pfau, *Production of a chromium Bose-Einstein condensate*, Applied Physics B, **82**, 211–216 (2006). 35

[79] J. Werner, *Kontinuierliches Laden einer Magnetfalle mit lasergekühlten Chromatomen*, Diplomarbeit, University of Stuttgart (2000). 35

[80] T. Binhammer, *Verdampfungskühlung ultrakalter Chrom-Atome*, Diplomarbeit, University of Stuttgart (2002). 35

[81] A. Griesmaier, *Aufbau einer kombinierten magneto-optischen Falle für Chrom und Rubidium*, Diplomarbeit, University of Stuttgart (2002). 35, 37, 42

[82] S. Götz, *Demagnetization cooling in an ultracold chromium gas*, Diplomarbeit, University of Stuttgart (2006). 35

[83] L. D. Landau and E. M. Lifschitz, *Lehrbuch der theoretischen Physik, Bd.1, Mechanik*, Deutsch (Harri) (1997). 40

[84] E. A. Donley, N. R. Claussen, S. T. Thompson and C. E. Wieman, *Atom-molecule coherence in a Bose-Einstein condensate*, Nature, **417**, 529 (2002). 51, 68

[85] H. J. Metcalf and P. v. d. Straten, *Laser Cooling and Trapping*, Springer-Verlag (1999). 52, 54

[86] K. Xu, T. Mukaiyama, J. R. Abo-Shaeer, J. K. Chin, D. E. Miller and W. Ketterle, *Formation of Quantum-Degenerate Sodium Molecules*, Physical Review Letters, **91**, 210402 (2003). 68

[87] J. Herbig, T. Kraemer, M. Mark, T. Weber, C. Chin, H.-C. Nägerl and R. Grimm, *Preparation of a Pure Molecular Quantum Gas*, Science, **301**, 1510 (2003). 68

[88] S. Dürr, T. Volz, A. Marte and G. Rempe, *Observation of Molecules Produced from a Bose-Einstein Condensate*, Physical Review Letters, **92**, 020406 (2004). 68

[89] A. P. Goutzoulis and D. Pape, editors, *Design and Fabrication of Acousto-Optic Devices*, CRC (1994). 71

[90] A. Yariv, *Optical Electronics*, Saunders College Publishers (1991). 71, 73

[91] M. Born and E. Wolf, *Principles of Optics*, Cambridge University Press (2003). 71

[92] L. Brillouin, *Diffusion de la lumiére et des rayons X par un corps transparent homogéne*, Ann. Physique, **17**, 88 (1922). 71

[93] J. Eichler and H.-J. Eichler, *Laser — Grundlagen, Systeme, Anwendungen*, Springer Verlag (1990). 72

[94] D. L. Hecht, *Multifrequency Acoustooptic Diffraction*, IEEE Transactions on Sonics and Ultrasonics, **SU-24** (1977). 74

[95] M. Abramowitz and I. A. Stegun, *Handbook of Mathematical Functions with Formulas, Graphs and Mathematical Table*, Dober Publications (1972). 83

[96] J. D. Jackson, *Classical Electrodynamics*, John Wiley and Sons, Inc. (1999). 84

# D. Danksagung

Und zu guter Letzt möchte ich mich noch bei allen Leuten bedanken, die zum Gelingen dieser Arbeit beigetragen haben. Ohne die Unterstützung von allen Seiten, wäre diese Arbeit so nicht möglich gewesen:

- An erster Stelle bedanke ich mich sehr herzlich bei Herrn Prof. T. Pfau, der meinen Weg an der Stuttgarter Universität von Anfang an begleitet hat. Angefangen mit dem kleinen Laborpraktikum bei Chrom I und der zwei Jahre langen Hiwi Zeit, was mir interessante Einblicke in die Welt eines Experimentalphysikers lieferte und auch sehr beim Erstellen der Diplomarbeit geholfen hat, bis hin zur Diplomarbeit die ich an seinem Institut machen durfte in dem meiner Meinung nach spannendsten Gebiet der Physik, das es momentan gibt. Insbesondere auch für die Unterstützung bei der Erstellung des AOM Artikels, die motivierenden Worte in der Weihnachtsansprache und das nette Angebot noch eine weitere Zeit hier arbeiten zu dürfen. Vielen Dank!

- Second, I thank of course Thierry Lahaye, from whose brilliancy I benefited so infinitely much! I learned so many things from him in this year that will serve me well in the future. Thank you for all the 'small calculations' that taught me more than any book could have taught me, for the motivation to write the AOM article, for the support in the lab, for explaining all things to me as often as I needed it, for making the nice results possible described in this thesis... And of course for still proof-reading this thesis, although already being in France and waiting for the baby!

- Bei Tobias Koch, dessen gute Ideen die Arbeit im Labor immer wieder voran gebracht haben. Viele Dinge die in dieser Arbeit beschrieben sind, sind auf seinem 'Mist' gewachsen. Natürlich auch für die Unterstützung während der ganzen Diplomarbeit und die Korrekturen in letzter Minute!

- Bei Jonas Metz, für seine unermüdlichen Versuche mir einen besseren Schreibstil aufzuprägen, ich hoffe es war nicht vollkommen umsonst!

- I thank Marco Fattori, for the short time I could work together with him. He also taught me many things and his 'gute Laune' made the work in the lab always enjoyable.

- Und dem ganzen Rest vom Institut ein herzliches Dankeschön! Es war sehr angenehm hier zu arbeiten. Axel Griesmeier, der mir schon im Laborpraktikum gezeigt hat wie mühsam Laborarbeit sein kann (Stichwort Faser einkoppeln)... Aber natürlich auch für das Beantworten aller Fragen zum Labor. Ulrich Raitzsch und Alexander Greiner für die Zeit kurz nach dem Mittagessen. Alexander Greiner und Jimmy Sebastian auch besonders für die Hilfe in der Hiwi-Zeit. Den restlichen Rubidis für den tollen Schraubenschrank. Björn Butscher auch besonders für das grösstenteils Übernehmen der Weihnachtsfeier-Organisation. Da konntest du schon mal üben für das Greenhorn

Meeting... Und natürlich auch den anderen Chrom II Leute und den Leuten aus dem dritten Stock, besonders Harald für das Lösen aller Computerprobleme. Und dann natürlich auch Sylvia, Nadine und Karin!

- Von den Ehemaligen danke ich ganz besonders auch Sven Hensler, der mir in der Hiwi Zeit sehr geholfen hat, und Bernd Kaltenhäuser für die schöne Grafik im AOM Artikel.
- Bei Herrn Prof. Dr. Wrachtrup für die Teilnahme als Mitberichter.
- Bei meinen Eltern für die Unterstützung in jeglicher Hinsicht während meines ganzen Studium!
- Bei meinen Freunden für den Ausgleich neben der Arbeit, besonders natürlich bei Sebo, Erik, Domi, Christian und Anna. Bei Patrick, Ilona und Alex für die effektive Prüfungsvorbereitung. Und bei den Chaoten, die es mir erlaubt haben hier in Stuttgart weiter Musik zu machen und dazu verbunden mit so viel Spaß!.
- Und last but absolutely not least bei meiner Freundin Denise für die Unterstützung und Geduld die sie aufgebracht hat, wenn es mal wieder später wurde, besonders natürlich in den letzten Wochen!